Nanoscale study of effective organic nano-coating on cement paste surface under aggressive environment for sustainable building materials

Xiaodong Zhu

Université de Lille

N° d'ordre :

THÈSE DE DOCTORAT
DE L'UNIVERSITÉ DE LILLE

réalisée au sein de

École doctorale n°632 : Sciences de l'Ingénierie et des Systèmes – ENGSYS

Laboratoire de Génie Civil et Géo-Environnement – LGCgE ULR4515

Étude à l'échelle nanométrique du nano-revêtement organique efficace sur la surface de la pâte de ciment dans un environnement agressif pour des matériaux de construction durables

Nanoscale study of effective organic nano-coating on cement paste surface under aggressive environment for sustainable building materials

---

Thèse soutenue publiquement le **27/11/2023**, par

Xiao-Dong ZHU

pour obtenir le grade de :

DOCTEUR en GÉNIE CIVIL de L'UNIVERSITE DE LILLE

Devant le jury composé de :

Fabrizio Cleri, Professeur	Président, University of Lille, France.
Siham Kamali-Bernard, Professeur	Rapporteure, INSA de Rennes, France.
Wei Yang, Professeur	Rapporteure, Hunan University, Chine.
Anatoly Belonoshko, Professeur	Examinateur, KTH-Stockholm, Suède.
Amine Bouibes, Maître de Conférences	Examinateur, INSA de Toulouse, France.
Ali Zaoui, Professeur	Directeur de thèse, University of Lille, France.

Laboratoire de Génie Civil et géo-Environnement

Acknowledgements

First of all, I would like to take the opportunity to appreciate all the people, without whom this thesis would not have been completed.

I am especially appreciative to my respectful supervisor, Professor Ali ZAOUI, who made the present work possible. Your valuable advice and friendly guidance significantly contributed to the accomplishment of this work. Your spirit of dedication to investigation and love for science have been a great resource of inspiration. Your door was always open, and I enjoyed the precious discussions that not only helped shape my work but also motivated me to work harder to be able to continue to move further in my research.

My sincere appreciate go to Prof. Wassila Sekkal for her time, generosity and constant encouragement with suggestions.

I would also like to acknowledge the help of the committee members, Prof. Siham Kamali Bernard, Prof. Wei Yang, Prof. Anatoly Belonoshko, Prof. Fabrizio Cleri, and Dr. Amines Buibes, who agreed to review my thesis. Special thanks to the reporters Prof. Siham Kamali Bernard and Prof. Wei Yang for taking the time to carefully read and comment my work. Thank you all for your time and for the valuable feedbacks.

My devout gratitude must go to my family, to my dear parents, to my sister and to my girlfriend, for their endless love, support and inspiration.

Abstract

Improving the life-time of cement paste is a significant challenge in construction sector. Surface treatment approaches, such as surface coating, surface pore sealing, and surface impregnation, have been playing a significant role to improve the durability of cement-based structures especially in preventing surface deterioration and damage. Experimental investigations indicate that surface coating, acting as a physical barrier, is an effective way for enhancing the durability of materials by avoiding the penetration either of water or hazards substances. Due to the experimental observation limitations, there is an urgency need to deeper delve the atomic level to understand the mechanism behind the success hydrophobic behavior of cement surface modified with a nano-coating treatment.

Therefore, this dissertation adopts a nano-scale level study to understand and control the nano-coating process to engineer an impermeable hydrophobic Calcium-Silicate-Hydrate (CSH) surface through nano-coating of epoxy and rubber films under aggressive environment. To this end, Molecular Dynamics (MD) simulations based on a combination potential of a general force field (CLAYFF) and the consistent-valence force field (CVFF) have been employed to represent the interatomic interactions between CSH and epoxy or rubber films. A developed realistic model has been used to represent the CSH nanostructure.

The thesis is dedicated, first, to study deeply the hydrated surface properties of CSH paste in order to thoroughly understand the hydrophilic nature of the (001) CSH surface. Then, a fully investigation has been performed on the interfacial interaction and adhesion properties between epoxy resins nano-coating and CSH surface. For that, we use diglycidyl ether of bisphenol A (DGEBA) as epoxy monomer and *m*-phenylenediamine (MPD) as hardener. Thereafter, an in-depth analysis of a hydrophobic rubber nano-coating process onto CSH surface is explored. Four types of rubber are employed, as TPI (1,4-*trans*-Polyisoprene), CPI (1,4-*cis*-Polyisoprene), TPB (1,4-*trans*-Polybutadiene), and CPB (1,4-*cis*-Polybutadiene). Finally, the present work is devoted to analyze the interfacial deterioration process between epoxy/rubber nano-coating of CSH surfaces under aggressive environment, like a salty water (4 wt.% of NaCl).

Results obtained indicate that epoxy and rubber coated CSH surface energy are drastically dropped to the range of 33.7 mJ/m^2- 48.4 mJ/m^2, which extremely reduces the hydrophilicity of the CSH surface. The averaged contact angle between water-nanodroplet and rubber coated CSH surface is found in range of 92.85° and 98.11°. The calculated interfacial adhesion between organic-coatings

(epoxy and rubber) and CSH is in range of 49.42 mJ/m^2 to 102.81 mJ/m^2. Additionally, *m*-phenylenediamine (MPD) would highly improve the epoxy nano-coating efficiency. Regarding rubber nano-coating, it is found that coating process with TPI (1,4-*trans*-Polyisoprene) and CPB (1,4-*cis*-Polybutadiene) than CPI (1,4-*cis*-Polyisoprene) and TPB (1,4-*trans*-Polybutadiene) will enhance efficiently the impermeability of CSH paste. Under aggressive conditions, non-fully epoxy nano-coating is detached more distorted in 4 wt.% of NaCl solution due to the chlorine ions which are responsible to attack the CSH surface. A continuous well-distributed rubber nano-coating is capable to make CSH impermeable under harsh environment leading to a promising future for sustainable cementitious materials.

The doctoral thesis concludes the feasibility and reliability of nano-coating by rubber film to prevent the interfacial deterioration of CSH surfaces in aggressive environment and to improve the impermeability of nano-coated CSH surfaces for more durable cementitious materials .

Résumé

Améliorer la durée de vie de la pâte de ciment constitue un enjeu important dans le secteur de construction. Les approches de traitement de surface, telles que le revêtement de surface, le scellement des pores de surface et l'imprégnation de surface, jouent un rôle important dans l'amélioration de la durabilité des structures à base de ciment, en particulier dans la prévention de la détérioration et des dommages de la surface. Des recherches expérimentales indiquent que le revêtement de surface, agissant comme une barrière physique, est un moyen efficace d'améliorer la durabilité des matériaux en évitant la pénétration de l'eau ou de substances dangereuses. En raison des limites de l'observation expérimentale, il est urgent d'approfondir les étude au niveau atomique pour comprendre le mécanisme à l'origine du comportement hydrophobe de la surface du ciment modifiée avec un traitement de nano-revêtement.

Par conséquent, cette thèse adopte une étude à l'échelle nanométrique pour comprendre et contrôler le processus de nano-revêtement afin de concevoir une surface hydrophobe imperméable de silicate de calcium hydraté (CSH) grâce au nano-revêtement par un film d'époxy et de caoutchouc dans un environnement agressif. À cette fin, des simulations de dynamique moléculaire (MD) basées sur une combinaison potentielle d'un champ de force général (CLAYFF) et du champ de force à valence constante (CVFF) ont été utilisées pour représenter les interactions interatomiques entre le CSH et les films époxy ou en caoutchouc. Un modèle réaliste a été utilisé pour représenter la nanostructure CSH.

La thèse est consacrée, dans un premier temps, à étudier en profondeur les propriétés de surface hydratée de la pâte CSH afin de bien comprendre la nature hydrophile de la surface (001) de CSH. Ensuite, une étude approfondie a été réalisée sur l'interaction interfaciale et les propriétés d'adhésion entre le nano-revêtement de résines époxy et la surface CSH. Pour cela, nous utilisons l'éther diglycidylique du bisphénol A (DGEBA) comme monomère époxy et la m-phénylènediamine (MPD) comme durcisseur. Par la suite, une analyse approfondie du processus de nano-revêtement de caoutchouc hydrophobe sur une surface CSH est explorée. Quatre types de caoutchouc sont utilisés, comme le TPI (1,4-trans-Polyisoprène), le CPI (1,4-cis-Polyisoprène), le TPB (1,4-trans-Polybutadiène) et le CPB (1,4-cis-Polyisoprène). Polybutadiène). Enfin, le présent travail s'intéresse à l'analyse du processus de détérioration de l'interface entre les films de époxy/caoutchouc et la surface de CSH dans un environnement agressif, comme l'eau salée (4% en poids de NaCl).

Les résultats obtenus indiquent que l'énergie de surface des CSH recouverts d'e films d'époxy et de caoutchouc est considérablement réduite et sa valeur est de 33,7 mJ/m^2 à 48,4 mJ/m^2. Ceci réduit considérablement le caractère hydrophile de la surface du CSH. L'angle de contact moyen entre la nano-gouttelette d'eau et la surface CSH recouverte de caoutchouc se situe entre 92,85° et 98,11°. L'adhésion interfaciale calculée entre les revêtements organiques (époxy et caoutchouc) et le CSH est comprise entre 49,42 mJ/m^2 et 102,81 mJ/m^2. De plus, les résultats montrent que la m-phénylènediamine (MPD) améliorerait considérablement l'efficacité du nano-revêtement époxy. Concernant le nano-revêtement de caoutchouc, on constate que le processus de revêtement avec du TPI (1,4-trans-Polyisoprène) et du CPB (1,4-cis-Polybutadiène) améliorera efficacement l'imperméabilité de la pâte CSH. Dans des conditions agressives, le nano-revêtement partiel par l'époxy se détache de manière plus déformée dans une solution à 4 % en poids de NaCl en raison des ions chlore qui sont responsables de l'attaque de la surface CSH. Un nano-revêtement de caoutchouc continu et bien réparti est capable de rendre le CSH imperméable dans des environnements difficiles, ouvrant la voie à un avenir prometteur pour les matériaux cimentaires durables.

La thèse de doctorat conclut la faisabilité et la fiabilité du nano-revêtement par un film en caoutchouc pour prévenir la détérioration interfaciale des surfaces CSH dans un environnement agressif et pour améliorer l'imperméabilité de la surface CSH nano-revêtue pour des matériaux cimentaires plus durables.

Contents

List of Figures

List of Tables

Chapter 1:

General Introduction

1.1. Research background

The most widely used building materials in civil engineering is cement binding paste, which plays a significant role in building industry. Nevertheless, its surface degradation is most of related to reinforcement bars corrosion, chemical attack (chlorides, sulfates and magnesium ions), microorganism bacteria erosion and surface calcium leaching by water penetration. All these disadvantageous processes reduce its mechanical strength and sustainability. Therefore, improving the durability of cement-based materials is an extremely crucial challenge in building domain. The most common acceptable effective strategy for delaying the surface deterioration of cement paste is to conduct an effective surface treatment [1-4]. In general, the surface treatment can be conducted into three main approaches: (i) apply a continuous films with various thickness onto the surface, named coating [5-7]; (ii) use a specific pore barrier, named sealing or blockage [8]; (iii) Impregnate both concrete's surface and the interior surface composing the pore, named impregnation or pore liner [9, 10]. Nevertheless, the pore sealing might be able to reduce the surface porosity of concrete but couldn't make it impermeable [8]. Though, either coating or impregnation are capable to reborn a hydrophobic performance to concrete [5, 10]. Moreover, experimental results indicate that the surface energy of cement paste is in range of 657 mJ/m^2 to 1750 mJ/m^2 [11, 12], which contributes to hydrophilic performance. Obviously, one effective way of reducing the hydrophilicity of the paste is by decreasing its surface energy. Hereby, using low surface energy materials to conduct a hydrophobic surface coating is an effective way for enhancing the durability of cement paste by avoiding the infiltration either of water or hazards substance that use water as medium [13, 14]. Due to the experimental technical limitations to understand the mechanism behind how the success hydrophobic coating make CSH surface impermeable under severe condition, there is an urgency need to deeper delve the atomic level of the nano-coating procedure. The Nobel Prize winning physicist Richard Feynman first introduced the concept of nanotechnology during his famous lecture in 1959: "*There's Plenty of Room at the Bottom*", which indicates that the possibility of manipulating matter on an atomic scale [15]. Nanotechnology comprises two main methods: (i) deconstruct the size of larger bulk materials from macro-scale level into the nano-scale level while remaining its original properties without atomic-scale level control, called "top-down" method. (ii) Engineer materials from atomistic level by a process of assembly or self-assembly, named the "bottom-up" method, also called "molecular nanotechnology", which is introduced by Drexler et al. [16]. Thanks to the developing of nano-scale modeling and numerical simulation tools, this

thesis takes the “bottom-up” method, which enables us the possibility for an in-depth analysis regarding to the hydrated surface properties of nano-granular CSH paste. In addition, it is capable to quantify the interfacial interatomic interactions between surface coating (epoxy and rubber) and CSH components via the radial distribution function (RDF), and deduce how the interfacial adhesion between them is and what is the principal constituent responsible to reduce the hydrophilicity of CSH surface. Further, it is possible to shed lights of the implication inducements that how rubber nano-coating makes CSH paste impermeable under aggressive environment [17-19].

1.2. Research objectives

The implication mechanisms of how a success hydrophobic impermeable coating treatment performs onto cement paste in a harsh condition have not been well explored. The main goal of this thesis is to an in-depth investigation of conducting an effective impermeable hydrophobic surface coating to cement paste. The influence of the dosage and the structure of coating agents to coating efficiency would be studied. The interfacial interatomic interaction in coating/CSH interface and the adhesion between them would be investigated as well. Further, the deterioration at the interface of coating/CSH and impermeable behavior of coating would have been delved in either salty water (4 wt.% of NaCl) or pure water solution. To that end, by means of molecular dynamics simulations, the objectives of this thesis are as following:

1. Investigate the hydrated CSH (001) surface properties using a developed realistic CSH model of Pellenq. The wettability of the (001) surface would be studied by using a water-nanodroplet to calculate the contact angle as well as the work of adhesion between them. The structural properties and surface energy of the CSH structure would be also calculated.
2. Delve the interfacial interaction between effective epoxy resins coating and CSH (001) surface by varying the initial distance between them. Investigate the decreased hydrophilicity of epoxy coated CSH surface by evaluating the contact angle between water-nanodroplet and coated surface.
3. Determine the dosage of epoxy resins coating agents by changing the weight content of the agents until making CSH ideally coated. The interfacial adhesion between epoxy coating and CSH surface would be further evaluated as well as the free energy of coated CSH surface.
4. Probe into a hydrophobic nano-coating process. Using nano-rubber coating film instead of epoxy resins agents further investigate the potential of surface coating that reverse hydrophilic CSH surface nature to hydrophobic performance. Quantify the interatomic interaction and the interfacial

adhesion between effective nano-rubber coating and CSH surface. Demonstrate the hydrophobic behavior of rubber coated CSH surface using a water-nanodroplet to calculate the contact angle between them. The influence of rubber dosage to coating efficiency would be studied by differing the weight content of rubber. The different atomistic rubber structures would have been used to investigate the structure effect to coating effectiveness as well.

5. Investigate the interface degradation process in case of between non-fully epoxy coating and CSH under either salty water solution or pure water solution environment by examining the variation of interfacial fracture toughness between them. Determine the principal interfacial ionic bond interaction in against with the deterioration behavior. Further, examine both fully epoxy coated CSH and rubber coated CSH under harsh condition to deduce what implication inducements that make CSH paste impermeable under aggressive environment.

1.3. Thesis Organization

To improve the lifetimes of cementitious composites, there is a crucial need to delve the implication inducements behind the impermeable coating cement paste under aggressive condition. By means of atomistic molecular dynamics simulations, this thesis first investigates in-depth the hydrated surface properties of CSH paste. Next, it quantifies the interface interatomic interaction between coatings (epoxy and rubber) and CSH constituents to introduce what is the principal constituent that contributes to the interfacial adhesion and look for a success procedure of a hydrophobic rubber nano-coating onto CSH paste. Then, under either salty water solution or pure water solution environment, it presents the degradation process of the interfacial interatomic bond in the interface between epoxy coating and CSH paste. Finally, it investigates the inducements behind the impermeable behavior of rubber nano-coating onto CSH surface.

In chapter 1, a general context of the research is firstly introduced, then the objectives of this thesis is clarified as well as the outlines of the thesis's work.

In chapter 2, we presented the academic investigation findings of cement paste materials. The introduction first goes to the understanding of the atomic structure of cement paste and its evolutions. Next, the multiscale morphology of CSH have been presented. Last, we summarized the latest experimental and theoretical investigation results for improving the durability of cement paste by conducting a surface coating treatment.

In chapter 3, we introduced the molecular dynamics (MD) simulation method utilized in this thesis, including the main numerical schemes, simulation principles and interatomic potentials.

Chapter 4 is devoted to a deep analysis of the hydrated surface properties of CSH paste related to the wettability and free energy of its (001) surface as well as the work of adhesion between the water-nanodroplet and CSH surface.

In chapter 5, it is dedicated to enhance the resistance to water infiltration into the CSH paste. In case of the improvement of hydrophobicity behavior by coating CSH surface with epoxy resins film. The dosage of epoxy resins is determined by varying the weight content of epoxy resins until the CSH ideal coated. Further, the interfacial bonding interaction and the adhesion of epoxy resins coated on (001) surface of CSH paste are delved as well as the free energy of epoxy coated CSH surface.

In chapter 6, the work is devoted to understand the mechanism behind the success hydrophobic behavior of CSH surface coated by a rubber nano-coating film. Four types of atomistic rubber structures are utilized to deeper analyze the atomic level of nano-coating procedure. The free energy of effective rubber coated CSH surface is estimated, and the hydrophobic behavior of coated surface is further examined using a water-nanodroplet in contact with. The interfacial interatomic interactions between rubber and CSH constituents are quantified as well as the adhesion between them.

In chapter 7, under either salty and pure water solution, the deterioration process between non-fully epoxy coating and CSH paste is studied. The principal ionic bond interactions contributes to the fracture toughness in the interface of non-fully-coating/CSH is investigated. Moreover, both fully epoxy coated CSH and fully rubber coated CSH are examined under the harsh environment. The behind inducements that make nano-coated CSH impermeable are further deduced.

In chapter 8, a general conclusion and perspectives are presented.

Chapter 2:

Cement paste materials

2.1. Understanding the structure of Cement paste: model construction and its applications

Adopting "bottom-up" approach, it is possible to enhance the traditional performance of hardened cement paste obtained in macro-scale level from atomic-scale level, which is essentially to explore the nanostructure of the nano-granular Calcium-Silicate-Hydrate (CSH) binding paste [20]. Taylor et al. [21] have done lots of work concerning the atomic structure of CSH, which is considered as an imperfect disordered layer structure hybrid both jennite [22] and 14 Å tobermorite [23]. Nevertheless, Pellenq has questioned the Taylor's model that there are two incompatible properties to real CSH, which are Ca/Si ratio and its density. Pellenq et al. [24] have then proposed a realistic CSH nanostructure with chemical composition of "$(CaO)_{1.65}(SiO_2)(H_2O)_{1.75}$" from the tobermorite 11 Å [25] with a Ca/Si ratio of 1.65 and a density of 2.56g/cm^3. These values are in good agreement with the experimental findings of Allen A J et al. [26] with Ca/Si ratio and density equal to 1.7 and 2.604 g/cm^3, respectively.

A number of investigations utilized Pellenq's model to represent the atomic-structure of CSH to delve its structural and mechanical properties. Qomi et al. [27] indicated that structural properties of confined water inside CSH depended on the substrate composition by using REAXFF potential [28]. Bauchy et al. [29] showed that structurally CSH has tobermorite-like layered structure but the hydrated species are amorphous based on Pellenq's model. Laanaiya et al. [30] have employed the developed Pellenq's model to study the structural and mechanical performance of modified CSH by embedding Fe_2O_3 nanoparticles using the REAXFF force field [31]. Additionally, Sekkal et al. [32] have employed this model to analyze the porosity effects on the mechanical properties and the structural stability of (001) CSH surface. By means of molecular dynamics tools, they indicate an improvement of the strength of CSH in interface with carbonate mineral when the gel porosity is roughly 30 % [33] and more recently while incorporating C_{60} nanoparticles [34].

Nevertheless, the surface properties of CSH still remains to explore at the nano-scale level, in which is directly related to the surface durability of cement paste. Wetting, one of the important characteristics of surface properties, has attracted a big attention of many researchers in various fields. The level of wetting [35] is measured by wettability, which is the ability of a solid surface to remain in contact with a liquid that is highly involved with its surface energy. Moreover. Brunauer et al. [36, 37] have measured the surface energy of tobermorite ($Ca_3Si_2O_7{\cdot}2H_2O$) which is found in the range of 386 erg/cm^2 to 450 erg/cm^2. Wittmann [11] has indicated that the surface

energy of hardened cement paste depends on the water of cement ratio and revealed its value as 657 erg/cm^2 and 1370 erg/cm^2, corresponding to the hardened cement paste with the water to cement ratio of 0.6 and 0.45, respectively. The high surface energy of cement paste induces a hydrophilic behavior, which means its surface is easier to wet than those with low surface energy. Li et al. [38] showed that the contact angle between water and mortar is cured dependent and its value is found equal to 33.34° and 24.5° corresponding to cured 3 days and 28 days, respectively. Klein et al. [39] have indicated the initial metastable contact angle between water and cement mortar equal to 21.7° and 26.0° corresponding to two different grain size distribution inside cement mortar. Otherwise. Franzoni et al. [40] have demonstrated that the contact angle between water and concrete is 32° and 36° corresponding to the ordinary concrete and the improved durability concrete, respectively. However, the hydrated surface properties of CSH paste remain misunderstood from atomic level. For this reason, the first propose of this thesis is, at nano-scale level, to investigate the wettability and free energy of (001) surface of CSH paste as well as the work of adhesion between the water-nanodroplet and CSH surface.

2.2. Multiscale morphology of CSH

2.2.1. Introduction

Calcium-Silicate-Hydrate (CSH) is the mainly hydration products of cement, which occupies 60% to 70% volume in hardened cement paste. Calcium hydroxide (CH), also called portlandite, has 10% to 20% volume fraction in cement paste. Due to the variation of hydration time, temperature and the impurities content, the CH size ranges in 10 μm to 100 μm. Finally, the minor components, such as the calcium aluminates, the ettringite and the calcium ferrites occupy approximately 15% volume of cement paste [41, 42]. The binding role of Calcium-Silicate-Hydrate (CSH) paste in concrete is significant to the mechanical strength of concrete. Its surface performance significantly related to the durability of concrete. Additionally, CSH is structurally recognized as a poorly ordered phase, its microstructure is characterized as gel-like morphology due to the presenting of nanometer pores [43-45]. The schematic morphology of CSH from macro-scale level to nano-scale level as given in Fig. 2.1.

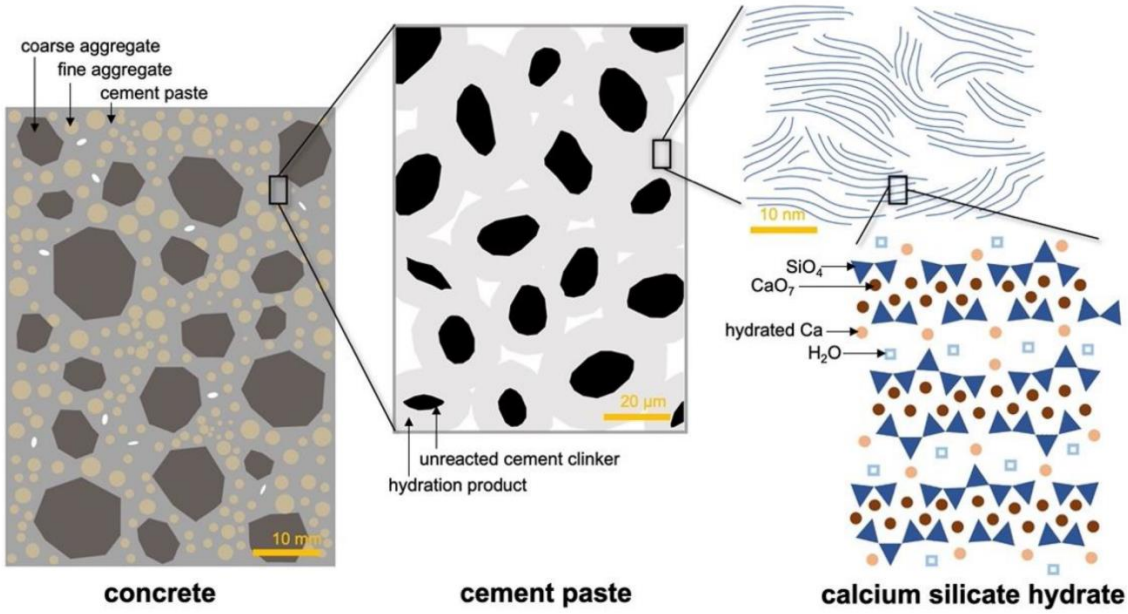

Fig. 2.1. Schematic morphology of CSH at multi-scale [46].

2.2.2. Microstructure of CSH

Regarding the morphology of hydrated cement paste at micro-scale level, Taplin [47] proposed a method that it “convenient to designate those products which lie within the original boundaries of the clinker particles ‘inner’ products, and those which lie ‘outside’ ‘outer’ products.” This method is well-supported by a number of investigations for cement materials by using the high resolution technique either transmission electron microscopy (TEM) [48-51] or by X-ray mapping [52, 53]. During the hydration of tricalcium silicate and CH with water, two different CSH gels are formed that they can be designated as being either "inner product" (Ip) or "outer product" (Op). In which Ip CSH forms within the original particles boundary, and Op CSH forms in the origina water-filled region [52]. Moreover, an Ip CSH in the larger cement grains has a typical fine-scale and homogeneous morphology, as shown in Fig. 2.2 [42]. Nonetheless, the Ip region contains the unreacted belite and CH [52]. An Ip CSH from larger slag grains indicate the typical behavior of fine-scale homogeneous morphology, but it chemically has high content of Mg and Al as given in Fig. 2.3 [48, 50].

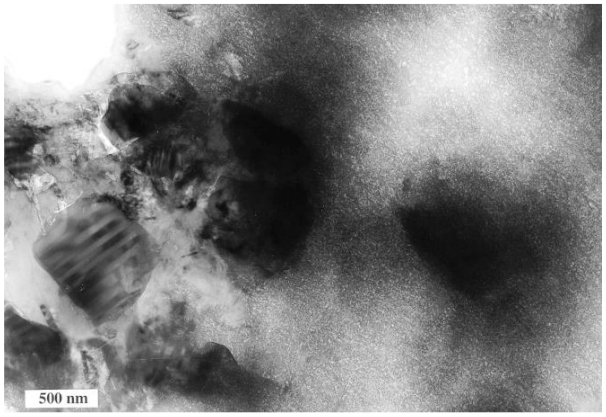

Fig. 2.2. TEM of an Ip CSH with the fine-scale morphology (centre-right), unreacted belite (left), and CH (surrounding the belite) [42].

Fig. 2.3. TEM of a slag inner product region (lower left-centre), fine fibrillar Op CSH (upper right-centre), an AFm plate (upper left-centre) and several AFt relicts along the Ip/Op interface (50% slag blend, W/S = 0.4, 20°C, 3 months) under Mg, Al-rich precipitates condition [48].

The hydrated cement products contain a less dense product with massive porosity surrounded by a region of quite dense CSH, as presented in Fig. 2.4 [42, 50, 52]. In hybrid of cement-slag paste, with increasing the content of slag the fibrillar CSH morphology is gently replaced by the foil-like morphology as given in Fig. 2.5 [48]. Furthermore, the foil-like morphology would decrease the porosity of CSH by efficiently filling voids without leaving large interconnected capillary pores. CSH morphology changed from fibrillar to foil-like is a significantly inducement to improve the durability for CSH containing slag system [54].

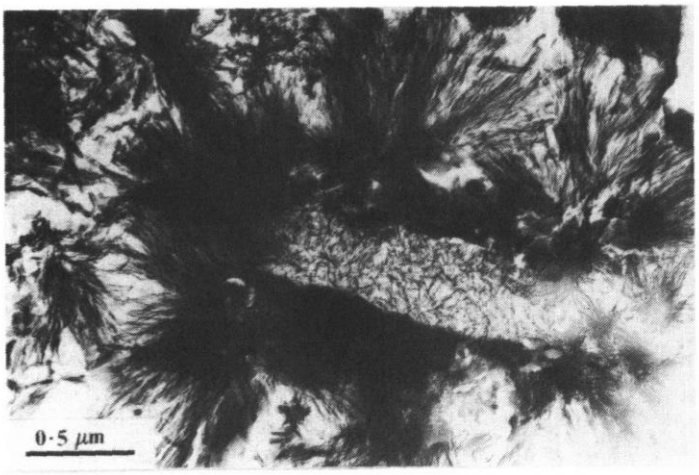

Fig. 2.4. Dense CSH wall around hydrated particle with lower density interior containing substantial porosity in hydrated cement paste [50].

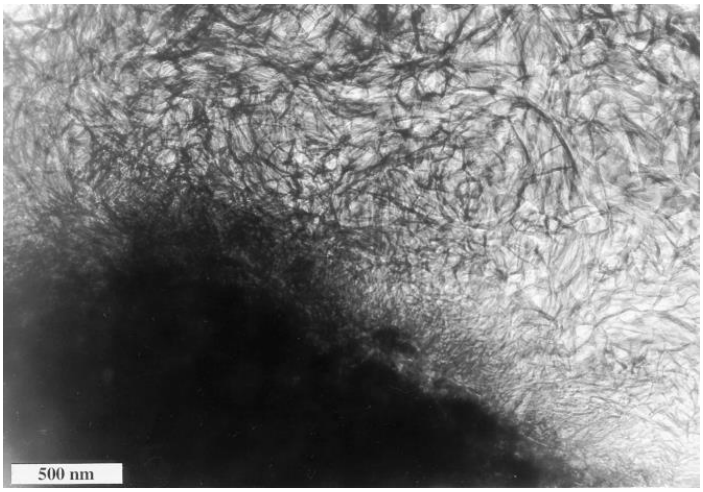

Fig. 2.5. TEM of foil-like Op CSH in a water-activated slag hydrated paste. From [42].

2.2.3. A realistic nanostructure of CSH

Pellenq et al. [24] have been proposed a realistic CSH model, "$(CaO)_{1.65}(SiO_2)(H_2O)_{1.75}$", with two comparable properties which are Ca/Si ratio of 1.65 and density of 2.56 g/cm^3. These findings are in good agreement with the experimental investigations of Allen A J et al. [26] that Ca/Si ratio and density equal to 1.7 and 2.604 g/cm^3, respectively.

The realistic CSH structure is constructed starting from a dry tobermorite of interlayer spacing roughly of 11 Å [25]. The initial Ca/Si ratio of the tobermorite is 1. To increase the Ca/Si ratio,

some SiO_2 are randomly removed following the experimental data of Q_n fraction factor (Q_0 = 10%, Q_1 = 67% and Q_2 = 23%) measured by nuclear magnetic resonance (NMR). The meaning of subscript n in Q_n is the number of bridging oxygen atom bound to silicon in a silicon chain. Thus Q_o is a single silicate monomer, a silicate dimer would have two Q_1, a silicate pentamer would have three Q_2. Consequently, a defective CSH model has a Ca/Si ratio of 1.65 with a distribution of Q_0 = 13%, Q_1 = 67% and Q_2 = 20%.

Moreover, Bauchy et al. [29] based on Pellenq's model deeper investigated the atomic order of realistic CSH structure using REAXFF force fields [28]. The outcomes indicate that, when taking all the CSH atoms into account, its atomic structure is closer to a glass structure rather than a crystal model. Nonetheless, since the silicate chains are not completely amorphous, and surrounding by nonrandom distribution of calcium atoms. Hence, CSH remains some layered performance similar to a tobermorite structure. On the other hand, REAXFF potential allow water molecules dissociate into hydroxyl groups because of the water interaction between interlayer and intralayer. Therefore, the water molecules and hydroxyl groups exhibit a completely glassy spatial distribution, which indicates that these hydration part are totally amorphous. Hence, the atomic order of CSH can be qualified as an intermediate structure between a crystal-like and a glass-like structure.

2.3. Durability of cement paste: Surface coating onto cement paste

Surface coating performs as a physical barrier to prevent harmful substances or water penetration into cement based composites by forming a continuous film. Organic polymer coatings have been being attracted researchers since its good protective performance in last few decades. The investigations indicate that epoxy-based coatings exhibit a remarkable performance in enhancing concrete against either the microbiologically influenced erosion in cooling tower basins or the salinity of marine induced corrosion [55, 56]. It also improved the properties of both cured and non-cured concrete exposed to a sulfate rich condition as well [57]. For instance, epoxy coated calcium aluminate cement mortar after filed exposure test in the cooling tower basins as given Fig. 2.6. Though both epoxy and polyurethane coatings show good behavior in reducing the water adsorption into concrete but polyurethane coating shows a better performance in decreasing the chloride diffusion coefficient than epoxy coating [58].

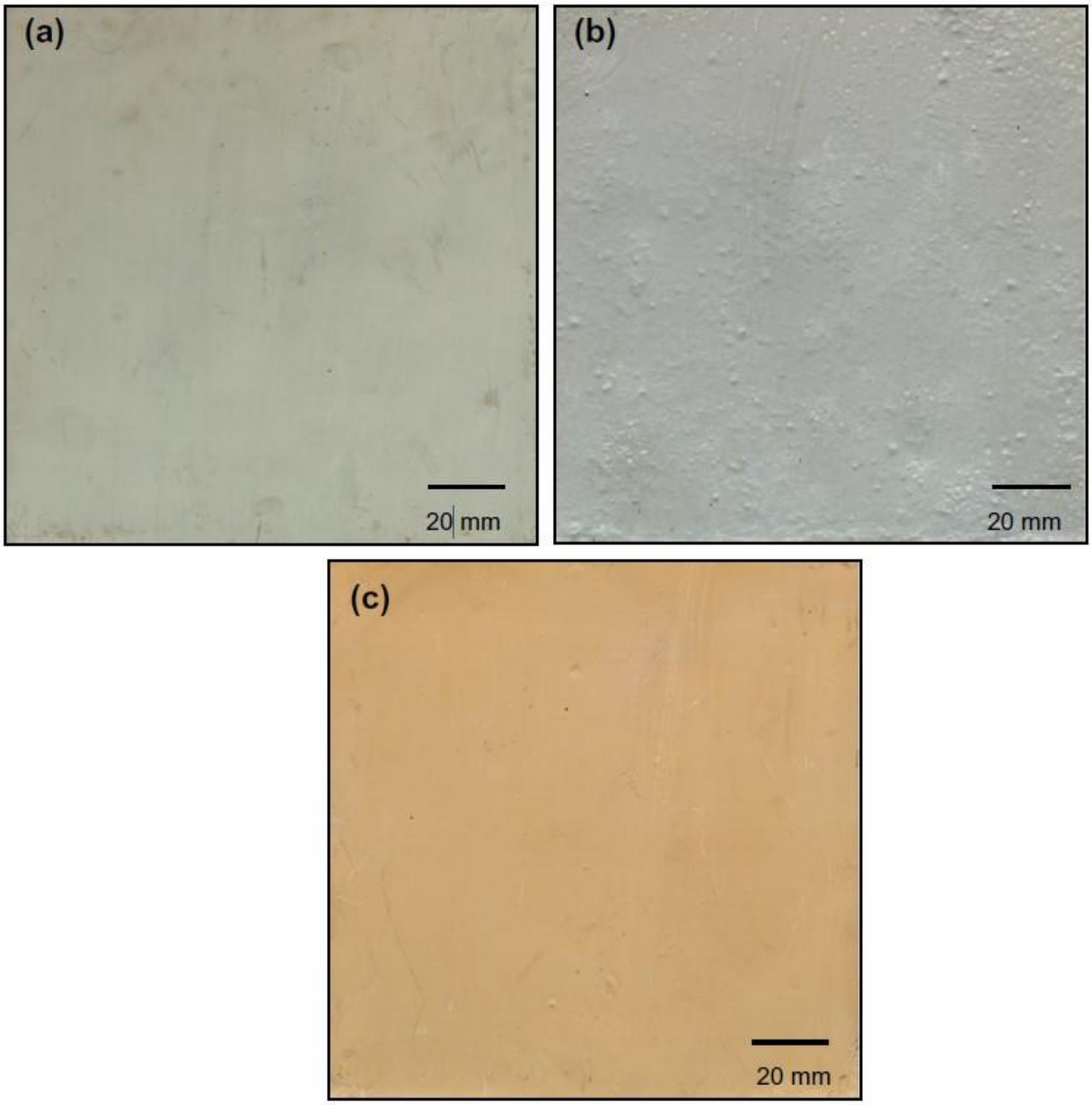

Fig. 2.6. Appearance of (a) Amercoat 351®; (b) Amercoat 385® and (c) Sikagard 62® all showing good condition after field exposure [55].

Additionally, concrete coated by two polyurethane-based coating agents show quite different behavior as given in Fig. 2.7. Furthermore, under sewer environment, one of the coated concrete has extended its lifetime to 14 times, and the other one extended its durability up to 57 times [59].

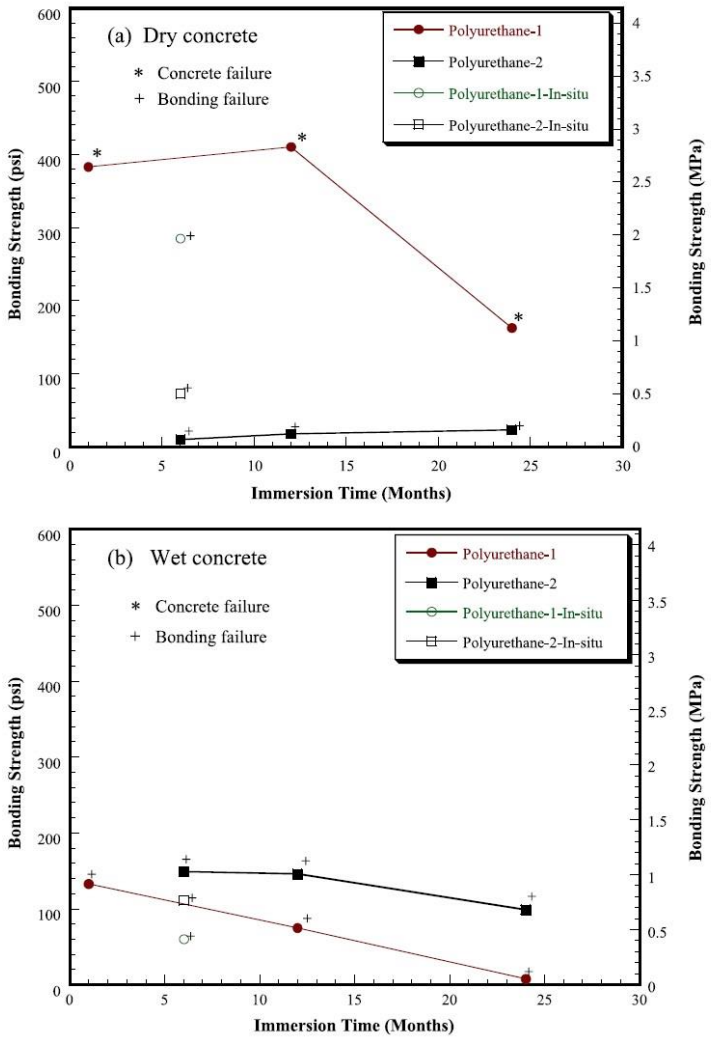

Fig. 2.7. Bonding strength of coated concrete in (a) dry concrete and (b) wet concrete [59].

Nonetheless, the surface energy of epoxy coated cement paste with a coating concentration of 1% to 10% is extremely decreased. The values are found in range of 28.2 mJ/m^2 to 53.1 mJ/m^2 in the case of water to cement ration of 0.3 [60]. Therefore, the related hydrophilicity is highly decreased as well, given the contact angle between water and the pure epoxy resin coated concrete is 77.5°. It is improved up to 96.1° when 0.3 wt. % of graphene oxides is added into the pure epoxy coating [61]. However, Polydimethylsiloxane coating is able to reborn concrete a superhydrophobic performance that forming a static contact angle of 164° between water and coated concrete. The results of 3D topographic profiles of Ultra-High Performance Concrete (UHPC) surface micro-pillared by polydimethylsiloxane (PDMS) and the contact angle are presented in Fig.2.8 [62]. In addition, the super-hydrophobicity of the coated surface is

significantly dependent on not only the coating agent type but also on the spray duration [5]. The polymer modified cementitious coating could also highly decrease the water content and chloride infiltration into reinforcement concrete under wet condition [63]. On the other hand, surface impregnation has the same potential as surface coating to protect concrete. Silane surface impregnation is valid for both un-cracked concrete and reinforced concrete by drastically decreasing the water absorption as well as preventing the chloride penetration. Nevertheless, the chloride infiltration cannot be fully prevented if there is a crack generated after impregnation for the reinforced concrete [9]. Additionally, Polybutadienes containing alkoxysilyl groups impregnated concrete could highly decrease the water absorption, and it makes the concrete hydrophobic, the contact angle is up to 105.8° [10]. The surface morphology of functionalized polybutadiene impregnated concrete as presented in Fig. 2.9. More recently, at atomic-scale level, fluoroalkylsilane modified CSH surface shows a superhydrophobic behavior [64], and isobutyltriethoxy silane modified ettringite improves its hydrophobicity [65].

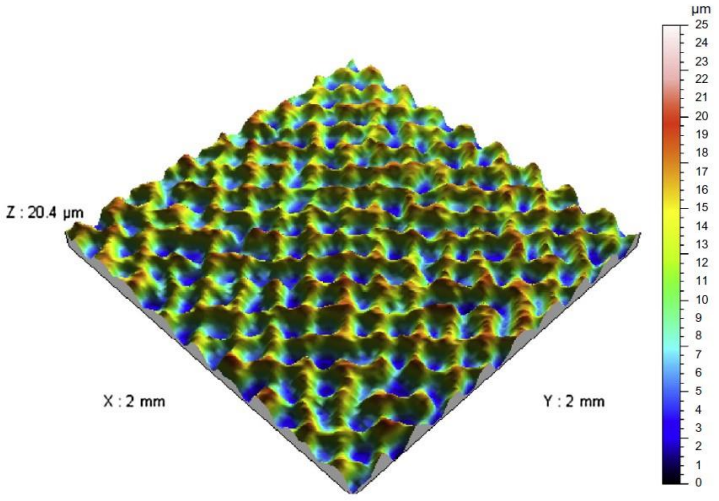

(a)

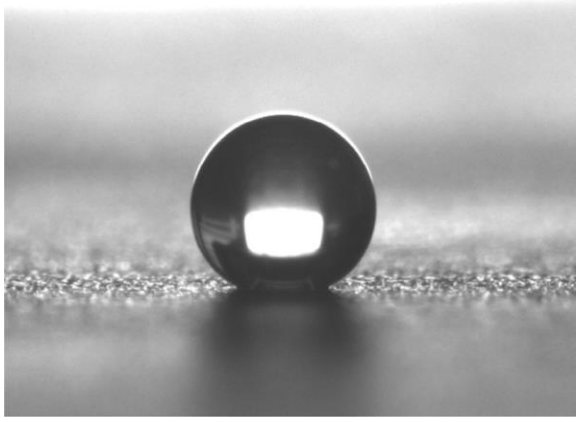

(b)

Fig. 2.8. 3D topographic profiles of UHPC/micro-pillared PDMS (a), Image of a drop of water deposited on UHPC/micro-pillared PDMS (b)[62].

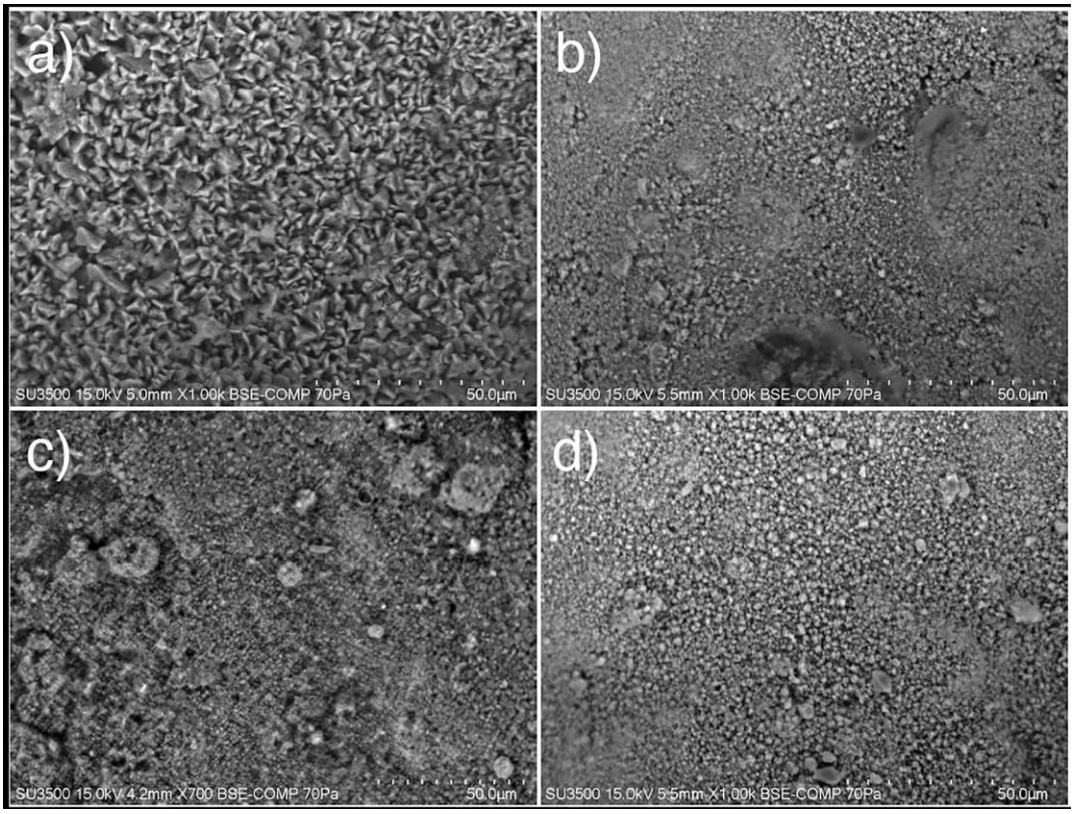

Fig. 2.9. SEM images of the surface of the uncoated concrete sample (a), and concrete samples coated with PBT1 (b), PBT2 (c), and PBT3 (d) solutions in Exxsol D60 [10].

After normal aging, the degradation of interfacial bond and adhesion at the interface between coating and concrete would reduce its lifetimes.[66]. Experimental findings indicate that the work of adhesion between epoxy coating and cement paste are 102.79 mJ/m^2 and 90.17 mJ/m^2 corresponding to 2 and 28 days hydration of cement, respectively [6]. However, a nonreversing weakening behavior is observed in bond strength of concrete/epoxy/fiber reinforced polymer structure in moisture cyclic environment [67]. Furthermore, the interfacial fracture toughness was deteriorated up to 77% in concrete-epoxy interface of fiber reinforced polymer system under the interacted effect of sustained load and moisture [68]. The oxidation and hydrolysis would pronouncedly reduce the scratch resistance of both isocyanate and epoxy acid coatings under an

outdoor weathering environment [69]. The cracks would be formed in the epoxy-based coating surface after ultraviolet radiation exposure, and its depth and number dependent on the exposure time as presented in Fig. 2.10 [70].

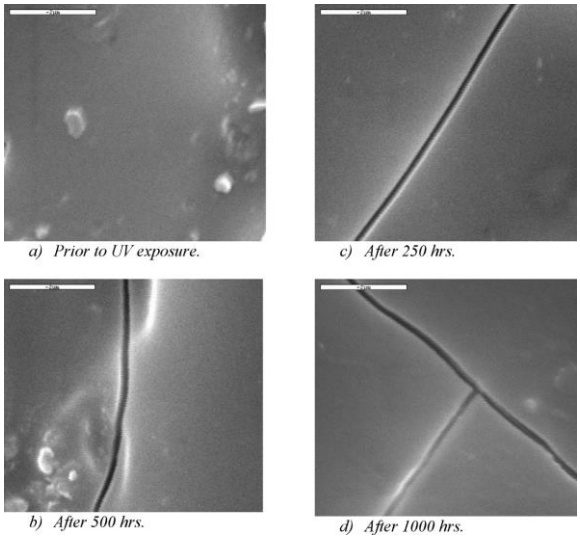

Fig. 2.10. SEM images for epoxy-based coating surface before and after ultraviolet (UV) exposure. [70].

Nonetheless, Aged epoxy coating exhibited a superior resistance in against chloride ion penetration, and its interfacial adhesion strength is comparable to polyurea coating unaged subjecting ultraviolet-condensation exposure environment [71]. Due to the experimental observation limitations, there is a lack of the information to the mechanism behind the success hydrophobic performance of coated CSH. Further, both the understanding of interfacial deterioration mechanism behind in the interface of coating/CSH and the implication parameters of how a success impermeable coated cement paste performed are not well explored. However, the investigations regarding to unsolved problems still wait to explore at atomistic level, which would enable us to have more understanding at nano-scale level, to be able to understand and control the performances observed at macro-scale level. Therefore, this thesis then propose, at nano-scale level, by means of molecular dynamics simulations, to quantify the interfacial interatomic interactions between organic coatings (epoxy and rubber) and CSH constituents via the RDF function, and study how the interfacial adhesion between them is and what is the principal constituent contribute

to decrease the hydrophilicity of CSH surface. Moreover, to understand the degradation of interfacial interatomic bond in the interface between epoxy coating and CSH paste in either salty water solution or pure water solution environment. Further, to delve the behind inducements of what remarkable properties are responsible for making the impermeable rubber coated CSH under severe condition.

Chapter 3:

Molecular dynamics method

3.1. Introduction

Molecular dynamics simulation is a powerful computational method to analyze the physical movements of atoms and molecules. The interatomic interaction between atoms or molecules are described using the interatomic force fields potentials. In a fixed period of time, its trajectories are calculated by numerically solving Newton's equations of motion of each interacting atom in a system, therefore predicting a view of the dynamic evolution of the system. Due to the advances capacities in MD computational method, it has been evolved into a significant and widely used theoretical tool, which can be used in chemistry, physics, and biology fields to predict macroscopic behavior from a atomistic dynamical performance for many different types of systems, including gases, liquids, solids, surfaces, and clusters [72-75]. The normal process of conducting a MD simulation is as followings: first of all, to construct the atomistic geometry of the materials, then define the interatomic interaction of the system, next step is solving Newton's equations of motion for the system, the following is choosing the environment of the simulation after the initialization and energy minimization of the structure geometry. The last step is calculating the expected properties after the integration scheme. The flowchart of the numerical approach as given in Fig. 3.1. The initial atomic positions of materials are generally based on the results from X-ray or NMR experimental data. Nano-scale modeling is concerned as alternatively utilized to construct the initial structural geometry when the experimental data are lacks. Moreover, the simulation boxes vary in a series of shapes, such as the cubic, triclinic, rectangular prism and the truncated octahedron geometries, as long as they can perfectly be put into a three dimensional crystal.

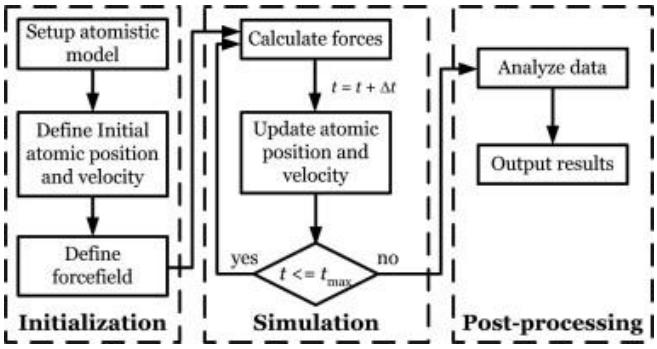

Fig. 3.1. Numerical approach of MD simulation. From [74].

3.2. Simulation principles

3.2.1. Periodic boundary condition

Periodic boundary condition (PBC) is a set of boundary condition aiming to approximate an infinite system by using a unit cell. In MD simulations, if the simulation box has PBC conditions, when one atom passes through one side of the box boundary, its image would re-appear on the opposite side of the box boundary with the same velocity. This principle is expressed in Fig. 2 in case of two-dimensional PBC condition [76]. Moreover, in PBC condition, a particle not only interacts with the other particles of the system but also with their periodic images, which extremely increases the amount of the interacting pairs. To address out this problem, a cut-off distance of r_{cut} is used, which means that the interaction would be ignored if the distance between two particles larger than the r_{cut}. Additionally, the minimum image convention considering that a particle i would interact with the closest image of a particle j and neglect the other images. For instance, in Fig. 3.2 that particle 2 would rather interact with particle 3′ than particle 3. The cut-off distance can be expressed to $r_{cut} \leq \frac{L_{unitcell}}{2}$, which means the r_{cut} smaller than half the unit box length. Three-dimensional PBC are useful and capable for predicting the performance of macro-scale systems, such as gases, liquids, and solids.

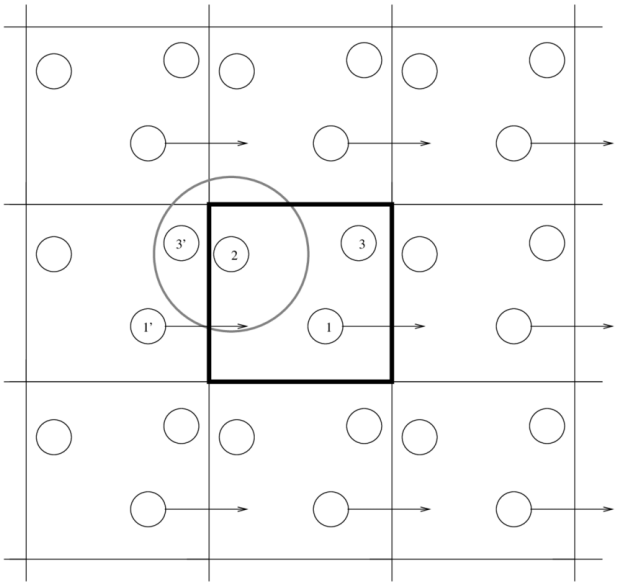

Fig. 3.2. Two-dimensional PBC condition, Particles 1′and 3′ are periodic images of particles 1 and 3, respectively [76].

3.2.2. Solving Newton's equations of motion

If the mass of a matter does not change with time, than the time derivative of the momentum acts only upon the velocity, since the time derivative of the velocity is the acceleration, thus the force equals the product of the mass and the acceleration, additionally, the acceleration is the second derivative of position with respect to time. Based on the well-known classical mechanics, therefore, the equation of motion of N particles are written as following Eq. (3.1).

$$F_i(t) = m_i \frac{d^2 r_i(t)}{d^2 t} \, , i \in \{1 \cdots N\} \tag{3.1}$$

Where F_i is the force upon particle i related to the positions of other particles j, and it can be derived from the interatomic potential function $\Phi(r_{ij})$, m_i and r_i are the mass and the position vector of particle i, respectively.

$$F_i(t) = -\Sigma_{i \neq j} \frac{\partial \Phi(r_{ij}(t))}{\partial r_{ij}(t)} \tag{3.2}$$

Where $r_{ij}(t) = |r_i(t) - r_j(t)|$.

3.2.3. Time integration

There is no analytical solution to the equations of motion as expressed in Eq. (3.1) for a systems of more than two atoms. There are a series of integration algorithms have been proposed for solving the problem, such as Verlet, Velocity Verlet, Predictor-Corrector and Gear Predictor-Corrector algorithms. The Verlet algorithm is the simplest and most commonly used integrator [77, 78]. The basic idea of Verlet algorithm is derived from two third-order Taylor expansions as following Eqs (3.3) and (3.4).

$$r_i(t + \Delta t) = r_i(t) + \frac{dr_i(t)}{dt}\Delta t + \frac{1}{2}\frac{d^2 r_i(t)}{dt^2}\Delta t^2 + \frac{1}{3!}\frac{d^3 r_i(t)}{dt^3}\Delta t^3 + 0(\Delta t^4) \tag{3.3}$$

$$r_i(t - \Delta t) = r_i(t) - \frac{dr_i(t)}{dt}\Delta t + \frac{1}{2}\frac{d^2 r_i(t)}{dt^2}\Delta t^2 - \frac{1}{3!}\frac{d^3 r_i(t)}{dt^3}\Delta t^3 + 0(\Delta t^4) \tag{3.4}$$

Summing Eqs (3.3) and (3.4) together and simplify, the position of a particle i at $t + \Delta t$ can be deduced as presented in Eq. (3.5).

$$r_i(t + \Delta t) = 2r_i(t) - r_i(t - \Delta t) + \frac{d^2 r_i(t)}{dt^2}\Delta t^2 + 0(\Delta t^4) \quad (3.5)$$

This is the basic form of the Verlet algorithm, which is simplicity and good stability. Nevertheless, a problem with this version of the Verlet algorithm is that velocities are not explicit. The velocity, which is the first derivative of position with respect to the time, could be calculated by considering the first order central difference. Using Eq. (3.3) subtract Eq. (3.4), the velocity of particle i at time t as given in Eq. (3.6).

$$V_i(t) = \frac{r_i(t+\Delta t) - r_i(t-\Delta t)}{2\Delta t} + 0(\Delta t^2) \quad (3.6)$$

However, this expression has the second order error rather than the fourth order error. To solve this problem, an improved Verlet version called velocity Verlet algorithm [79] is proposed as given in Eqs. (3.7) and (3.8).

$$r_i(t + \Delta t) = r_i(t) + V_i\Delta t + \frac{1}{2}a_i(t)\Delta t^2 \quad (3.7)$$

$$V_i(t + \Delta t) = V_i(t) + \frac{a_i(t) + a_i(t+\Delta t)}{2}\Delta t \quad (3.8)$$

Where r_i, V_i and a_i are the position, velocity and acceleration of particle i.

3.2.4. Energy minimization

In molecular dynamics simulations, the minimum energy state of the molecular system have been being attracted the researcher's attention, which is related to the stable configuration of the system corresponding to global and local minima on their potential energy surface. The initial molecular structures derived from experimental data are almost have high energy. Therefore, the energy minimization is utilized to calculate the initial equilibrium state of the system. It starts from a non-equilibrium state using the numerical process of optimization to move atoms to decrease the

net forces, which is the gradients of potential energy on the atoms until it becomes negligible. A well-established algorithm of energy minimization could be an efficient tool to optimize the molecular structure, such as the Polak-Ribiere version of the conjugate gradient (CG) algorithm, Hessian-free truncated Newton algorithm and steepest descent algorithm.

3.2.5. Ensembles

In molecular dynamics simulations, the simulation environment can be represented in different conditions corresponding to different ensembles, such as NVE, NVT, NPT and μVT ensembles. Where N is the number of atoms of the system, V is the volume of the system, E is the energy of the system, T is the temperature of the system, P is the pressure of the system, μ is the chemical potential. For instance, if a simulation is under NPT ensembles, thus the simulated system will be under a constant number of atoms, a constant of pressure and a constant temperature during the simulation time.

3.3. Force fields

A force field is a mathematical expression describing the relationship between the energy of a system and the coordinates of its particles. The interatomic potential energy is analyzed by a set of parameters, which are normally obtained either from *ab initio* quantum mechanical calculations or by fitting to experimental data (neutron, X-ray and electron diffraction, NMR, infrared, Raman and neutron spectroscopy) [80, 81]. For an empirical force field, the total energy of the system will be divided into as intramolecular energy, Van der Waals energy and Coulombic energy. Additionally, the intramolecular interactions composed of bond stretching interaction, angle bending interaction, dihedral interaction and improper torsions interaction, a generally expression as given in Eq. (3.9) adapted from the following literature [80].

$$U = \sum_{\text{bonds}} \frac{1}{2} k_b (r - r_0)^2 + \sum_{\text{angles}} \frac{1}{2} k_a (\theta - \theta_0)^2 + \sum_{\text{torsions}} \frac{V_n}{2} [1 + \cos(n\phi - \delta)] + \sum_{\text{improper}} V_{\text{imp}} + \sum_{\text{LJ}} 4\varepsilon_{ij} \left[\left(\frac{\sigma_{ij}}{r_{ij}} \right)^{12} - \left(\frac{\sigma_{ij}}{r_{ij}} \right)^{6} \right] + \sum_{\text{elec}} \frac{q_i q_j}{r_{ij}} \quad (3.9)$$

Moreover, to describe the coupling effect between stretching, bending, and torsion, other additional terms are addes, which could bring corrections to the intramolecular energy. For an instance of such cross-terms are given in Eqs. (3.10) and (3.11) [80].

$$U_{bond-bond} = \frac{1}{2}k_{bb}(r - r_0)(r' - r'_0) \tag{3.10}$$

$$U_{bond-bend} = \frac{1}{2}k_{ba}[(r - r_0) + (r' - r'_0)](\theta - \theta_0) \tag{3.11}$$

Generally, Hydrogen bonding interaction energy would be reproduced by van der Waals parameters and partial charges. Nevertheless, there is an extra term to improve the accuracy of its energy. A commonly used general expression is given in Eq. (3.12) [82].

$$U_{HB} = (\frac{A}{r_{AD}^{12}} - \frac{B}{r_{AD}^{10}})(\cos^2\theta_{AHD}) \tag{3.12}$$

Where r_{AD} and θ_{AHD} are the distance of donor-acceptor and the angle of the donor-hydrogen-acceptor, respectively.

A number of empirical potentials have been proposed, the most commonly used force fields are the Dreiding [83] and Universal (UFF) [84], CHARMM [85], AMBER [86], GROMOS [87], CVFF [88], and CLAYFF [89]. Due to the simplicity of calculating the intramolecular force of empirical force fields, simulations using empirical force field would be several orders of magnitude faster than these that used *ab initio* method. Consequently, it is possible to handle much larger systems and to explore much longer simulation times. In addition, it is possible to modify easily the energy expression to expect the calculation, to determine what the precise interactions are that corresponding to a specific property. Nevertheless, empirical force fields have some inherent limitations. Particularly, it cannot provide any information concerning the electronic structure, cannot do charge transfer and unable to break or to form the bonds during the simulation [80]. Furthermore, reactive force fields are developed to address out the intrinsic limits of the empirical force fields. A several of reactive potentials based on bond-order distance-dependent function have been proposed. The most common used reactive force fields are REBO2 [90], AIREBO [91] and REAXFF [92].

Chapter 4:

Wettability and work of adhesion of water-nanodroplet on (001) surface of cement paste

4.1. Introduction

This chapter is dedicated to investigate the surface properties of CSH from the point view of the atomic-scale level. To this end, the developed model of Pellenq et al. [24] has been used to describe the interatomic model of CSH. The Surface energy is estimated from a free boundary condition, which is a vacuum added onto the Z direction. In addition, the water adsorption onto CSH surface has been studied as well as the wettability of (001) surface of CSH evaluated from the contact angle between water-nanodroplet and CSH surface. Moreover, the work of adhesion between water-nanodroplet and CSH surface is deduced from the equilibrated state of water-nanodroplet onto the (001) surface of CSH.

4.2 Model construction and simulation details

4.2.1 Bulk and films CSH model

The developed realistic model of Pellenq et al. [24] has been used to represent the atomistic structure of CSH based on the initial structure of tobermorite 11 Å proposed by Hamid [25]. In order to increase the initial Ca/Si ratio, some SiO_2 groups were randomly removed, giving a modified tobermorite structure with a new ratio of 1.64. Grand Canonical Monte Carlo method was used to perform the adsorption of water molecules into the structurally defected modified tobermorite. More details of constructing a realistic model could be found in the following literature [24, 27-29]. Nine labels were used to distinguish the atoms of CSH structure in this work. Ow and Hw are oxygen and hydrogen atoms, respectively, to form the water molecules inside CSH; Oh and H are oxygen and Hydrogen atoms belonging to the hydroxyl groups; Ob are the bonding oxygen atoms in the Silica chains and O are the non-bridging oxygen atoms in the Si/Ca layers. Ca and Cw are the interlayer and the intra-layer calcium inside of CSH structure, respectively. Finally, there is only one type of Si atoms. To study the surface area effect onto the free surface energy, three bulk simulations boxes were concstructed 2×2×1, 5×4×1 and 10×8×1 containing 2004, 10020 and 40080 atoms, respectively. To generate a (001) free surface, a vacuum of 40 Å is added to the CSH bulk onto both sides along the Z direction. The corresponding structure of bulk, films and unit cell are shown in Fig. 4.1, where the corresponding unit cell parameters: a = 13.084 Å, b = 18.090 Å, c = 23.840 Å, $\alpha = 88.967°$, $\beta = 92.807°$ and $\gamma = 88.569°$.

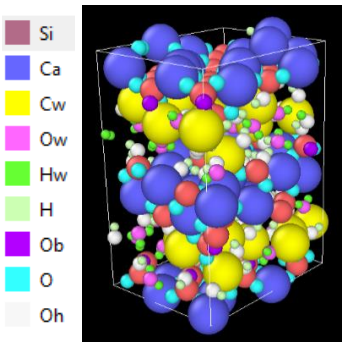

(a)

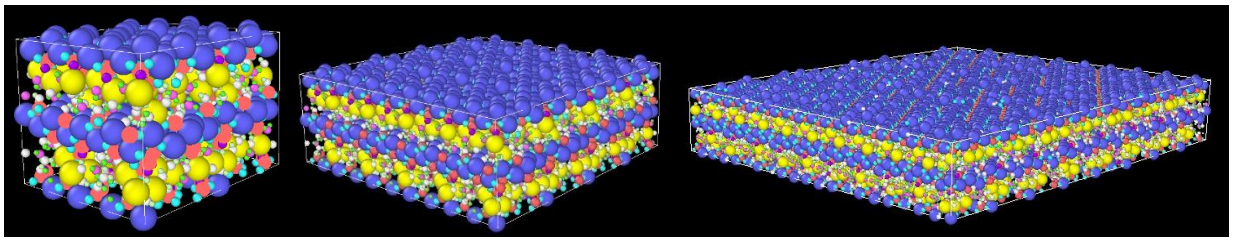

(b)

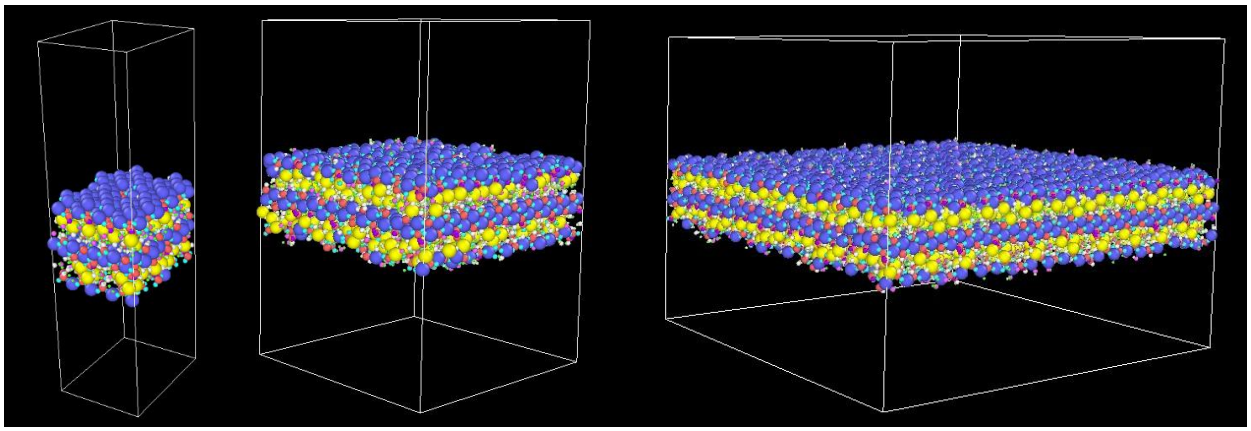

(c)

Fig. 4.1. Perspective view of bulk, films and unit cell structure (a). From left to right: bulk CSH, 2 × 2 × 1, 5 × 4 × 1 and 10 × 8 × 1 times of unit cell (b). CSH films corresponding to each CSH bulk (c).

4.2.2 Nanodroplet and CSH-nanodroplet model

An initial water box contained 500 water molecules obtained using Packmol code developed by Martínez et al. [93] and Atomsk code developed by Hirel [94]. Next, we simply added approximately 30 Å vacuum along X, Y and Z in order to create a free boundary condition to

generate a water nanodroplet. Jorgensen et al. [95] have investigated the simple point charge (SPC) model, which has the good capacity to give reasonable structural and thermodynamics descriptions of liquid water. A developed full flexible fixed-point charges model (SPC/E) has been used to generate the water-nanodroplet [96]. The initial bulk water as well as water nanodroplet are presented in Fig. 4.2.

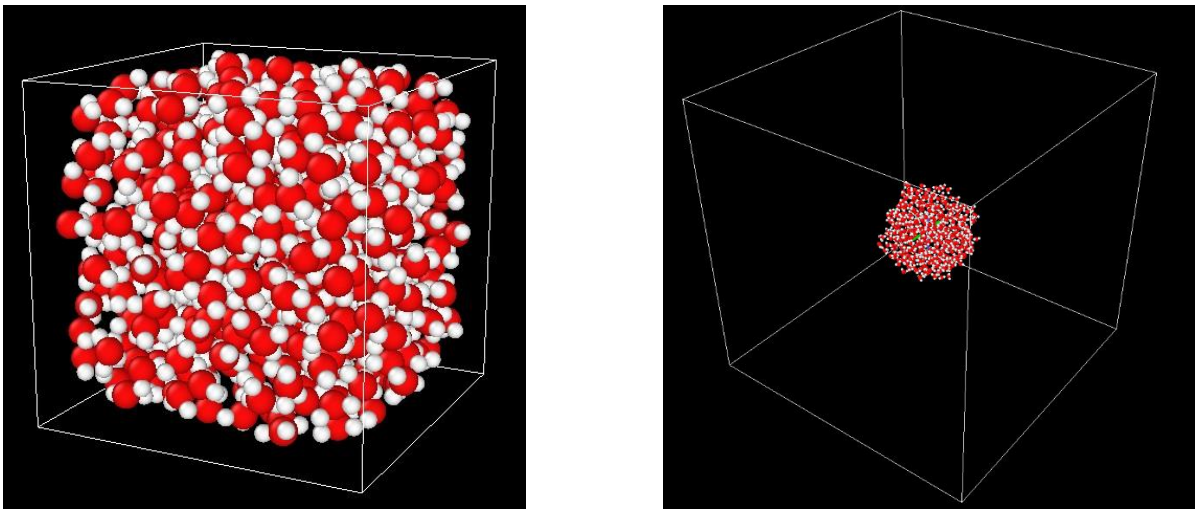

(a) (b)

Fig. 4.2. Perspective view of water molecules. The red and white atoms are Oxygen and Hydrogen, respectively. The initial positions of water box: Initial bulk water parameters: a = 18.445 Å, b = 18.265 Å, c = 18.250 Å, α = 90.00°, β = 90.00°and γ = 90.00°. The relaxed positions of water molecules (a). Water Nanodroplet parameters: a = 99.753 Å, b = 99.753 Å, c = 99.753 Å, α = 90.0°, β = 90.0° and γ = 90.0°(b). (For interpretation of the references to color in this figure legend, the reader is referred to the web version of this article.)

To create the CSH-Nanodroplet model containing 41580 atoms, we simply put water nanodroplet onto the relaxed (001) supercell surface structure (10×8×1). The distance between both is very close but not connected (3.04 Å). In CSH-Nanodroplet model there are 11 labels to recognize the atoms inside the structure. Besides the 9 labels as introduced in bulk CSH model, the rest of Od and Hd are oxygen and hydrogen atoms of water-nanodroplet, respectively. The CSH-Nanodroplet model is shown in the Fig. 4.3.

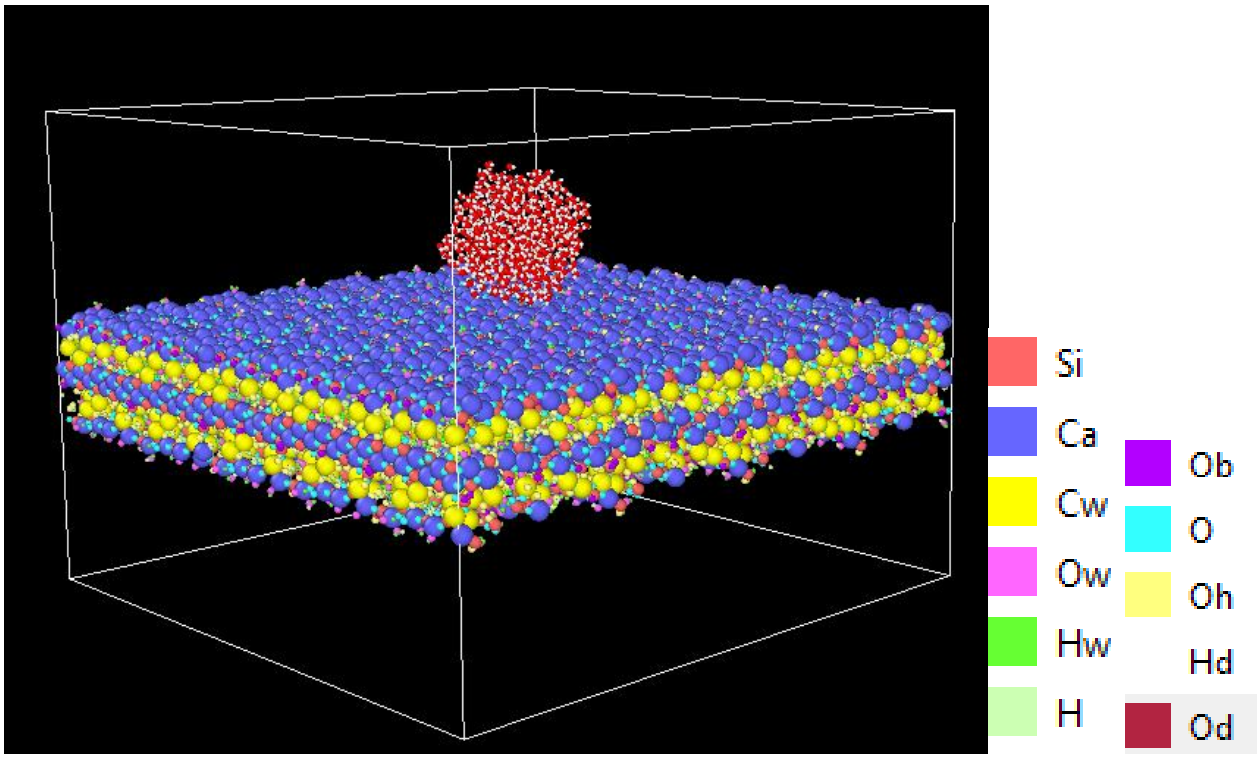

Fig. 4.3. CSH-Nanodroplet structure, cell parameters: a = 130.757 Å, b = 144.638 Å, c = 103.780 Å, α = 88.96°, β = 92.81° and γ = 88.57°.

4.2.3 Force field

Reactive force field [97, 98] (ReaxFF) is an empirical force filed based on distance-dependent bond-order functions to divide the system energy into a series of partial energy contributions as given in Eq. (4.1). Manzano et al. [31] have parameterized the Ca-O/H interactions within ReaxFF potential that has been employed to describe the interactions between the CSH atoms. In addition, the charge equilibration method (Qeq) [99] formulated by Nakano [100] has been applied on those models in order to redistribute the charge that allows charge transfer between atoms and molecules[101].

$$E_{system} = E_{bond} + E_{over} + E_{under} + E_{val} + E_{pen} + E_{tors} + E_{conj} + E_{vdw} + E_{Coulomb} \quad (4.1)$$

Where $E_{bond}$is bond order and bond energy, E_{over} and E_{under} are over-coordination and under-coordination energy, $E_{val}$is valence angle energy, E_{pen} is penalty energy, E_{tors} is torsion energy, E_{conj} is conjugation energy, E_{vdw} is van der Waals energy, $E_{Coulomb}$ is Coulomb energy.

Otherwise, SPC/E potential has been initially used to describe the interactions between oxygen and hydrogen atoms of water box. The total energy is divided into two part: one is non-bonded intermolecular interactions as described by Lennard-Jones (L-J) potential and Coulombic interactions of partial charges. The other part is harmonic bond and angle intramolecular interactions, as given in Eq. (4.2). Potential parameters of the geometry and electrostatic quantities of SPC/E are listed in the Table 4.1.

$$E_{total} = 4\varepsilon_{ij}\left[\left(\frac{\sigma_{ij}}{r_{ij}}\right)^{12} - \left(\frac{\sigma_{ij}}{r_{ij}}\right)^{6}\right] + \frac{q_i q_j}{4\pi\varepsilon_0 r_{ij}} + K_r(r - r_0)^2 + K_\theta(\theta - \theta_0)^2 \quad (4.2)$$

Where q_i and q_j are charges of atom i and atom j, respectively. r_{ij} is the distance between atom i and j, σ_{ij} and ε_{ij} are L-J parameters deduced from Lorentz-Berthelot rules [102] as shown in Eqs. (4.3) and (4.4); ε_0 is dielectric permittivity. r and θ are bending harmonic bond and bending harmonic angle, respectively, r_0 and θ_0 are equilibrated harmonic bond length and angle, respectively. Note that the usual factor ½ is included in force constants K.

$$\sigma_{ij} = \frac{\sigma_i + \sigma_j}{2} \quad (4.3)$$

$$\varepsilon_{ij} = \sqrt{\varepsilon_i \varepsilon_j} \quad (4.4)$$

Table 4.1

Parameters of SPC/E water model.

ε_{O-O}(Kcal/mol)	0.1502629	ε_{H-H}(Kcal/mol)	0.00774378
ε_{O-H}(Kcal/mol)	0.034111637	σ_{O-H} (Å)	2.04845
σ_{O-O} (Å)	3.1169	σ_{H-H}(Å)	0.98
q_O (e)	-0.8476	q_H (e)	0.4238
R_{OH}(Å)	0.9611	θ_{HOH}(°)	109.4712
K_θ(Kcal/(mol θ^2))	42.1845	K_r(Kcal/(mol Å^2))	176.864

4.2.4 Simulations details

Large-scale Atomic/Molecular Massively Parallel Simulator(LAMMPS) [103] has been used for molecular dynamics simulations. The method that added vacuum onto desirable direction for determining the surface energy has been employed by previous researchers [104-106]. In this work, details of creating a free surface are mentioned in the model construction part. To run molecular dynamics simulations, we used the Verlet algorithm for the integration of the equation of motion with a timestep of 0.25 fs. The bulk and films structures were relaxed in canonical(NVT) ensemble [107] using Nose-Hoover thermostat at T=300 K for 1.25 ns and 4 ns, respectively. To generate the nanodroplet, the water box was relaxed for 0.5ns under the same environment conditions, as described above in the bulk CSH simulation. The cutoff radius was set as 10 Å to simulate the non-boning interactions. Regarding the wettability of CSH surface, simulations of the nanostructure nanodroplet/CSH surface are run for 0.3 ns.

4.3. Results and discussion

4.3.1. Structural and mechanical properties

4.3.1.1. Radial distribution function

Radial distribution function (RDF), also called g(r), is defined as the probability of finding an atom at a distance r from another atom chosen as reference. In this session only the RDF of 2×2×1 supercell is discussed. First of all, a total RDF has been computed between all atom types for both of bulk and films CSH model. Fig. 4.4.a shows four remarkable peaks at around 0.95 Å, 1.65 Å, 2.25 Å, and 2.65 Å for both of bulk and films structure, what means that the relative positions of atoms in films structure are the same as bulk one. It can be seen that the first and second peaks situated around 0.95 Å and 1.65 Å, respectively are high and sharp compared with the remaining two peaks. To study the origin of those peaks, the contributions of partial pair interactions to total RDF is calculated as shown in Fig. 4.4.b. For both bulk and films structures it can be seen that the contribution to the first peak, which is situated around 0.95 Å, is mainly due to the hydroxyl groups from water and freely hydroxyl groups inside CSH. Si-Ob pair interaction mainly results from the second peak that is situated around 1.65 Å. For the third and last peaks they are situated around 2.25 Å and 2.65 Å, respectively, mainly due to the Ca-O and Ca-Si pair interactions, respectively. To have more understanding of the origin of those four peaks, we have investigated more pair interactions as well as the calculation of the coordination number in each pair of the four peaks.

Fig. 4.5 shows the main pair interactions results regarding the first three remarkable peaks observed in Fig. 4.4.a. It can be seen from Fig. 4.5.a that the first bond length of Ow-Hw and Oh-H pair interactions are 0.95 Å for both bulk and films structure that mainly contribute to the first remarkable peak. However, the coordination number of Ow-Hw is 1.81 within a range of sphere radius between 1.06 Å and 1.4Å for bulk structure and it is 1.52 within a range of sphere radius from 1.05 Å to 1.55 Å for films structure. The coordination number of Oh-H pair is 0.98 within a range of sphere radius from 1.13 Å to 1.45Å for bulk structure and it is 0.86 within a range of sphere radius between 1.06 Å and 1.47 Å for films structure. From Fig. 4.5.b it can be seen, for instance, that the first bond length of Si-Ob, Si-O and Si-Oh pair interactions are 1.65 Å for both of bulk and films structure, which results in the second remarkable peak. The coordination number of Si-Ob is 1.1 within a range of sphere radius from 1.72 Å to 3.4Å for bulk structure and it is 1.1 within a range of sphere radius between 1.81Å and 3.33 Å for films structure. The coordination number of Si-O pair is 2.2 within a range of sphere radius from 1.9 Å to 3.1Å for bulk structure and it is 2.15 within a range of sphere radius between 1.73 Å and 3.09 Å for films structure. Moreover, the coordination number of Si-Oh pair is 0.7 within a range of sphere radius from 1.73 Å to 3.02Å for bulk structure and it is 0.7 within a range of sphere radius between 1.73 Å and 3.05 Å for films structure. We studied the two types of calcium atom in the CSH model in order to understand more origins of the third remarkable peak. From Fig. 4.5.c it can be seen that the first bond length of Ca-Ow pair interaction is 2.75 Å and 2.70 Å for bulk and films structures, respectively. The coordination number of Ca-Ow is 0.3 within a range of sphere radius from 2.94 Å to 3.39 Å for bulk structure and it is 0.49 within a range of sphere radius between 3.34 Å and 3.52 Å for films structure.

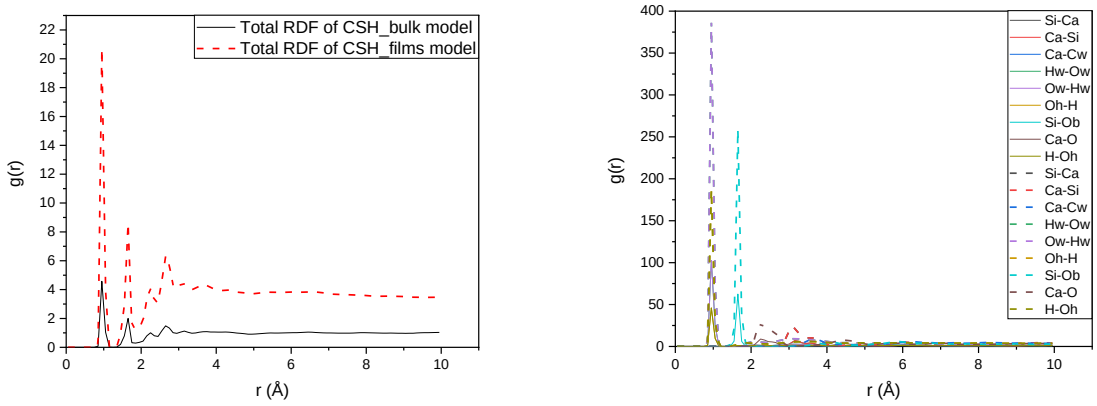

(a) (b)

Fig. 4.4. Total RDF of bulk (solid line) and films structure (dash line) (a), The contribution of pair interactions to total RDF of bulk (solid line) and surface structure (dash line) (b).

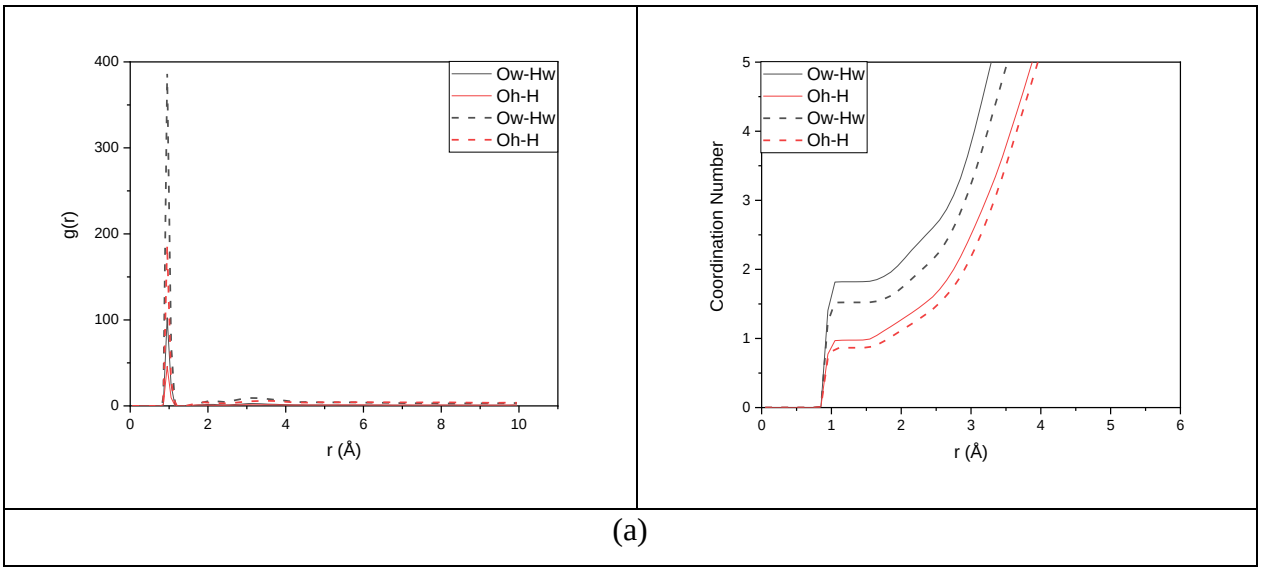

(a)

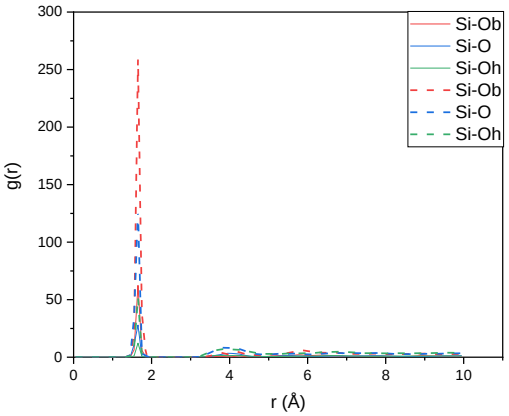
g(r)
r (Å)
Si-Ob
Si-O
Si-Oh
Si-Ob
Si-O
Si-Oh

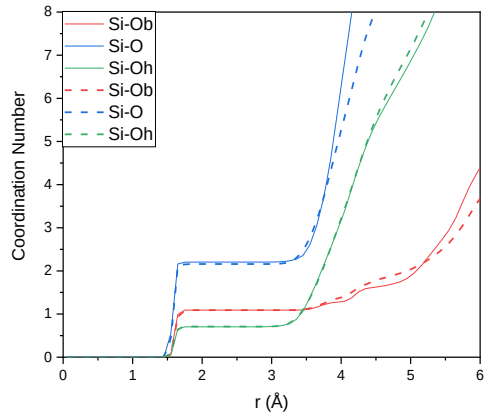
Coordination Number
r (Å)
Si-Ob
Si-O
Si-Oh
Si-Ob
Si-O
Si-Oh

(b)

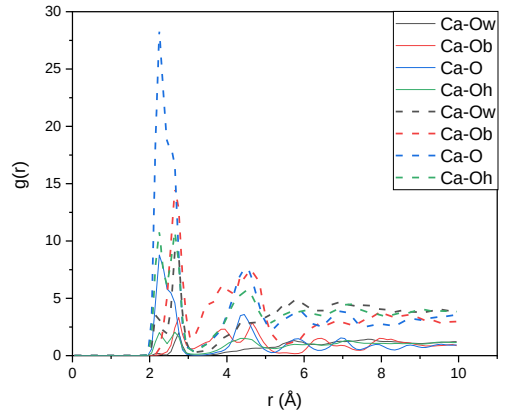
g(r)
r (Å)
Ca-Ow
Ca-Ob
Ca-O
Ca-Oh
Ca-Ow
Ca-Ob
Ca-O
Ca-Oh

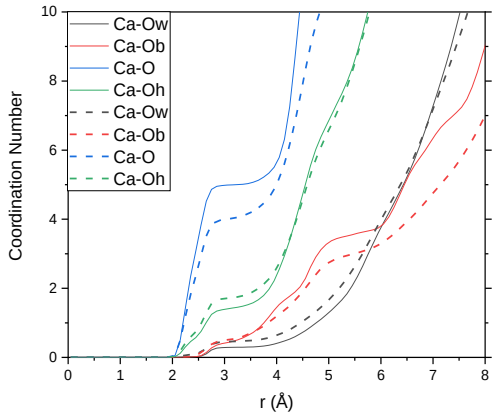
Coordination Number
r (Å)
Ca-Ow
Ca-Ob
Ca-O
Ca-Oh
Ca-Ow
Ca-Ob
Ca-O
Ca-Oh

(c)

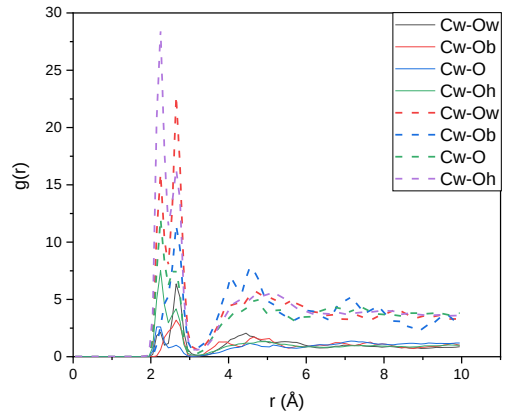
g(r)
r (Å)
Cw-Ow
Cw-Ob
Cw-O
Cw-Oh
Cw-Ow
Cw-Ob
Cw-O
Cw-Oh

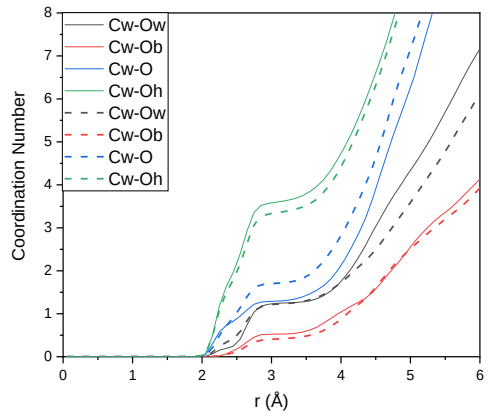
Coordination Number
r (Å)
Cw-Ow
Cw-Ob
Cw-O
Cw-Oh
Cw-Ow
Cw-Ob
Cw-O
Cw-Oh

(d)

Fig. 4.5. Partial distribution function and coordination number for bulk (solid line) and surface structure (dash line).

To investigate the last remarkable peak observed in Fig.4.4.a, the partial correlation function of RDF is shown in Fig. 4.6. The remarkable peak of Fig. 4.6 is represented in Fig. 4.7 as well as the coordination number corresponding to each of significant peak. From Fig. 4.7 it can be seen that Ob-Ob pair interaction is one of the contributions that results in the last remarkable peak observed in Fig. 4.4.a. For instance, its first bond length is 2.65 Å for both bulk and films structures, however, the coordination number of Ob-Ob is 0.92 within a range of sphere radius between 2.98 Å and 4.5 Å for bulk structure and it is 0.92 within a range of sphere radius from 3.31 Å to 3.79 Å for films structure. All results of the first bond length and coordination number of each pair interaction compared with other calculation [29, 108, 109] are listed in Table 4.2. The estimated error is in the range of 0.27 % to 11.64 %.

Table 4.2

First bond length and coordination number (CdN) of pair interactions compared with other experimental and theoretical data [29, 108, 109].

	This work				Experiments		Theoretical	
	CSH bulk		CSH surface		CSH bulk			
	Bond (Å)	CdN (range(Å))	Bond(Å)	CdN (range(Å))	Bond(Å)	CdN	Bond(Å)	CdN (range(Å))
Ow-Hw	0.95	1.81(1.06-1.4)	0.95	1.52(1.05-1.55)			0.99	1.81(1.3)
Oh-H	0.95	0.98(1.13-1.45)	0.95	0.86(1.06-1.47)			0.99	0.97(1.3)
Si-Ob	1.65	1.1(1.72-3.4)	1.65	1.1(1.81-3.33)				
Si-O	1.65	2.2(1.9-3.1)	1.65	2.15(1.73-3.09)	1.67	3.90	1.62	0.7-2.21(2.5)
Si-Oh	1.65	0.7(1.73-3.02)	1.65	0.7(1.73-3.05)				
Ca-Ow	2.75	0.3(2.94-3.39)	2.70	0.49(3.34-3.52)				
Ca-Ob	2.75	0.4(3-3.05)	2.65	0.5(2.95-3.02)				
Ca-Oh	2.25	1.4(3-3.08)	2.25	1.71(3.01-3.12)				
Ca-O	2.25	5(3.05-3.22)	2.25	4.02(3.08-3.15)	2.43	6.10	2.23/2.6	1.33-5(3)
Cw-Ow	2.65	1.25(3.05-3.15)	2.65	1.22(3.08-3.19)				
Cw-Ob	2.65	0.51(2.91-3.24)	2.65	0.54(3.02-3.19)				
Cw-O	2.20	1.29(2.95-3.13)	2.25	1.71(3.04-3.16)				
Cw-Oh	2.25	3.61(3.08-3.14)	2.25	3.38(3.08-3.14)				
Si-Si	3.15	1.19(3.29-3.88)	3.15	1.2(3.32-3.91)	3.15			
Ca-Ca	3.75	5.92(4.69-4.79)	3.76	4.79(4.71-4.73)	3.75			
Hw-Hw	1.55	0.84(1.66-1.69)	1.55	0.6(1.66-1.71)			1.51	0.98(1.6)
Ob-Ob	2.65	0.92(2.98-4.5)	2.65	0.92(3.31-3.79)	2.75		2.65	0.92(3)

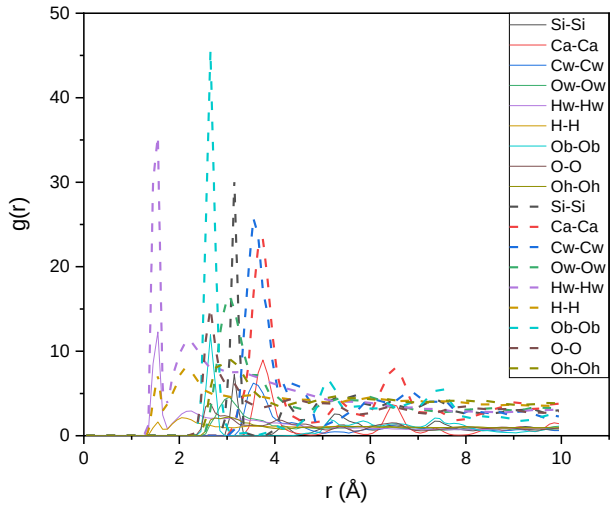

Fig. 4.6. Partial correlation function of bulk (solid line) and (001) surface structure (dash line).

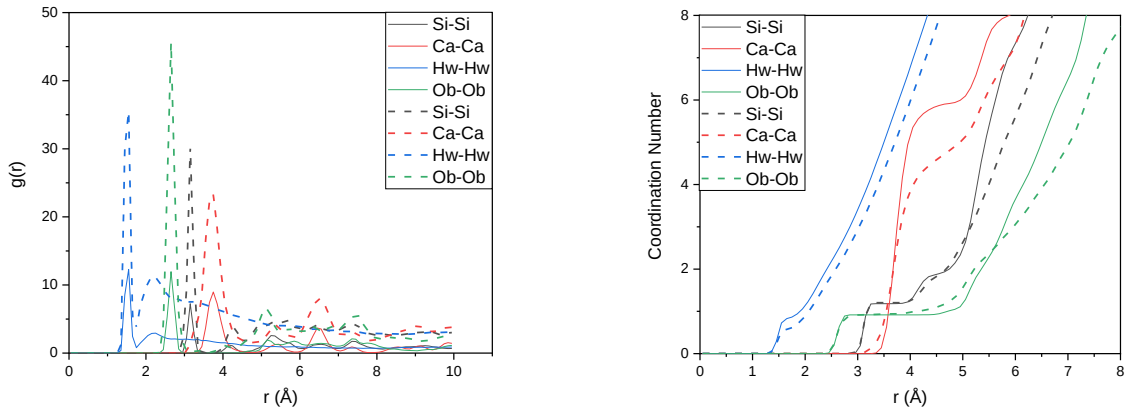

(a) (b)

Fig. 4.7. Partial correlation function and coordination number of bulk (solid line) and (001) surface structure (dash line).

4.3.1.2. Elastic properties and Ca/Si ratio effect

To study the Ca/Si ratio effect on CSH structure, the relaxed 10×8×1 bulk structure is used to investigate the mechanical properties of CSH. The equilibrated structure under uniaxial strain (X, Y and Z) and shear strain (YZ, XZ and XY) were applied with an engineering strain rate of 7×10^{9} s^{-1} in NVT ensemble. The elastic tensor is derived from stress strain relationship. We only present the most important elastic tensor and the corresponding results as shown in Table 4.3. It can be

seen that both C_{11} and C_{22} are bigger than C_{33}, which means the CSH structure is more resistant in XY plane corresponding to the silicate layers. Zaoui's [110] work shows that the elastic tensor is bigger if CSH has a bigger Ca/Si ratio. The same tendency is found between the present work and Pellenq's work [24]. Even though the Ca/Si of this work is bigger than Zaoui's work, most of elastic tensor data of this work remain smaller.

Bulk modulus (K), shear modulus (G), Young's modulus (E), Poisson's ratio (ν) and indentation modulus (M) are estimated according to the following equations:

$$K_V = [\, C_{11} + C_{22} + C_{33} + 2(C_{12} + C_{23} + C_{31})]/9$$
$$G_V = [\, C_{11} + C_{22} + C_{33} - (C_{12} + C_{23} + C_{31}) + 3(C_{44} + C_{55} + C_{66})]/15$$
$$E = 1/[(1/3G) + (1/9K)] \quad (4.5)$$
$$\nu = 0.5[1-3G/(3K + G)]$$
$$M = 4G[(3K + G)/(3K + 4G)]$$

The corresponding results are shown in Table 4.4. It can be seen that our findings are very close to other theoretical works. Moreover Constantinides et al. [111] found the indentation modulus equal to 65 GPa from nanoindentation measurements, which is in agreement with our obtained value of 61.29 GPa.

Table 4.3

Elastic constants of CSH model compared with other works [24, 110]

	Pellenq's work	Zaoui's work		This work
Ca/Si Ratio	1.65	1.00	0.83	1.64
Density(g/cm^3)	2.56	/	/	2.37
C11(Gpa)	93.50	180.01	153.90	82.85
C22(Gpa)	94.90	117.29	103.83	92.00
C33(Gpa)	68.50	157.22	119.61	65.27
C44(Gpa)	19.20	29.48	22.26	16.91
C55(Gpa)	16.10	45.62	35.36	14.60
C66(Gpa)	31.20	36.77	32.46	25.04
C12(Gpa)	45.40	48.93	37.23	43.35
C13(Gpa)	26.10	53.97	38.91	20.85
C23(Gpa)	30.01	29.60	14.46	22.69

Table 4.4

Results of Bulk modulus, shear modulus, Young's modulus, poisson's ratio and indentation modulus compared with others [24, 28, 108].

	This work	Other works
K(Gpa)	45.99	47-51
G(Gpa)	21.53	22-24.7
E(Gpa)	55.86	55-74
M(Gpa)	61.29	63.72-69
v	0.3	0.28-0.3

4.3.2 Surface properties

4.3.2.1 Surface free energy

The (001) surface free energy of CSH is determined by using the following equation:

$$\gamma_s = \frac{E_{films} - E_{bulk}}{A} \tag{4.6}$$

Where the γ_S is the surface free energy, E_{films} is the total energy of CSH films, E_{bulk} is the total bulk energy, A is the area of the surface. In this work, A is the area of up and down surface of the films structure.

To evaluate the surface free energy, we prepared three different sizes of surface. Firstly, we must ensure that both bulk and films have got well relaxed. Fig. 4.8 shows the total energy versus time for the 2×2×1 bulk and films supercells relaxed for 1.2 ns and 4 ns, respectively. We can see that both structures are well relaxed, since the total energy is keeping fluctuating but around a constant value. The same case occurs for 5×4×1 and 10×8×1 supercells. The results of free energy concerning (001) surface is 698 erg/cm^2, 740 erg/cm^2 and 701 erg/cm^2 corresponding to 2×2×1, 5×4×1 and 10×8×1 models, compared with available experimental results as listed in Table 4.5.

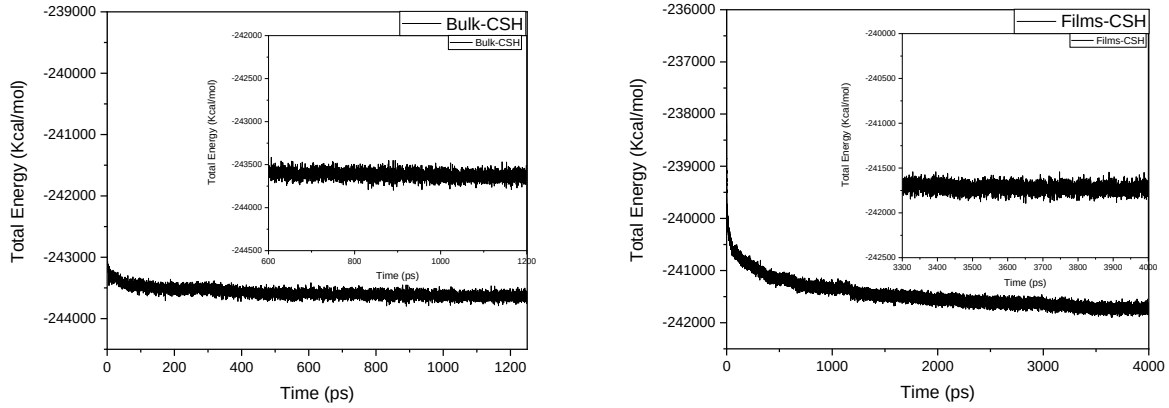

(a) (b)

Fig. 4.8. Total energy versus time for bulk structure (a), and (001) surface structure (b).

Table 4.5

Surface energy of CSH compared with other calculations.

Methods	Materials	Stoichiometry/Degree of hydration	Surface energy erg/cm^2
	Tobermorite	$Ca_3Si_2O_7 \cdot 2H_2O$	386-450
Experimental[11, 36, 37]	Cement paste	0.45 (water to cement ratio)	1370
	Cement paste	0.6 (water to cement ratio)	657
Theoretical	CSH (this work)	$41Ca(OH)_2 31CaO 44SiO_2 \cdot 34H_2O$	698-740

At the end of this part, we present the surface interaction energy calculation of water molecule in the bulk system to water molecule in the droplet estimated by the equation:

$$E_{surface\ interaction} = E_{droplet} - E_{bulk\ water} \quad (4.7)$$

Where the $E_{surface\ interaction}$ is the total interaction energy of the droplet surface, $E_{droplet}$ is the total energy of water-nanodaoplet, $E_{bulk\ water}$ is the total energy of bulk water. Fig. 4.9 shows the interaction energy of water molecules with CSH surface and the total energy of water-nanodroplet. It can be seen that the interaction energy between the nanodroplet and the surface converges quickly as the same as the total energy of water-naondroplet.

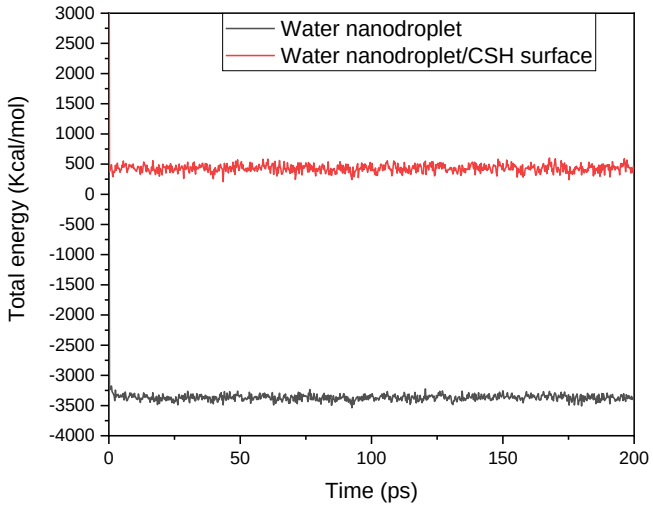

Fig. 4.9. Variation with time of the total energies of water-nanodroplet and water-nanodroplet/CSH surface.

4.3.2.2 Wettability

The wettability is measured by the contact angle between equilibrated nanodroplet and CSH surface. The schematic of droplet onto a surface is shown in Fig. 4.10. It is called non-tilting hydrophobic surface if the contact angle between droplet and surface is bigger than 90° (Fig. 4.10.a), otherwise, it is called non-tilting hydrophilic surface if it smaller than 90° (Fig. 4.10.b). Moreover, if the surface has a tilting angle, the smaller one angle is called as receding angle and the other one is called as advancing angle as shown in Fig. 4.10.c. This method was used previously on clay, KCl and geopolymers systems [112-114].

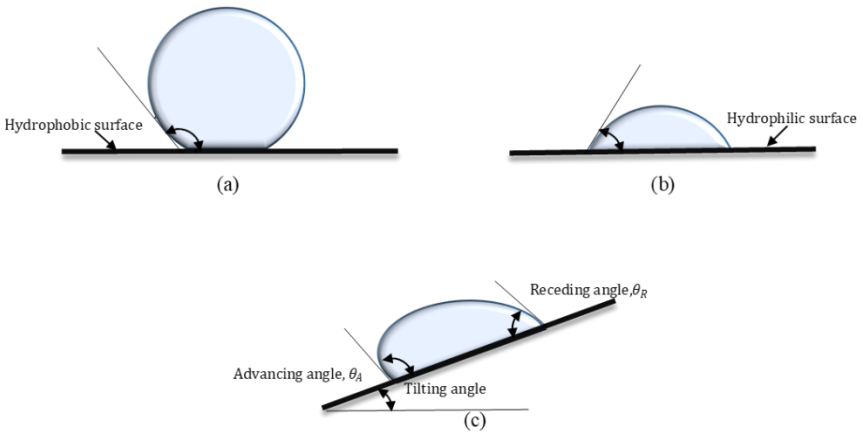

Fig. 4.10. Schematic of a droplet onto a non-tilting hydrophobic surface (a), non-tilting hydrophilic surface (b), and tilting surface (c).

In order to have the equilibrated stable configuration of nanodroplet onto CSH surface, we investigated the variation of total energy of CSH-Nanodroplet structure with time and the interaction energy between water-nanodroplet and CSH versus time are shown in Fig. 4.11. The interaction energy between water-nanodroplet and CSH is determined by Eq. (4.8).

$$E_{interaction} = (E_{CSH} + E_{droplet}) - E_{CSH+droplet} \quad (4.8)$$

Where the $E_{interaction}$ is the total interaction energy between water-nanodroplet and CSH, E_{CSH} is the total energy of CSH. $E_{droplet}$ is the total energy of water-nanodaoplet, $E_{CSH+droplet}$ is the total energy of CSH-Nanodroplet structure.

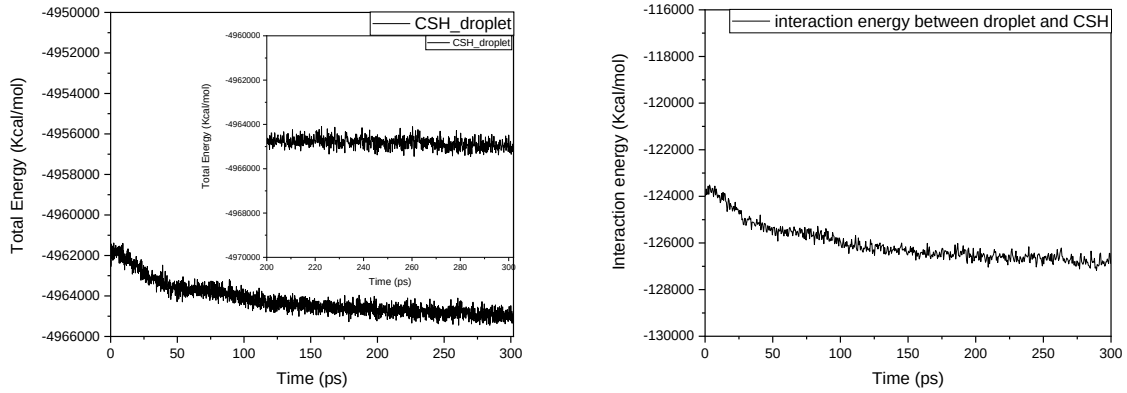

(a) (b)

Fig. 4.11. Total energy of CSH-Nanodroplet structure (a), and the interaction energy between water-nanodroplet and CSH versus time (b).

It can be seen that the interaction energy between water-nanodroplet and CSH has the same evolution in time as the total energy of CSH-Nanodroplet. The total energy is almost converged around 60ps and it would suddenly go down to be relaxed after 300 ps.

The contact angle is determined as follows: Every 5ps we generated a configuration of nanodroplet onto CSH surface and the average value of contact angle is determined from the last 50 ps data. To do so, firstly we extract the atomic positions for each configuration from last 50 ps data then plot in Cartesian coordinates. Next, we simply made an appropriate tangent to close the surface of equilibrated water droplet profile then to meet the CSH substrate.

The configuration, for instance, at 0 ns, 0.1 ns and 0.25 ns are shown in Fig. 4.12. We must admit that we present the main water molecules adsorbed onto CSH surface and deleted the few of water molecules that far away from the main water droplet. Fig. 4.12 shows that the droplet is adsorbed quickly onto CSH (001) surface and the spreading area is increasing in time. At 0.25 ns, it can be remarked that the spreading area of equilibrated nanodroplet onto CSH surface is a defect circle and a few of water molecules are far away from the main circle adsorbed onto the area. Closer to the edge of surface even one of them is adsorbed onto the edge of the surface.

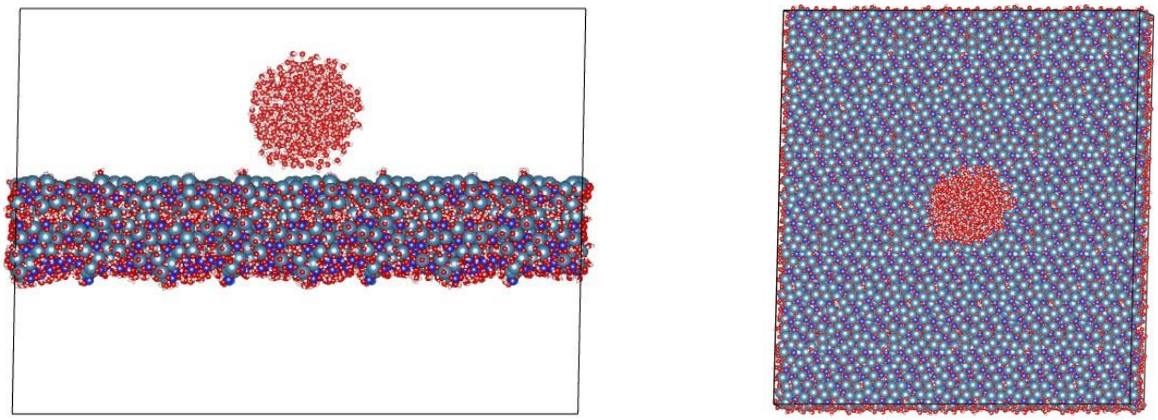

(a)

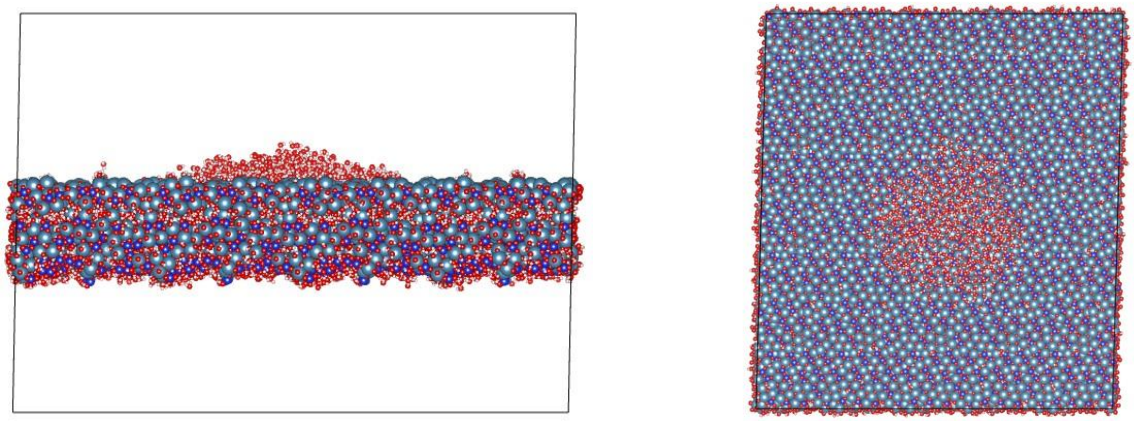

(b)

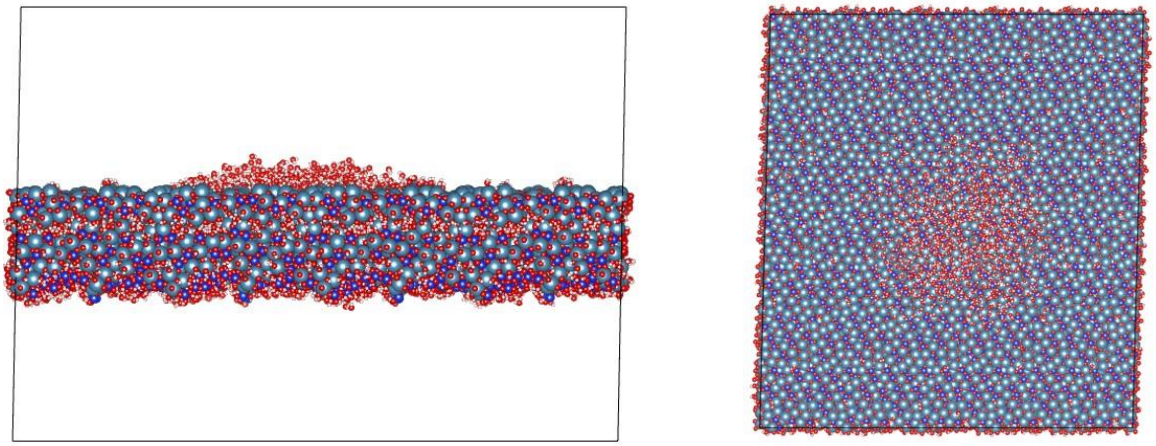

(c)

Fig. 4.12. Water-nanodroplet onto CSH surface at different stage: *t* = 0 ns (a), *t* = 0.1 ns (b), *t* = 0.25 ns (c).

In order to have more understanding of equilibrated CSH-Nanodroplet structure, the atomic density profile of water-nanodroplet along Z direction is calculated from the equilibrated state of CSH-Nanodroplet structure as shown in Fig. 4.13. It can be seen that the sharpest and highest peak is situated at around 3.2 Å. Moreover, the mean-squared displacement (MSD) of water-nanodroplet is estimated from the last 50 ps data of CSH-Nanodroplet structure as shown in Fig. 4.14. It can be found that MSD is decreasing in time. The diffusion coefficient is derived from MSD curve as following the three-dimensional Einstein relation function shown here:

$$D=\frac{1}{6}\frac{d}{dt}r(t)^2 \tag{4.9}$$

Where $r(t)^2$ is mean-squared displacement defined as r(t)=R(t)-R(0), R(t) is the atomic position at time t. Fig. 4.15 shows the diffusion coefficient of water-nanodroplet onto CSH surface. It can be seen that the diffusion coefficient is a little bit changing quickly at the beginning and it will slow down the changing at the last.

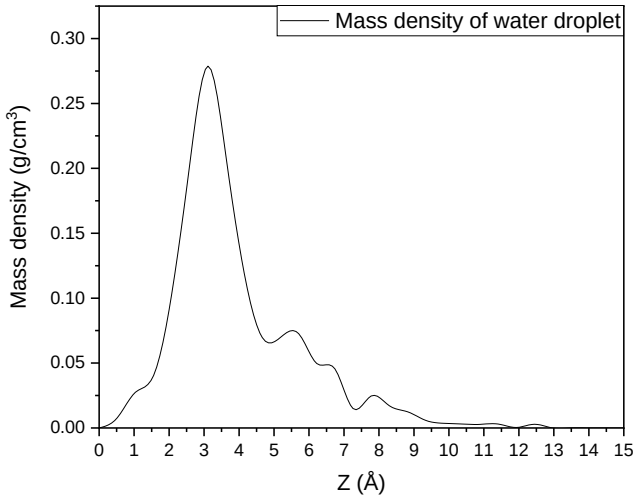

Fig. 4.13. Mass density of equilibrated water-nanodroplet onto CSH surface.

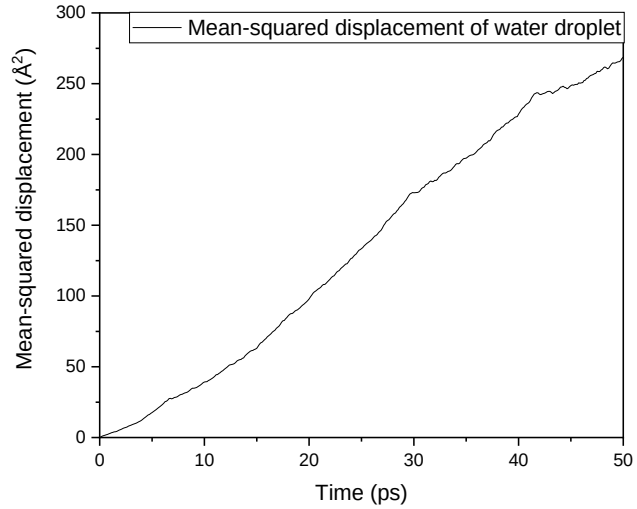

Fig. 4.14. Mean-squared displacement of equilibrated water-nanodroplet onto CSH surface versus time.

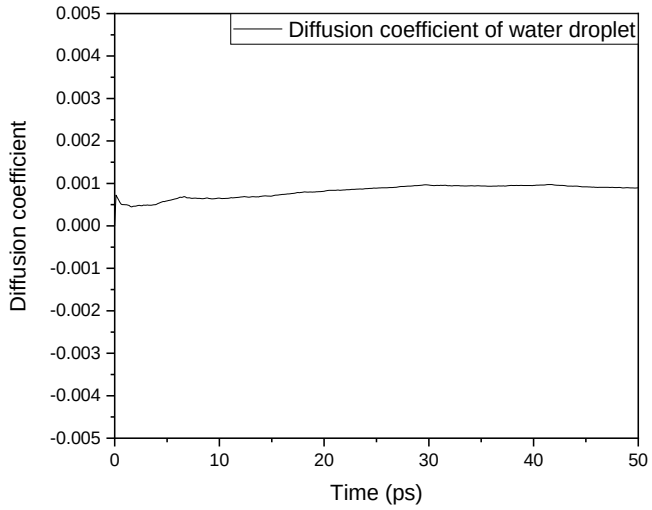

Fig. 4.15. Diffusion coefficient of equilibrated water-nanodroplet onto CSH surface versus time.

Moreover, we studied the distance between equilibrated structure of droplet and CSH surface by using radial distribution function as well as the coordination number as shown in Fig. 4.16. The last shows the sharpest and highest peak situated at 2.65 Å with a coordination number of 0.084 within a range of sphere radius from 3.04 Å to 3.19 Å for Ca-Od pair interaction. For Ca-Hd pair interaction the first bond length is 3.20 Å. In addition, we remark a small peak of Ca-Od pair interaction situated at 2.25 Å. To dig the origin of this small peak, we investigated the Od-Hd pair interaction as shown in Fig. 4.16.b that we can see the small peak appeared in Ca-Od pair interaction mainly due to the superposition of the Ca-Od and Od-Hd pair correlations. However, we remark that the coordination number of Od-Hd pair is 1.94 within a range of sphere radius from 1.13 Å to 1.51 Å.

The results of averaged contact angle calculated from last 50 ps data compared with available experiment results are presented in Table 4.6. As it can be seen, our results have a highly agreement with the available experimental results. Obviously, it can be demonstrated that the (001) surface of CSH is hydrophilic. Moreover, the difference between receding angle and advancing angle is bigger if the tilting angle is bigger too. The smallest and biggest contact angle is 23.62° and 29.29°, respectively. The water-nanodroplet adsorbed onto CSH surface from different views at 0.25 ns is shown in Fig. 4.17. One can see that the contact angle between water-nanodroplet and CSH is different with changing the views.

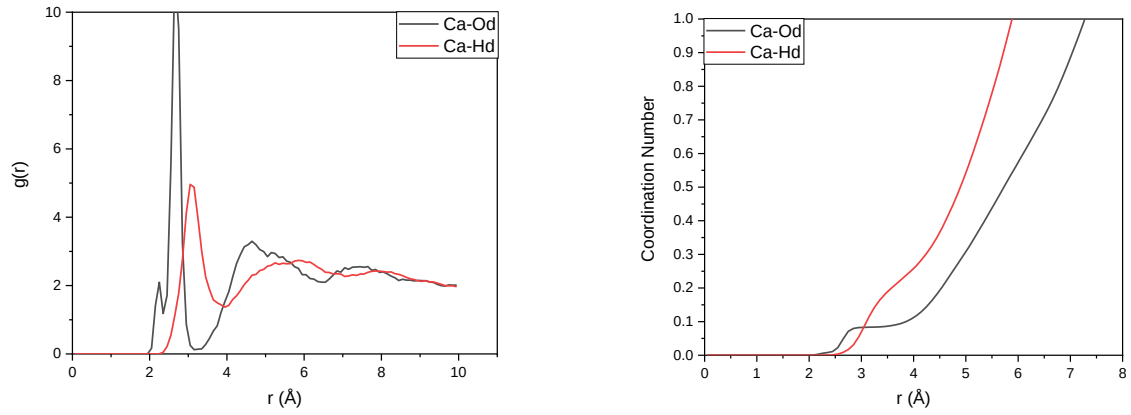

(a)

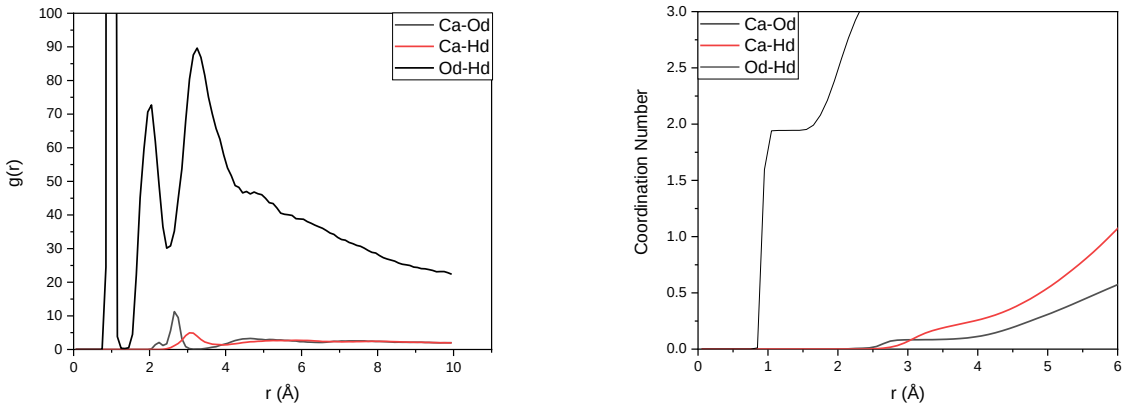

(b)

Fig. 4.16. Radial distribution function and coordination number of CSH-Nanodroplet structure.

Table 4.6

Contact angle between equilibrated water droplet and CSH surface compared with experiments.

Method	Contact angle(°)			
	Tilting surface angle (1.0333°)		Tilting surface angle (2.8069°)	
Theoretical (this work)	Receding angle	Advancing angle	Receding angle	Advancing angle
	23.62	26.41	26.32	29.29
Experimental[17-19]	21.7-36			

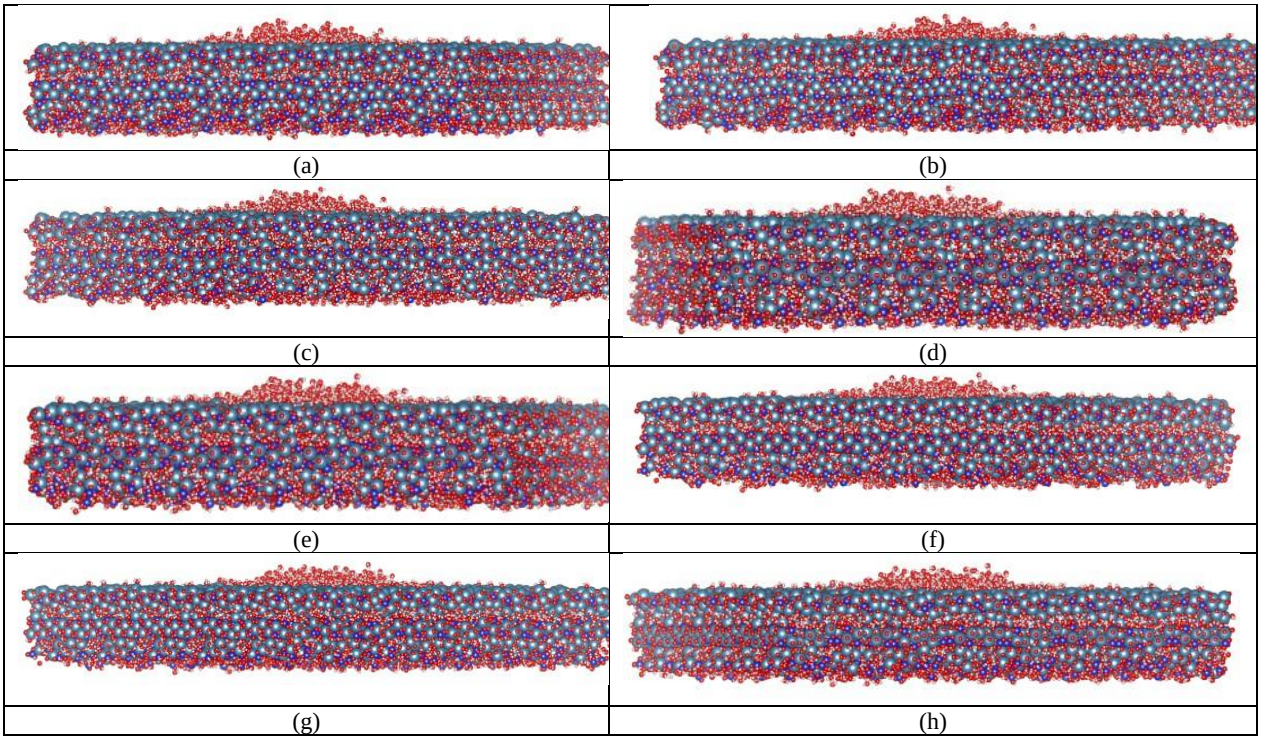

Fig. 4.17. Different views of water-nanodroplet onto CSH at 0.25 ns.

To digging more understanding of equilibrated structure of CSH-Nanodroplet. We have investigated the work of adhesion between water-nanodroplet and CSH. We have followed two methods. In the first one, we started from the contact angle between the solid and liquid phases, what means that the work of adhesion is taken as the work required to separate a droplet from a solid surface and leaving behind a clean solid surface. This is determined by following Young-Dupre equation [115] :

$$W_{AB}=\gamma_l(1+\cos\theta) \quad (4.10)$$

Where W_{AB} is the work of adhesion between solid A and liquid B, $\gamma_l$is the surface tension of liquid and θ is the contact angle between liquid and solid. We did again the averaged contact angle from different tilting surface, which gives the value of 26.41°. The surface tension of water from experiment [116] corresponds to 71.99×10^{-3} J/m^2. Then the work of adhesion is determined as 136.47×10^{-3} J/m^2, which is very close to the experimental results of Courard's [117] (102.49 ×10-

[3] J/m^2). In the second method, we studied the molecular surface effect onto work of adhesion between water-nanodoplet and CSH. In this way, the work required to break the interaction energy between solid and liquid and make a separation between them is considered as the work of adhesion. It is estimated according to Eq. (4.11):

$$W_{CSH+droplet} = \frac{E_{interaction}}{2A} \tag{4.11}$$

Where the $W_{CSH+droplet}$ is the work of adhesion between CSH and water-nanodroplet, $E_{interaction}$ is the interaction energy between CSH and water-nanodroplet, A is the molecular contact area. In this case three types of molecular surface are considered to determine the work of adhesion, which are Van der Waals(VDW) contact area, solvent accessible surface area and Connolly surface. The three types molecular surface of equilibrated water-nanodroplet created are shown in Fig. 4.18. The VDW contact area, in this work, is represented by simply draw the top view of the equilibrated water-nanodroplet onto CSH surface through using the van der waals radii [118] of all the constituent atoms composed of water-nanodroplet. However, the solvent accessible surface area is taken as the area of the system, which is accessible to solvent. It is represented by using a sphere of a radius is 1.4 Å to probe the surface. Moreover, the Connolly surface is represented as the same method as the one determining the solvent accessible area. For calculating the value of contact area, we calculated the pixels of water-nanodroplet and CSH. To do so, we replot the VDW contact area between water-nanodroplet and CSH surface as shown in Fig. 4.19 to determine the pixels of water-nanodroplet and CSH. The ratio of pixels between water-nanodroplet and CSH surface is firstly determined, so we could estimate the spreading area of water-nanodroplet. The obtained result of work of adhesion between water-nanodroplet and CSH gives 8.998 J/m^2 for Connolly surface. It is equal to 7.704 J/m^2 for solvent accessible area and equal to 10.76939 J/m^2 for VDW contact area. It can be seen that the results of work of adhesion calculated using connolly area is closer, rather than using solvent accessible contact area or VDW contact area.

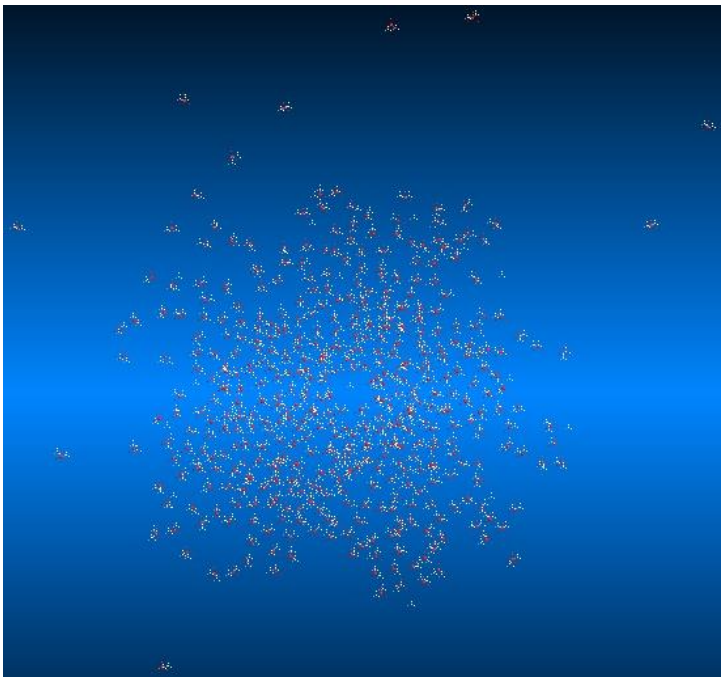

(a)

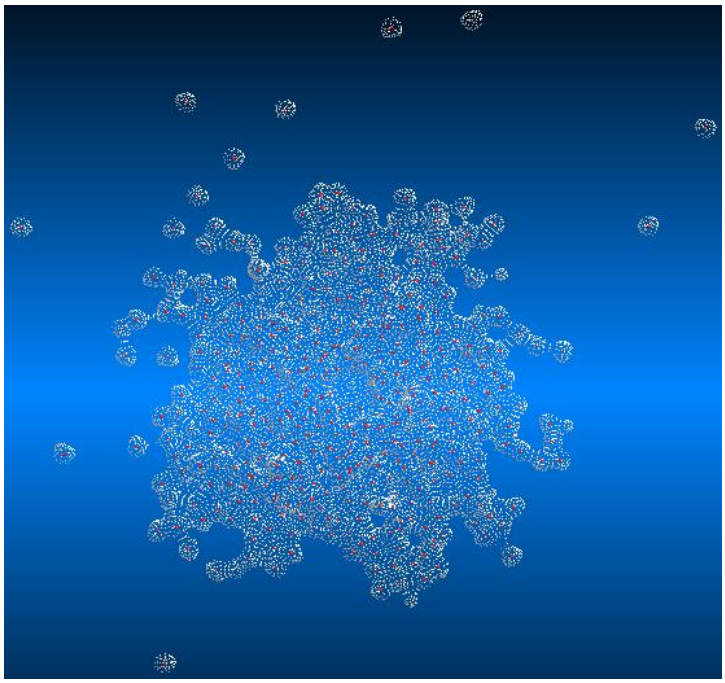

(b)

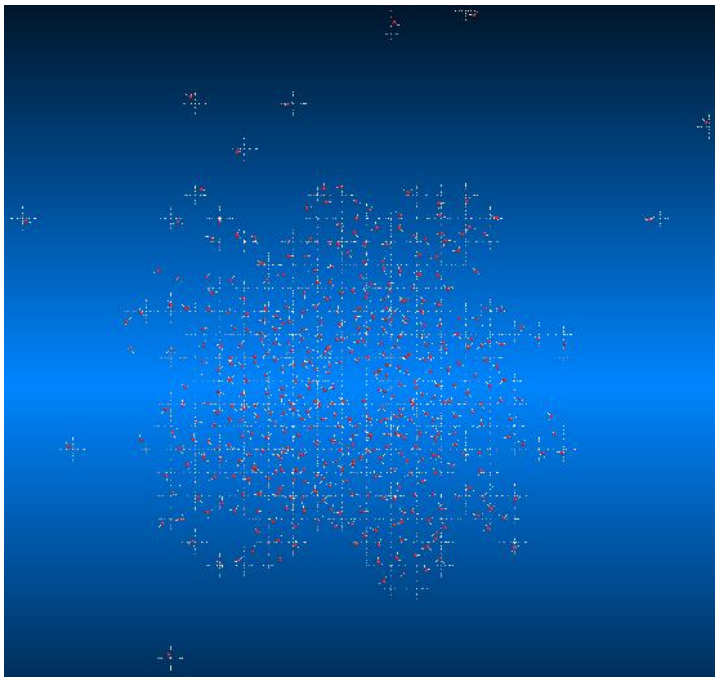

(c)

Fig. 4.18. Contact area (a) VDW (b) connolly surface (c) solvent accessible area of water-nanodroplet between CSH.

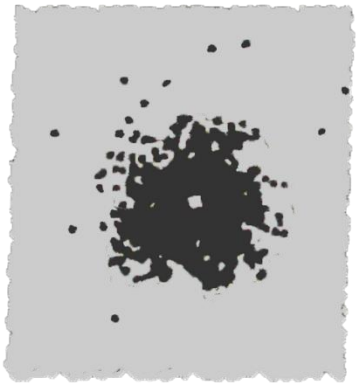

Fig. 4.19. VDW contact area (black color) of water-nanodroplet onto CSH.

4.4. Conclusion

In this work, the work of adhesion and the wettability between a water nanodroplet and CSH (001) surface have been investigated by means of Molecular Dynamics simulation. A realistic model has been employed to describe the nanoscale structure of CSH, and ReaxFF has been used to simulate the atomic interactions in CSH based model. The obtained surface energy of (001) CSH surface has been found between 698 erg/cm^2 to 740 erg/cm^2, in agreement with experimental findings. The averaged contact angle between equilibrated water-nanodroplet and CSH surface is found in the range of 23.62° to 29.29°, which confirms the hydrophilic behavior of (001) surface of CSH. The obtained work of adhesion between water-nanodroplet and CSH surface is 136.47×10^{-3} J/m^2 in agreement with the experimental data. For Connolly surface, solvent accessible area and VDW contact area, our calculations give the values of 8.991 J/m^2, 7.704 J/m^2 and 10.769 J/m^2, respectively.

Chapter 5:

Molecular-scale insight into improved waterproofing of cement paste by protective epoxy resins nano-coating

5.1. Introduction

The aim in the present chapter is to discuss the improvement of hydrophobicity behavior by coating CSH surface with epoxy resin film. It is a deep study necessary to analyze the interfacial bonding and the adhesion between epoxy resin layer, CSH and water. To this end, the developed realistic model of Pellenq et al. [24] has been used to describe the interatomic model in CSH nanostructure. 7 surface coating models are constructed by varying the concentration of epoxy material. It is the first time that a full coating is investigated with diglycidyl ether of bisphenol A (DGEBA) as epoxy monomer and m-phenylenediamine (MPD) as hardener. The hydrophobicity of coated (001) CSH surface is investigated from the contact angle between water nanodroplet and coated CSH surface. Dynamical properties including diffusion coefficient of water molecules is evaluated for the various proposed models to control the water penetration into the epoxy layer. Through this work, a particular attention will be paid to the interfacial bonding in order to explain the adhesion behavior of epoxy film on cement paste. The analysis of the interatomic bonding between CSH, epoxy layer atoms and water are evaluated through the radial distribution function, the coordination number and the mass density profile. In addition, the work of adhesion between epoxy resins and CSH is estimated from the interfacial model. This study offers an in-depth understanding of the nanoscale mechanisms of wettability of epoxy resin coated CSH and it provides information such as the structural changes for a better prevention of the durability of cementitious materials.

5.2. Model construction and simulation details

5.2.1. CSH surface coated model

The (001) CSH surface model containing 10,020 atoms is derived from the 5 × 4 × 1 bulk supercell of our previous work [17]. The developed CSH model is based on Pellenq et al. [24] with a new Ca/Si ratio of 1.64. More details of constructing a realistic CSH can be found in the following literature [24, 27, 29]. To simplify the accommodation of epoxy coating onto (001) CSH surface, we transformed the triclinic system of CSH to orthogonal system that it maintained the relative positions of atom inside CSH during the transformation. The surface model (a = 70.390 Å, b = 75.245 Å, c = 92.296 Å, $\alpha = \beta = \gamma = 90.00^{\circ}$) is obtained by adding 65 Å vacuum along Z direction onto the transformed 5 × 4 × 1 bulk CSH. The initial and equilibrated structures of surface model are shown in Fig. 5.1 as well as the variation of total energy of surface slab with time. To construct

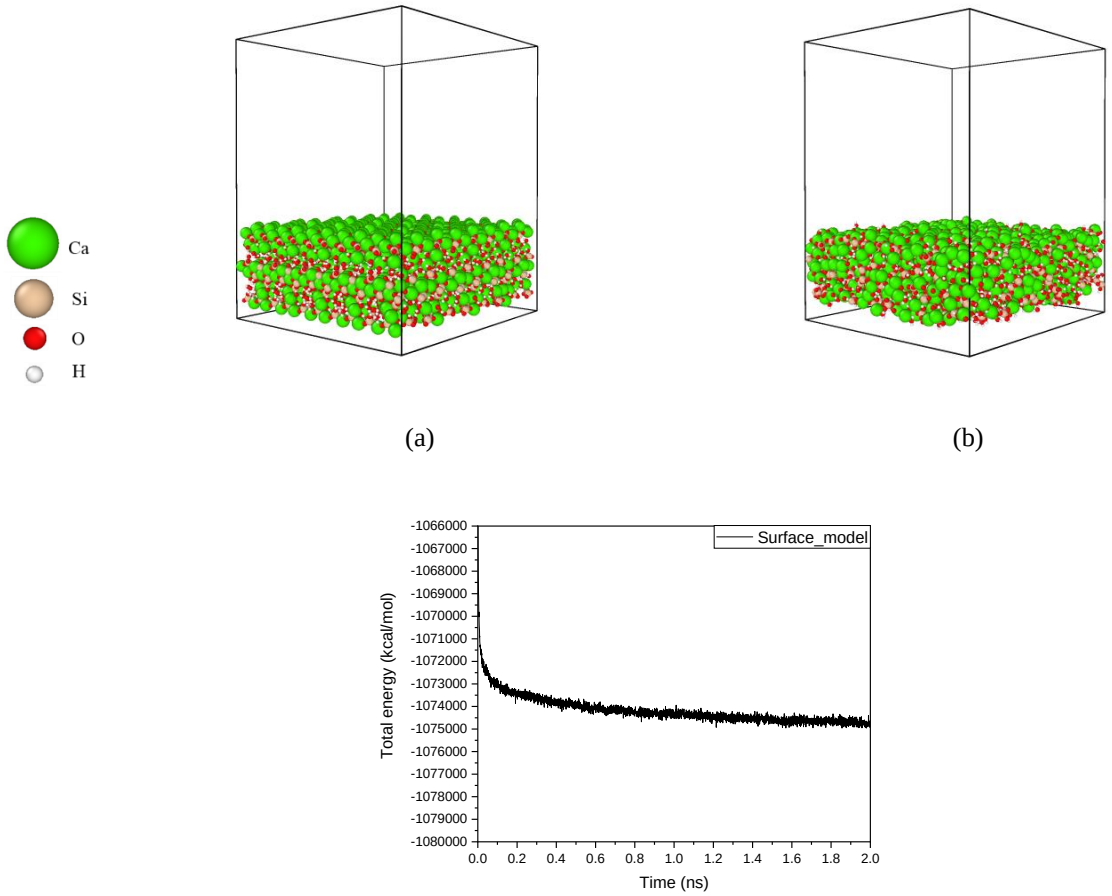

Fig. 5.1. Perspective view of (001) CSH surface model: initial structure (a), equilibrated structure (b), and the total energy versus time of surface model (c).

the (001) CSH surface coated model, a confined layer of amorphous cell composed of DGEBA and MPD is placed onto the relaxed (001) surface model. We calculated the appropriate distance between coating and CSH surface for which the coated surface structure has the minimum energy at the appropriate distance. In this work, we have constructed 7 surface coating models by varying the concentration of epoxy material. Moreover, we keep the number ratio of DGEBA/MPD as 2:1. The bulk epoxy coated CSH is constructed by eliminating the vacuum onto Z direction of the equilibrated CSH surface coated model. For instance, one of the initial coated surface structures containing 15,150 atoms with 15.62 wt% of epoxy monomers and 2.48 wt% of MPD is presented in Fig. 5.2 as well as the variation of total energy with the distance between coating and CSH. In this case, the most appropriate equilibrium distance is 0.874 Å. In addition, the equilibrated CSH

surface coated structure corresponding to the first one, as listed in Table 5.2, is shown in Fig. 5.3 as well as the derived relaxed bulk epoxy coated CSH. The variation of total energy with time of the both structures are displayed in Fig. 5.3 as well.

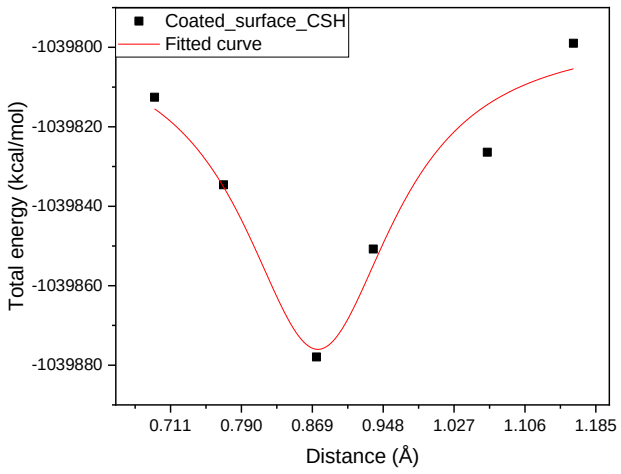

(a)

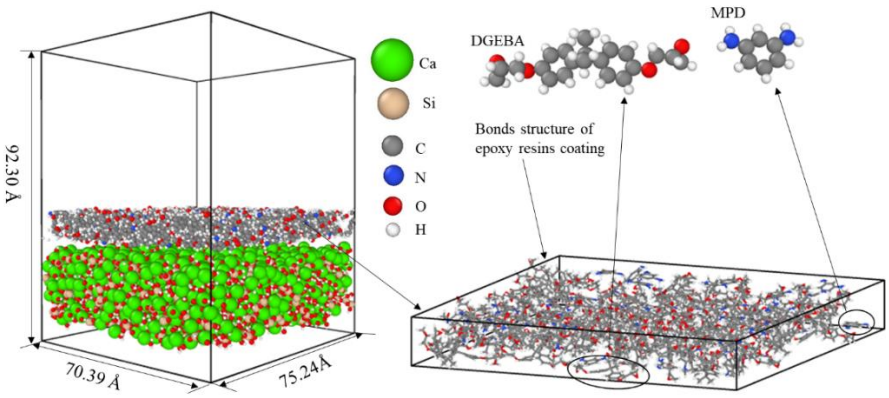

(b)

Fig. 5.2. Total energy of the coated CSH versus distance between coating and CSH surface (a). The initial configuration of (001) CSH surface coated (orthogonal) (b).

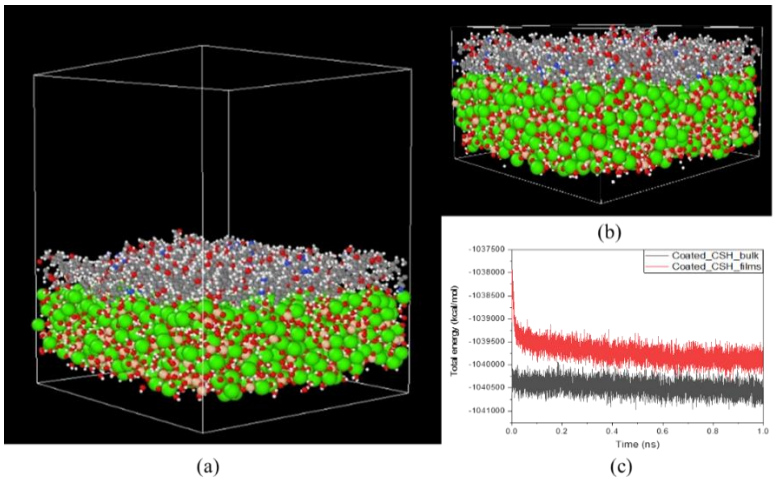

Fig. 5.3. Perspective view of equilibrated configuration of (001) CSH coated surface (a). The relaxed bulk epoxy CSH coated (b), and the total energy versus time of both models (c).

5.2.2. Interfacial model

To construct the interfacial model, we built epoxy resins films (a = 69.926 Å, b = 74.800 Å, c = 101.882 Å, $\alpha = \beta = \gamma = 90.00^{\circ}$) with a ratio of DGEBA/MPD of 2. The initial and relaxed structures are given in Fig. 5.4 as well as the variation of the total energy of epoxy films with time. The interfacial model (a = 70.067 Å, b = 74.899 Å, c = 101.415 Å, $\alpha = \beta = \gamma = 90.00^{\circ}$) containing 21,420 atoms is constructed by simply gathering both relaxed epoxy films and CSH (001) surface model. The initial distance between them is closed but not connected (2.71 Å). The initial and equilibrated configurations of interfacial model are shown in Fig. 5.5 as well as the variation of total energy of interfacial model with time.

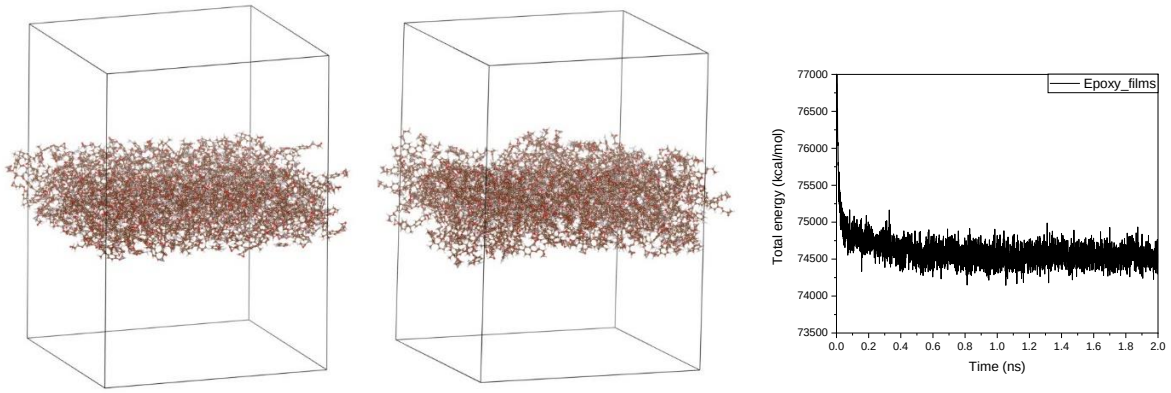

(a) (b) (c)

Fig. 5.4. Perspective view of epoxy film structures: the initial structure (a), the equilibrated structure (b), and the variation of the total energy of epoxy films with time (c).

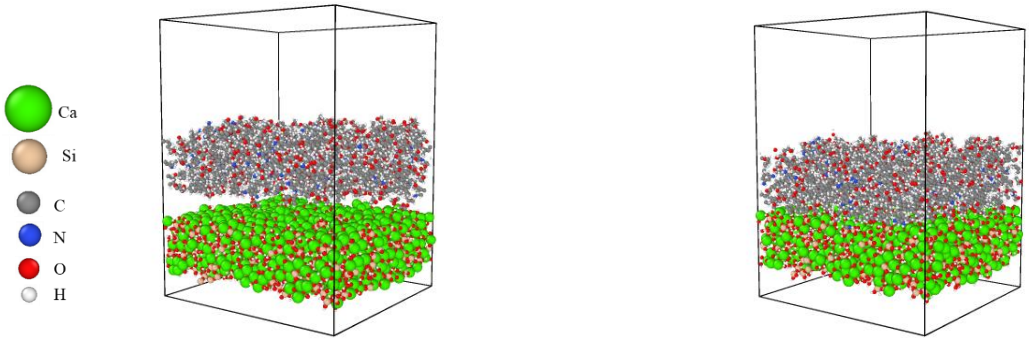

(a) (b)

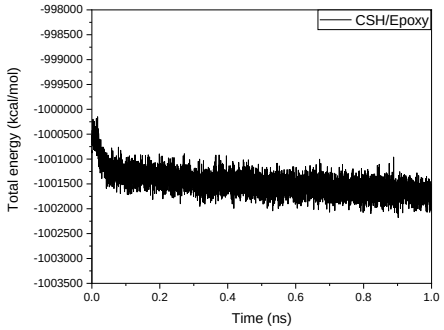

(c)

Fig. 5.5. Interfacial model: the initial structure (a), the equilibrated structure (b), and variation of the total energy of interfacial model with time (c).

5.2.3. Coated CSH-nanodroplet model

The generation details of a water-nanodroplet containing 500 water molecules utilized here is explained in our previous work [17]. It is constructed from water molecules placed in the middle of a box by adding roughly 30 Å vacuum onto the X, Y and Z direction of the water box. To construct the coated CSH-Nanodroplet model, we simply put the water-nanodroplet onto the equilibrated CSH coated surface. In this work, we have constructed 6 coated CSH-Nanodroplet structures to study the hydrophobicity of the coated (001) CSH surface. For instance, one of the

coated CSH-Nanodroplet structures containing 16,992 atoms is shown in Fig. 5.6. In this case, the initial distance between coated CSH and Nanodroplet is 3.51 Å.

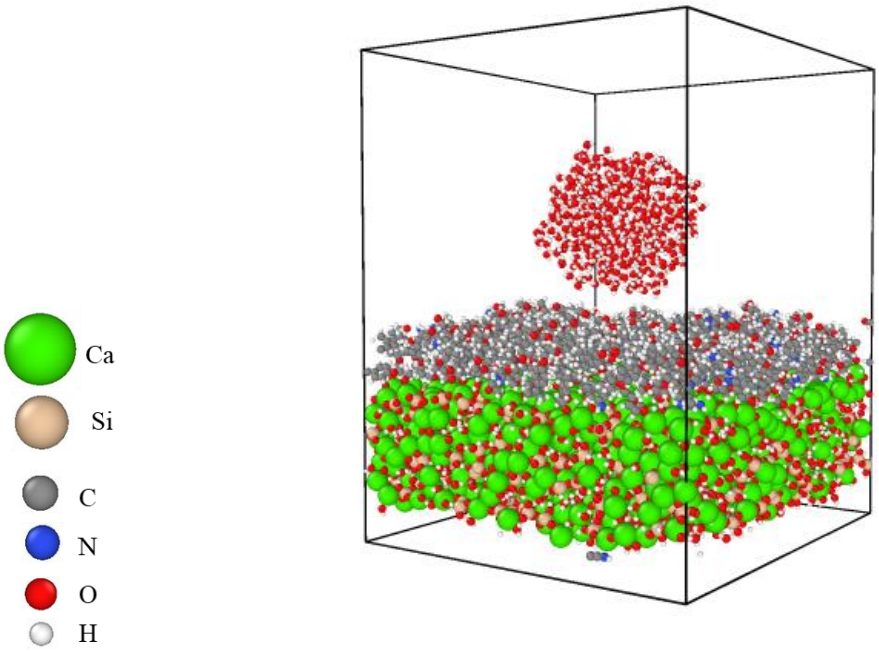

Fig. 5.6. Initial structure of water nanodroplet onto (001) coated CSH surface, cell parameters: a = 69.891 Å, b = 74.827 Å, c = 91.642 Å, $\alpha = \beta = \gamma = 90.00^{\circ}$.

Table 5.1

The Van der Waals radii used in this work.

Element	Van der waals radii	
	Organic	Inorganic
C	1.77	-
Ca	-	2.17
H	1.10	1.20
O	1.58	1.52
Si	-	2.15
N	1.64	-

5.2.4. Force field

A general force field [89] (CLAYFF), which is based on the single point charge [119] (SPC) water potential, has been utilized to simulate the interactions between atoms in CSH nanostructure. The total energy of CLAYFF potential is summed of Coulombic interactions, van der Waals interactions and the bonded interactions as shown in Eq. (5.1). The consistent-valence force field [88] (CVFF) has been employed to describe the interactions between atoms of epoxy coating. Its total energy is divided into a series of partial energy contributions as given in Eq. (5.2). The interactions between CSH surface and epoxy coating is represented following Lorentz-Berthelot rules [102].

$$E_{system} = E_{VDW} + E_{Coul} + E_{bond} + E_{angle}$$

$$= \sum_{i \neq j} 4\varepsilon_{ij}\left[\left(\frac{\sigma_{ij}}{r_{ij}}\right)^{12} - \left(\frac{\sigma_{ij}}{r_{ij}}\right)^{6}\right] + \frac{1}{4\pi\varepsilon_0}\sum_{i \neq j}\frac{q_i q_j}{r_{ij}} + K_r(r - r_0)^2 + K_\theta(\theta - \theta_0)^2 \quad (5.1)$$

$$E_{total} = E_{VDW} + E_{Coul} + E_{bond} + E_{angle} + E_{dihedral} + E_{improper} \quad (5.2)$$

Where E_{VDW} is van der Waals energy, E_{Coul} is Coulombic energy, E_{bond} and E_{angle} are harmonic bonded energy. r_{ij} is the distance between atom i and j, σ_{ij} and ε_{ij} are Lennard-Jones parameters calculated from Lorentz-Berthelot rules [102]. ε_0 is dielectric permittivity, q_i and q_j are charges of atom i and atom j, respectively, r and θ are bending harmonic bond and bending harmonic angle, respectively. r_0 and θ_0 are well relaxed harmonic bond length and angle, respectively, note that the general factor ½ is included in force constants K. $E_{dihedral}$ is harmonic dihedral energy, $E_{improper}$ is CVFF improper energy.

5.2.5. Simulation details

Large-scale Atomic/Molecular Massively Parallel Simulator [103] (LAMMPS) has been utilized for molecular dynamics simulations. Three-dimensional periodic boundary condition was applied and the equation of motion was integrated by using Verlet algorithm [120] with a timestep of 0.25 fs. The Van der waals interactions and Coulombic electrostatic interactions were truncated using a

cutoff of 10 Å. However, for bulk epoxy coated CSH, the used cutoff is 15 Å due to the roughness of the coated CSH surface. In addition, the long-range Coulombic interactions or long-range $1/r^6$ is calculated using particle-particle particle-mesh (pppm) method [121], as formulated in [122] with accuracy value of 10^{-4} in forces. The conjugate gradient algorithm was firstly used to have energy minimization with the structure optimization. Next, simulations were carried out under canonical (NVT) ensemble [107] using Nose-Hoover thermostat at T = 300 K. To evaluate the epoxy coated (001) surface energy, both the CSH surface coated model and the epoxy coated CSH bulk were simulated for 1 ns. To estimate the work of adhesion between epoxy and CSH, simulation of the interfacial model was done for 1 ns. Both epoxy films and CSH surface model were run for 2 ns. Regarding the hydrophobicity of coated surface, the coated CSH-Nanodroplet models were run for 1 ns. Molecular dynamics method is a powerful numerical tool, can serve as a bridge between macroscale experimental measurements and theoretical mechanisms. It has been widely used to study construction and building materials including cement paste, geopolymers, clays, …[30, 32-34, 108, 110, 123-125].

5.3. Results and discussion

5.3.1. Coated surface free energy

The epoxy coated (001) surface energy of CSH is determined according to Eq. (5.3). The method used to calculate the surface energy has been investigated previously [17, 104-106], as follows:

$$\gamma_s = \frac{E_{coated\_films} - E_{coated\_bulk}}{2A} \tag{5.3}$$

Where γ_s is the coated surface free energy, E_{coated_films} is the total energy of the coated surface structure, E_{coated_bulk} is the total energy of the coated bulk model, A is the area of the coated surface. The variation of the total energy with time of one of the CSH surface coated model is given in Fig. 5.3. It can be seen that the total energy of both coated films CSH and coated bulk CSH structure are converged after 1 ns. The total energy of the rest of coating models has the same behavior as the given one. To have a better top view of the coated surfaces, we represented it using Van der Waals radii (VDW) of atoms [118, 126]. The parameters used are given in Table 5.1. The top view of 7 equilibrated coating surfaces is given in Fig. 5.7. The coating surfaces is mainly divided into two types: one type is composed of pure epoxy molecules which corresponds to the 1st and the 2nd

coating surfaces. The other type is composed of epoxy with MPD corresponding to the rest of coating surfaces. It can be seen from the 1st and the 2nd coating surfaces that the coating percentage is increasing with increasing the wt% of pure epoxy molecules. Moreover, the 1st and the 4th coating surfaces show that MPD would highly improve the coating efficiency, however from the 3rd to the 7th coating surfaces it is noticed that the best coated surface is the 6th. The initial density, weight percentage and coating percentage are listed in Table 5.2. Therefore, the 2nd, 4th, 5th and 6th coating structures of Fig. 5.7 are used for evaluating the coated surface energy. The obtained values are ranging from 33.7 mJ/m^2 to 45.5 mJ/m^2, which have a highly agreement with the experimental results as given in Table 5.3.

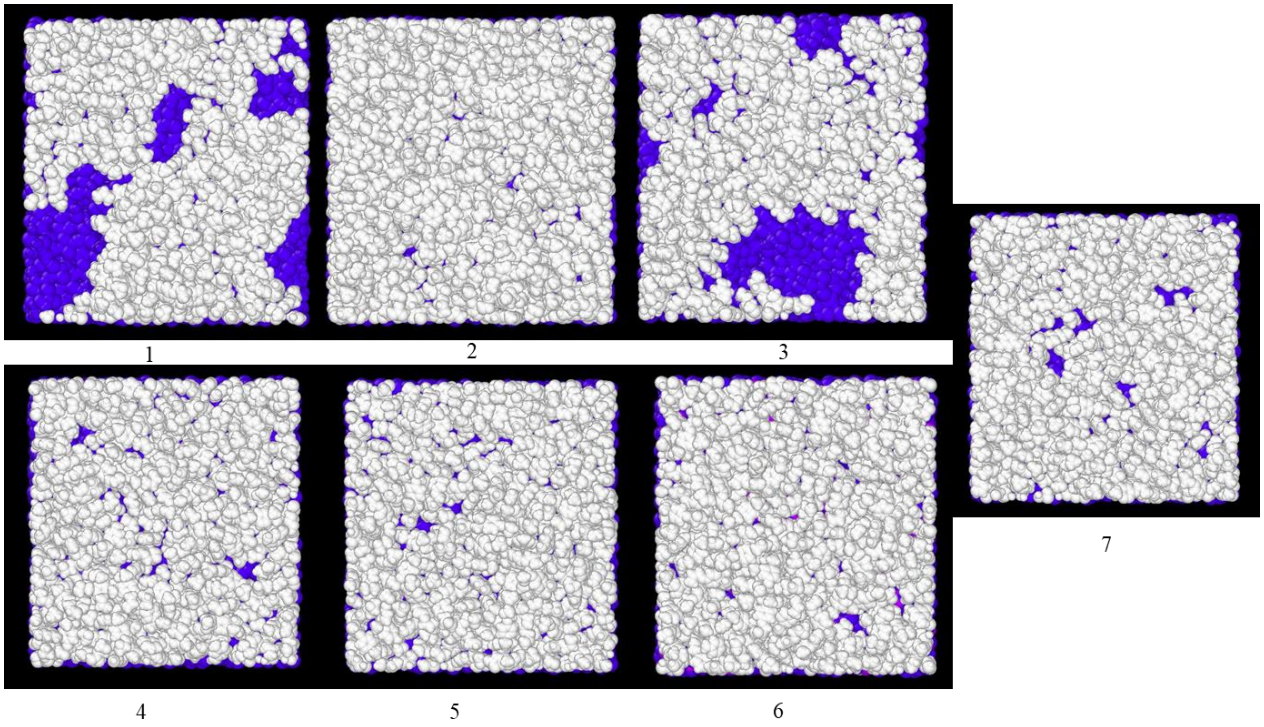

Fig. 5.7. Top view of the relaxed coating surfaces (white color) with the variation of epoxy and MPD (wt%), replotted using VDW radii of atoms.

Table 5.2

The initial density, weight percentage and coating percentage of coating surfaces.

Coating materials	Coating surfaces	Initial density (g/cm^3)	Weight percentage (%)		Coating percentage (%)
Epoxy with MPD	1	1.125	16.02^{E}	0.00	66.74
	2	1.140	22.88^{E}	0.00	98.08
	3	1.163	12.66^{E}	2.01^{M}	68.98
	4	1.128	15.62^{E}	2.48^{M}	95.84
	5	1.131	16.18^{E}	2.57^{M}	96.87
	6	1.132	16.46^{E}	2.61^{M}	96.95
	7	1.133	17.01^{E}	2.70^{M}	95.54

*Note that: the marked E and M represented epoxy and MPD materials, respectively.

Table 5.3

The surface energy of CSH with and without coating [17] compared with experimental [60] results.

Materials	Stoichiometry/Degree of hydration	Surface energy mJ/m^2
Cement paste with coating	0.3 (water to cement ratio)	28.2-53.1
	0.5 (water to cement ratio)	36.7-46.5
CSH without coating	$41Ca(OH)_2 31CaO 44SiO_2 \cdot 34H_2O$	698-740
CSH with coating(this work)		33.7-45.5

More interestingly, the coated surface energy is roughly 93% to 95% lost compared with the surface without coating, which means that epoxy coating could highly reduce the hydrophilicity of the (001) surface of cement paste. As reported in many previous works [5, 60, 61], high free surface energy would induce high hydrophilicity. Therefore, in this work, the reduction of hydrophilicity is due to the decrease of the surface energy of the coated CSH. Following Eq. (5.3), the calculation of the surface energy is based on the calculation of the total energy of the system. When the surface is coated by epoxy, the obtained total energy of the coated film is lower in comparison with the total energy of the film without coating. This came from the fact that the coated surface is more stable due to the interfacial bonding between CSH atoms and epoxy. Therefore, the difference between the total energy of the film and the bulk became smaller. This will give a small value of the surface energy of the coated film. The reason behind this behavior is the formation of chemical connections at the interface between CSH and epoxy: Ca^{2+}_{CSH}-O_{Epoxy}, O_{CSH}-H_{Epoxy}, and H_{CSH}-O_{Epoxy}, making the CSH/epoxy interface more stable, reducing the total energy of the system and leading thus to a lower surface energy. To have more information about the accommodation of coating

surfaces onto CSH, we represented the front and the left views of the 2nd, 4th, 5th and 6th coating surfaces corresponding to Fig. 5.7 using VDW radii, as presented in Fig. 5.8.

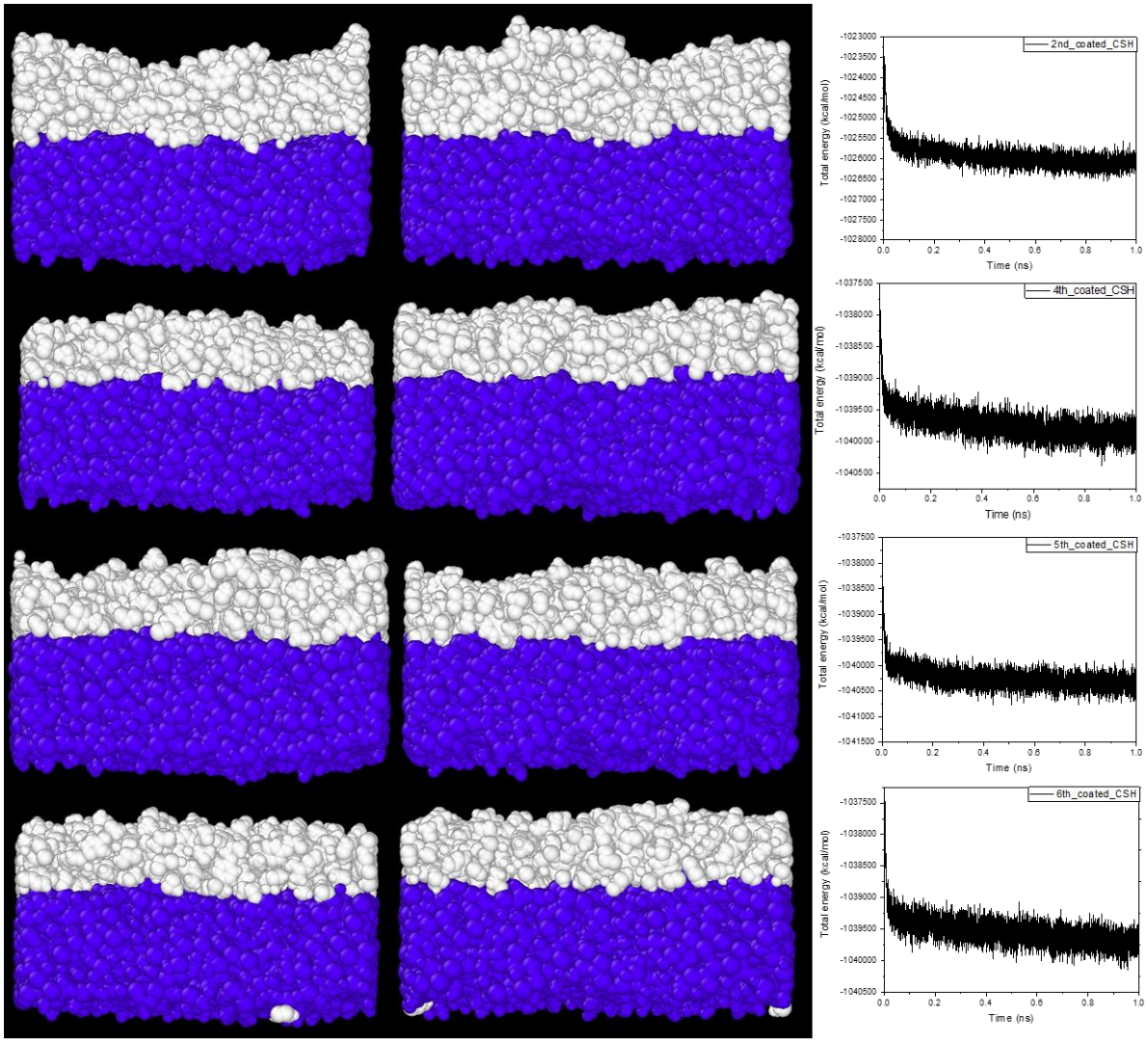

(a) (b) (c)

Fig. 5.8. Front view of coating surfaces (white color): from top to bottom corresponding to the 2nd, 4th, 5th and 6th coating surfaces of Fig. 5.7(a). The left view of coating surfaces corresponding to each front view (b). The total energy versus time corresponding to each structure of the front view (c).

It shows that the total energy of those four models is converged after 1 ns. It is observed that the 4th, 5th and 6th coating surfaces are thinner and with less roughness compared to the 2nd coating surface. For this reason, we only focus on the 4th, 5th and 6th coating surface. For the following, the 4th, 5th and 6th coating surfaces are renamed A, B and C coating surfaces for better recording. To dig more understanding of A, B and C coating surfaces, the mean squared displacement (MSD) is investigated as given in Fig. 5.9. The corresponding self-diffusion coefficient (D) is evaluated from the three-dimensional Einstein relation function as shown in Eq. (5.4) [127]:

$$D = \frac{1}{6}\frac{d}{dt}r(t)^2 \tag{5.4}$$

Where $r(t)^2$ is the mean squared displacement of the atoms, which is defined as $r(t)^2 = \langle |R(t) - R(0)|^2 \rangle$, $R(t)$ is atom position at time t. Fig. 5.9 shows that the slope of MSD was decreasing sharply at the beginning and gradually slowly within time. The inserted figures are the variation of MSD and diffusion coefficients in last 50 ps, respectively, indicating that epoxy resins diffuse onto CSH surface more slowly at the end than at the beginning of the simulation. The averaged self-diffusion coefficients from the last 50 ps are 9.58×10^{-11} m^2/s, 7.12×10^{-11} m^2/s and 1.11×10^{-10} m^2/s corresponding to coating surfaces A, B and C, respectively.

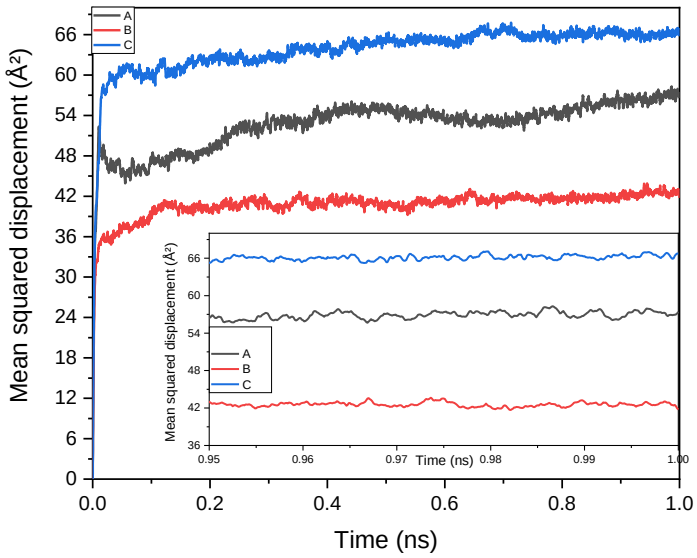

(a)

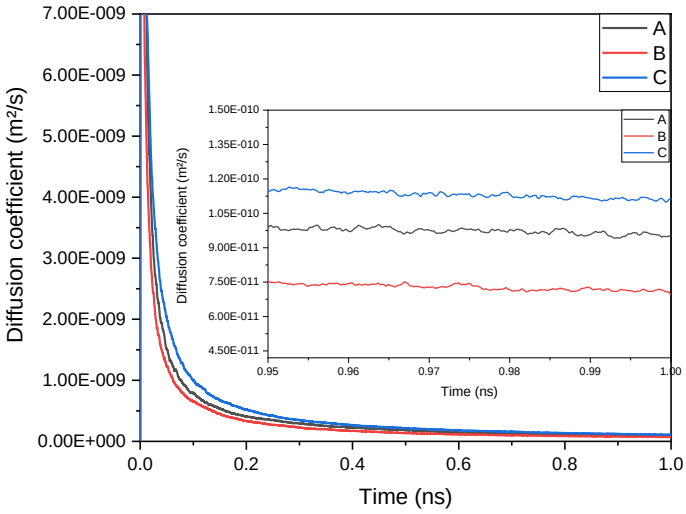

(b)

Fig. 5.9. Mean squared displacement (MSD) of A, B and C coating surfaces (a). Self-diffusion coefficient of A, B and C coating surfaces (b).

The density profile of coating surfaces, as shown in Fig. 5.10, has no big difference between the three coating surfaces. However, in the case of coating surface A, the curve has the most sharply peak and it is decreased deeper compared with the rest of the two coating surfaces. Besides, the density profile of coating surface C is fluctuating from 6 Å to 10.5 Å along Z direction roughly around 1.14 g/cm^3 and it has the smallest amplitude compared with the other two curves.

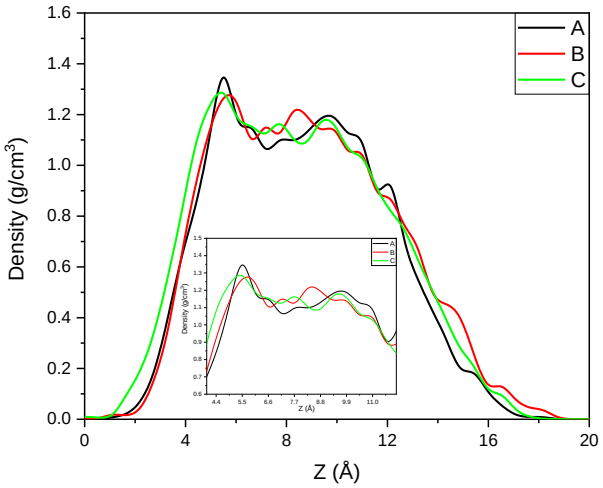

Fig. 5.10. Density profiles of equilibrated A, B and C coating surfaces.

Regarding the coordination correlations between CSH and coating surface, we analyzed radial distribution function (RDF) also named g(r), which is the probability of finding an atom at a radial distance r from another atom chosen as a center sphere reference. The partial pair correlation functions are given in Fig. 5.11 as well as the coordination number corresponding to each pair interaction. The cao notation is the surface calcium atom onto the CSH surface; c1 and c2 are Sp3 carbon atoms bonded 1 and 2 hydrogen atoms, respectively. o is oxygen atom belong to epoxy molecules; n2 and hn are nitrogen and hydrogen bonded to nitrogen atoms, respectively, and belonging to MPD molecules. It can be seen from Fig. 5.11 that the RDF between A, B and C coating structures have no big difference. For instance, from the pair interactions of the coating structure C, it can be seen that the first bond length of cao-c2 and cao-c1 pair interactions are 4.15 Å and 3.95 Å with a coordination number of 0.12 and 0.06, respectively. In addition, cao-o pair interaction has the first bond length of 2.55 Å with a coordination number of 0.02 in agreement with Hou's [128] and Hosseini's [129] studies that have proposed the distance of interfacial bonds of Ca–O pair in CSH/Epoxy structure to be from 2.35 to 2.55 Å. Moreover, cao-n2 and cao-hn pair interactions have the first bond length of 2.85 Å and 3.15 Å with a coordination number of 0.01 and 0.04, respectively. Hosseini [129] has proposed the interfacial bond Ca–N distance of 2.4 Å, which is closed to our studies. The results of all pair interactions of the three coating structures are listed in Table 5.4.

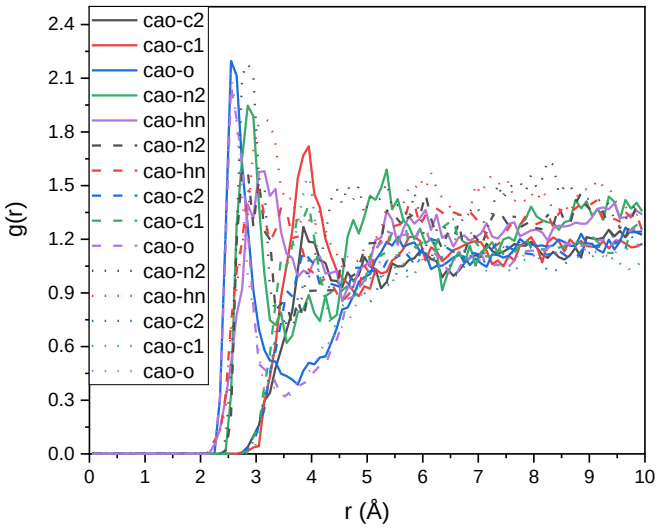

(a)

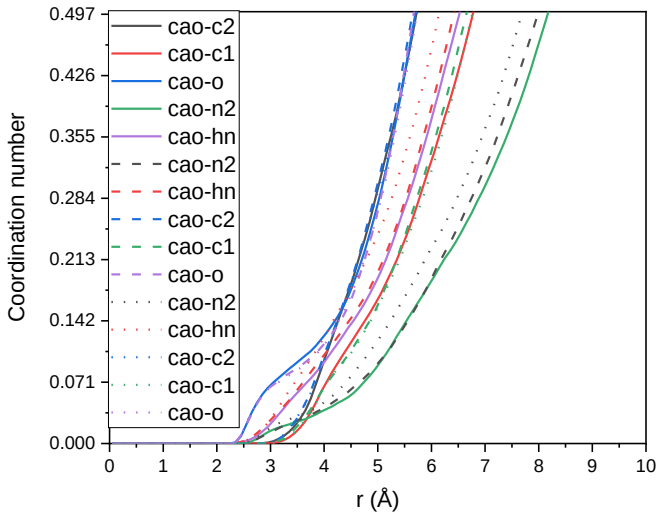

(b)

Fig. 5.11. Partial pair correlation function of A, B and C coating structures: the solid, dash, and dot lines are for A, B and C, respectively (a). The coordination number corresponding to each pair interaction (b).

Table 5.4

The first bond distance with the coordination number (CdN) in that distance of partial cao pairs of different coating surfaces.

	A		B		C	
	Bond (Å)	CdN	Bond(Å)	CdN	Bond(Å)	CdN
cao-c2	3.85	0.07	3.85	0.08	4.15	0.12
cao-c1	3.95	0.06	3.95	0.06	3.95	0.06
cao-o	2.55	0.02	2.55	0.02	2.55	0.02
cao-n2	2.85	0.01	2.80	0.01	2.85	0.01
cao-hn	3.10	0.03	2.85	0.02	3.15	0.04

5.3.2. Hydrophobicity of coated surface

The hydrophobicity is determined by evaluating the contact angle between equilibrated nanodroplet and coated CSH surface. This method has been utilized in previous studies [17, 112, 113] . To this end, each of A, B and C coating surface contributes to two models, which differs in

the initial position of water-nanodroplet at the coated surface. For instance, we named A1, A2 to distinguish the two models based on coating surface A. One of the 6 initial structures of water-nanodroplet onto coated CSH surface is given in Fig. 5.6.

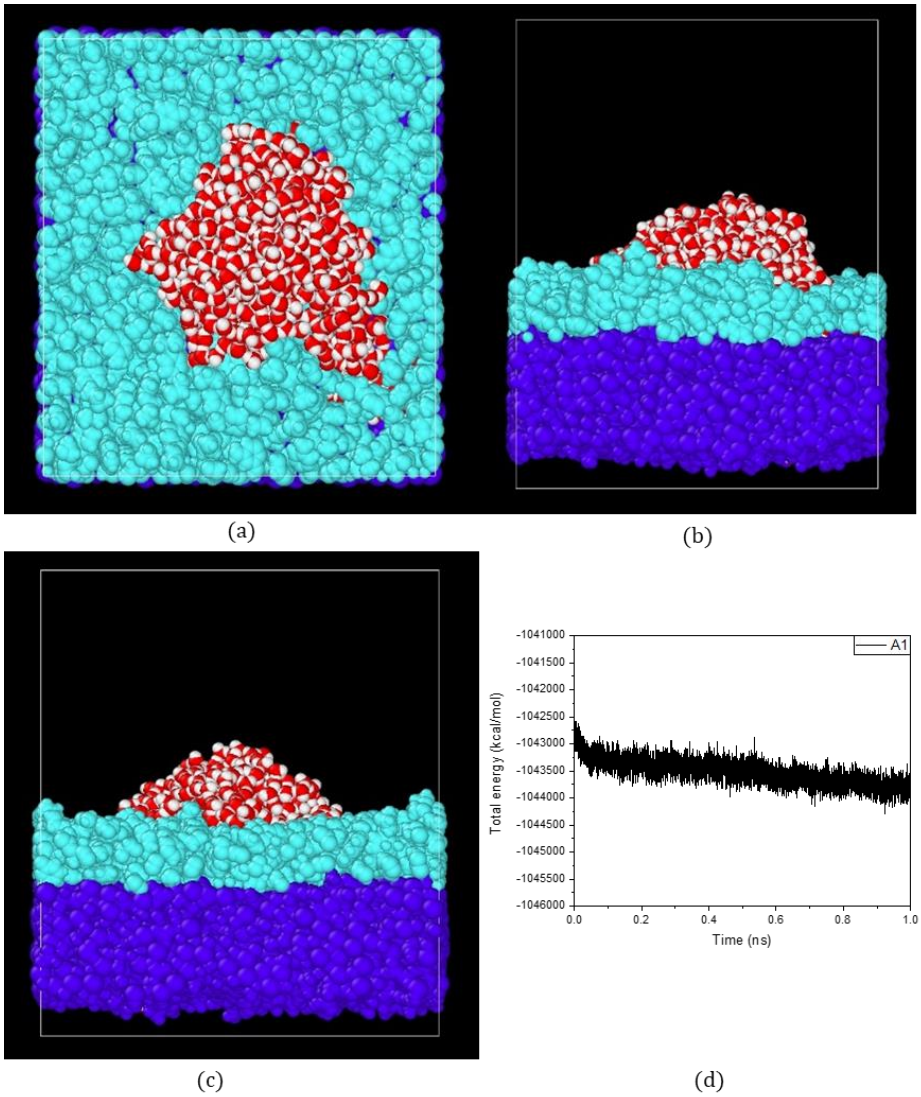

Fig. 5.12. Relaxed configuration of A1 model: The top view (a), the front view (b), the left view (c). The total energy of A1 model versus time (d). The white and red colors represent water molecules, the green and blue color are represented coating surface and CSH substrate, respectively. (For interpretation of the references to color in this figure legend, the reader is referred to the web version of this article.)

For coating A surface, the relaxed configurations of A1 model are represented in VDW radii, as given in Fig. 5.12 as well as the total energy of A1 structure versus time. Fig. 5.12 shows that the total energy of A1 model is converged after 1 ns and the spreading area of water nanodroplet is irregular onto coated surface. Moreover, the coating surface is removed in order to see how coating surface prevented water to diffuse, as presented in Fig. 5.13.

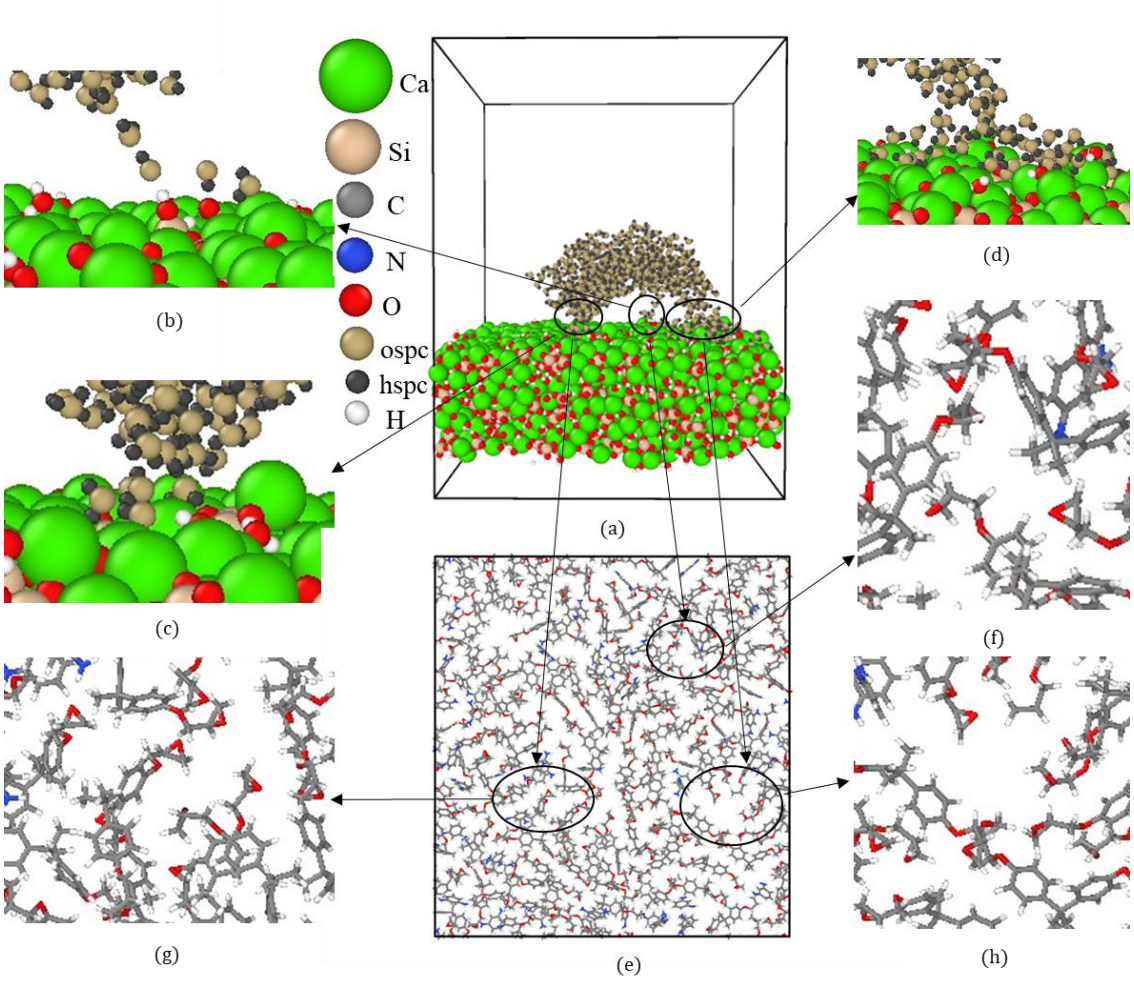

Fig. 5.13. Equilibrated structure of A1 model without coating surface (a). The enlarge site where water interacted with CSH surface (b), (c) and (d). The initial bond structure of coating surface (white color) (e). The enlarge site where gave the access of water (f), (g) and (h) corresponding to each (b), (c) and (d), respectively.

It can be seen from Fig. 5.13.d that in this model, most of adsorbed water molecules onto CSH surface correspond to the initial bond structure observed in Fig. 5.13.h. The molecules composed

the holes observed in Fig. 5.13.h are more faraway from each other compared with the rest of Fig. 5.13.g and f. To dig the holes area effect, A2 model is constructed by moving the initial position of waternanodroplet by 0.5 Å to away from the area of Fig. 5.13.h along X direction. It can be seen from Fig. 5.14 that the total energy of A2 model is converged after 1 ns. The top view, front view and left view of A2 structure are quite different compared with A1 structure. In addition, Fig. 5.15 shows that water molecules prefer going through coating from the area (as listed in Fig. 5.15.d) to CSH surface resulted in Fig. 5.15.b. Fig. 5.15.d shows that there is an area with one molecule marked at the bottom of the coating but the molecules at the top of the coating are more faraway from each other, forming a big hole where water molecules go through easily.

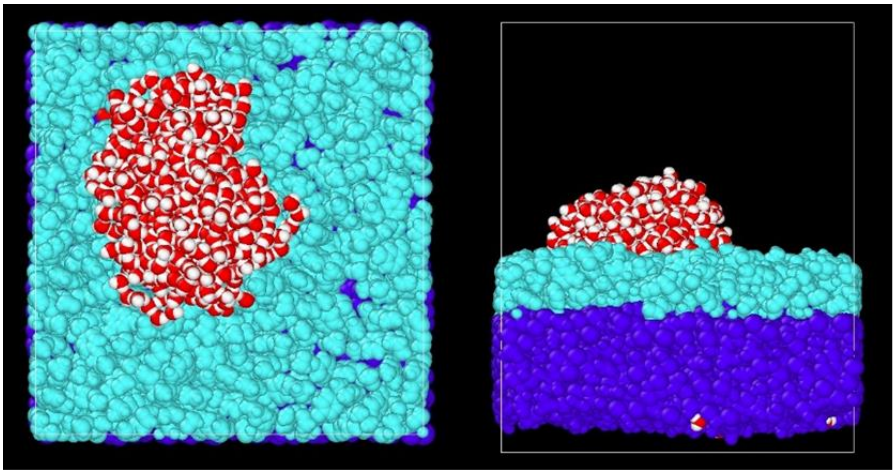

(a) (b)

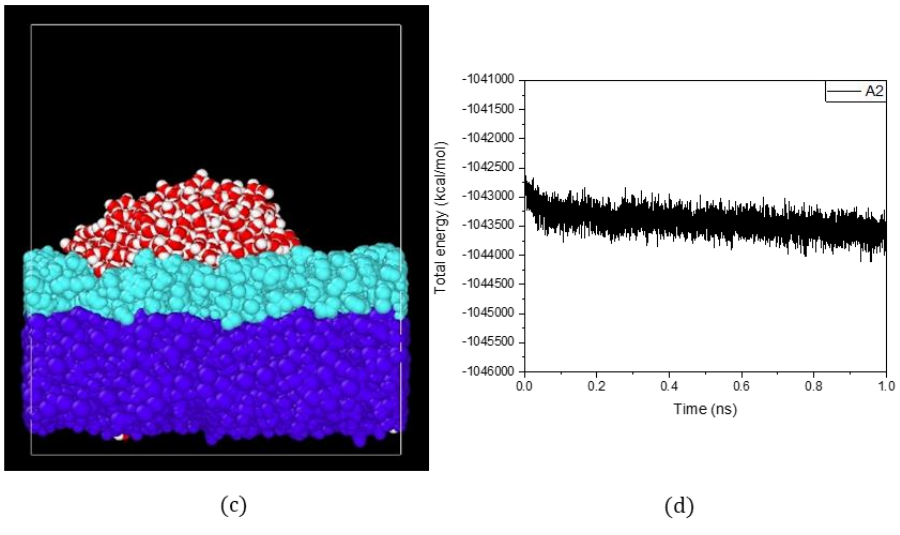

(c) (d)

Fig. 5.14. Equilibrated structure of A2 model: The top view (a), the front view (b), the left view (c). The variation of total energy of A2 model with time (d). Colors have the same meaning as used in Fig. 5.12.

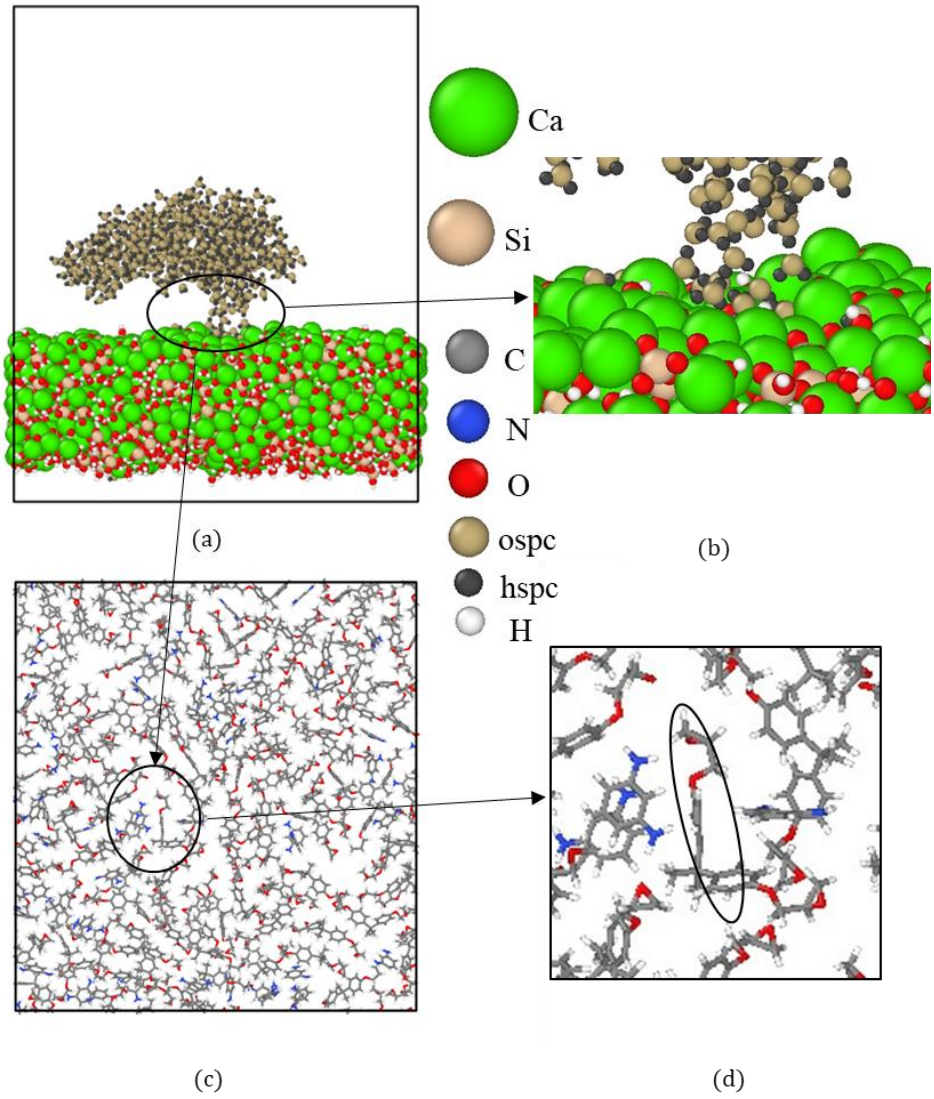

Fig. 5.15. Relaxed structure of A2 model without coating surface (a), the enlarge site where water interacted with CSH surface (b); the initial bond structure of coating surface (white color) (c). The enlarge bond site where gave the access of water (d).

We determined the hydrophobicity of coating surfaces B and C similarly as done to coating surface A. For coating surface B, it can be seen from Fig. 5.16 that the total energy of both B1 and B2 model are converged after 1 ns. It is noticed that the three directions' views are different from

B1 to B2 structure, especially for the spreading area of equilibrated nanodroplet. In the case of B1 model, it can be seen that water molecules like going through coating from the area of Fig. 5.17.f to CSH surface. Just a few of them could eventually adsorbed onto CSH surface, most of them were interacting with the coating materials composed of the slit hole. Nevertheless, one significant hole is observed in Fig. 5.17.i adjacent to Fig. 5.17.f. The reason that water prefers Fig. 5.17.f instead of Fig. 5.17.i is similar as the behavior observed in Fig. 5.15.d. For B2 model, it can be seen that after moving the initial position of nanodroplet of 1 Å along X direction, the water molecules like going through coating from the area of Fig. 5.17.g to CSH surface. The equilibrated state of the area of Fig. 5.17.g is given in Fig. 5.17.h.

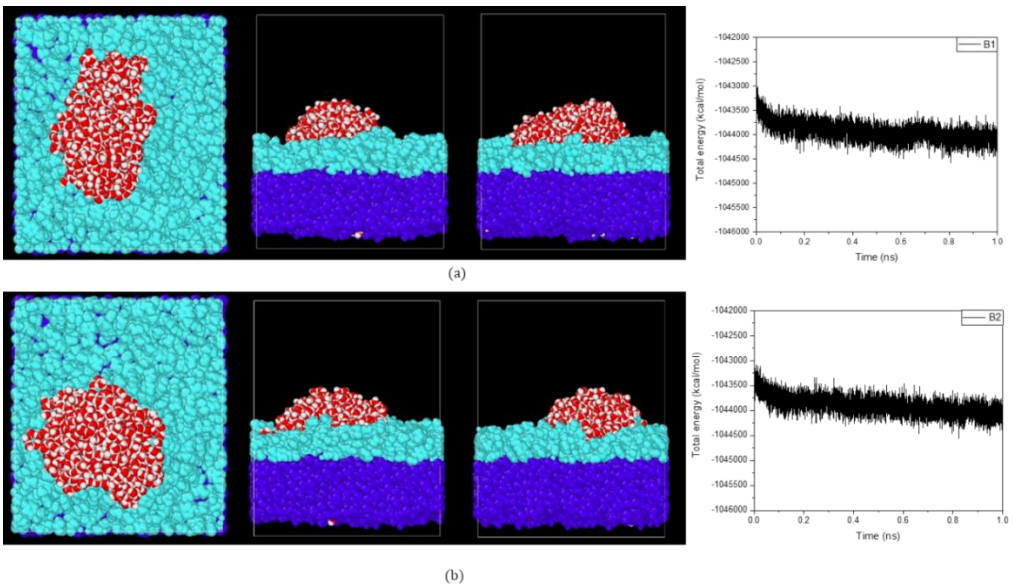

Fig. 5.16. From left to right: The top view, the front view, the left view and the variation of total energy with time of equilibrated B1 model (a), and of equilibrated B2 model (b). Colors have the same meaning as used in Fig. 5.12.

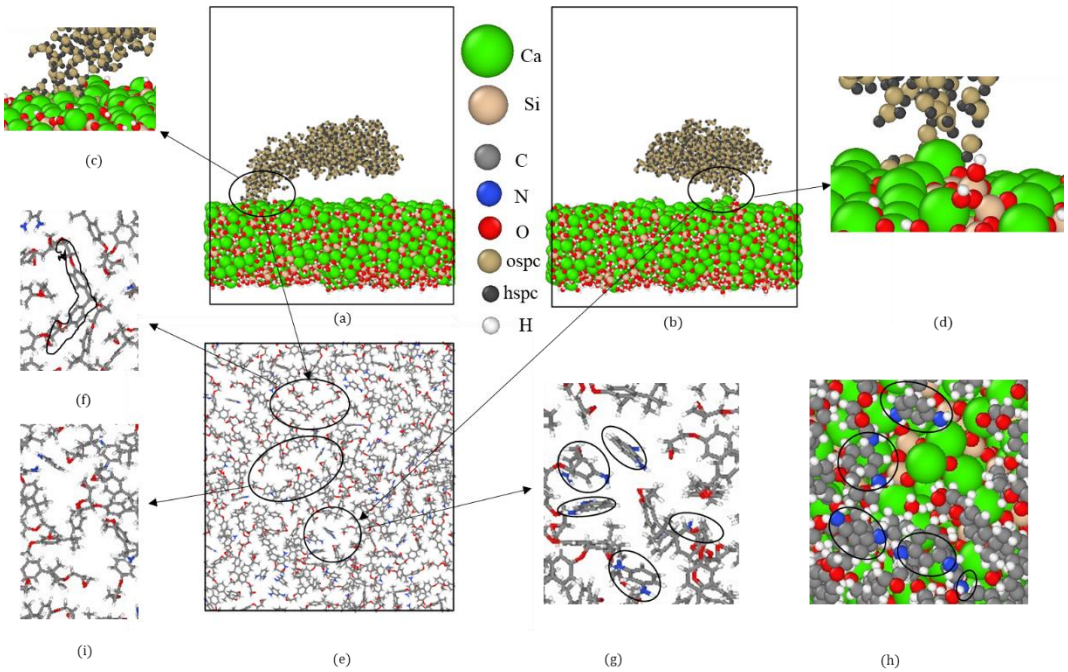

Fig. 5.17. Relaxed structure without coating surface: B1 model (a), B2 model (b). Enlarged place where water permeated corresponding to B1 model (c), B2 model (d). Initial bond structure of coating surface B (e). Enlarged bond site corresponding to B1 structure (f), B2 structure (g). Relaxed top view corresponding to g (h), an adjacent hole around f (i).

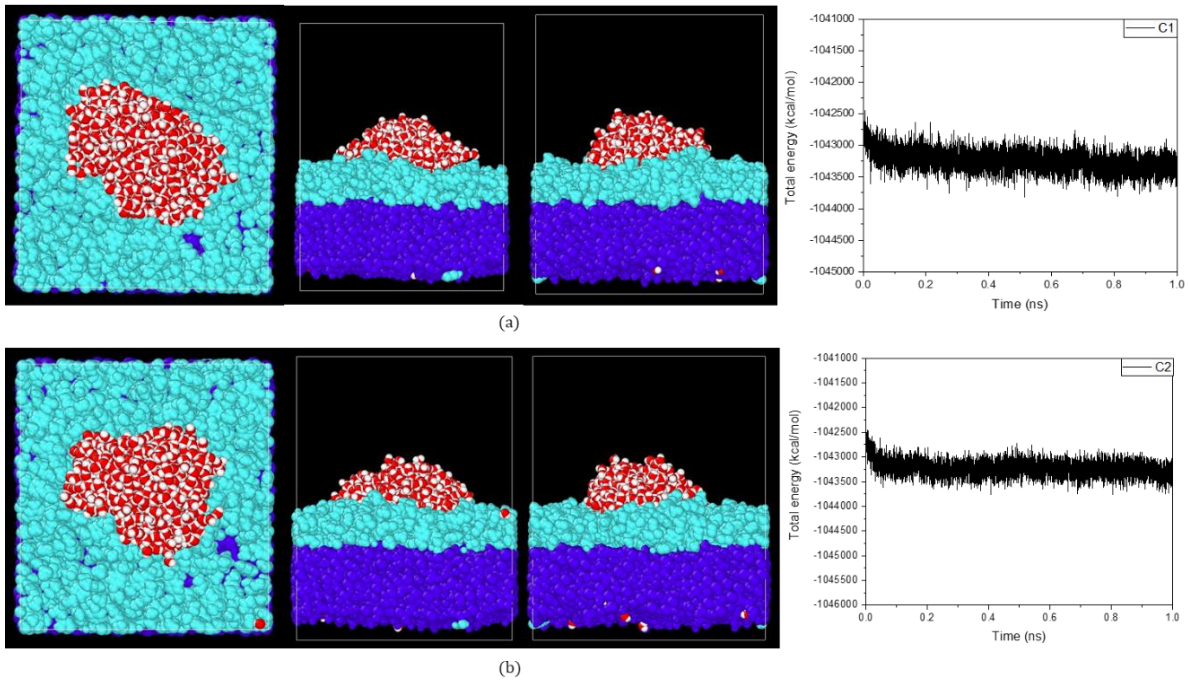

Fig. 5.18. From left to right: The top view, the front view, the left view and the variation of total energy with time of relaxed C1 model (a), relaxed C2 model (b). Colors have the same meaning as used in Fig. 5.12.

For coating surface C, it can be seen that the total energy of both C1 and C2 model are converged after 1 ns as given in Fig. 5.18. The three directions' views of C1 and C2 equilibrated states are different. Fig. 5.19.a shows that there is only one water molecule adsorbed onto CSH surface of C1 model. C2 model is constructed by moving the initial position of nanodroplet of 1 Å along Y direction and the results show that only one molecule went through coating and eventually it was being interacted with coating materials as marked in Fig. 5.19.d. The results of percentage of water molecules adsorbed onto the three coating surfaces during the simulation are listed in Table 5.5 and displayed in Fig. 5.20. Fig. 5.20 shows clearly that the coating surface C model is the best one for preventing water from CSH surface.

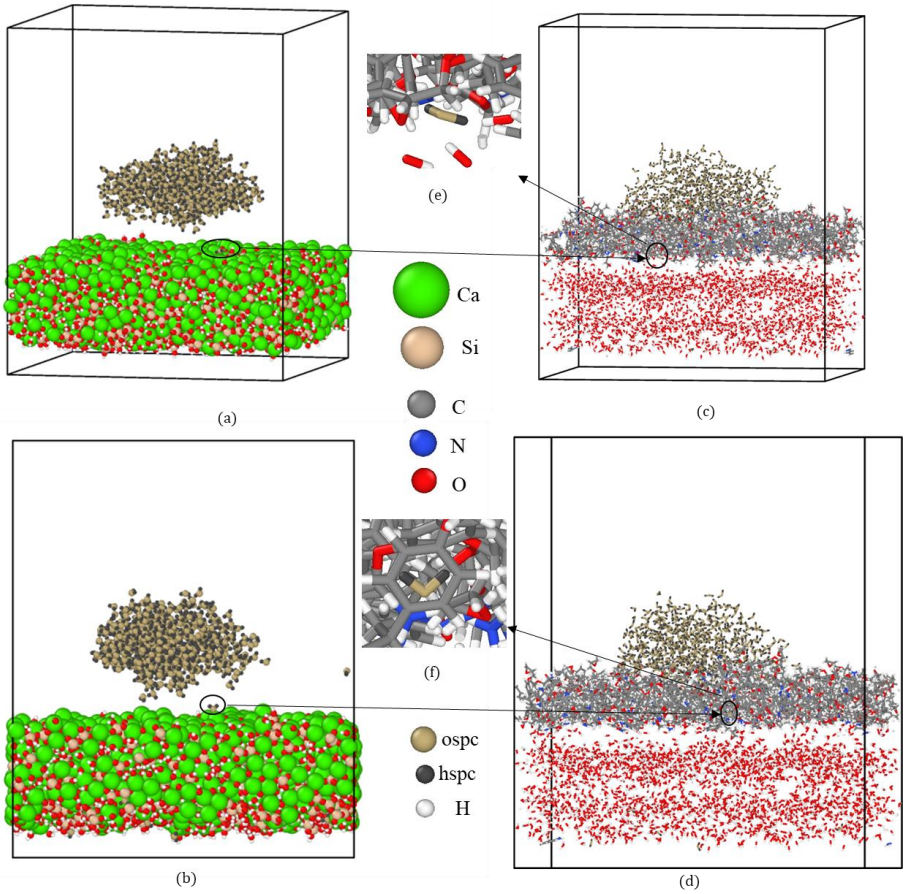

Fig. 5.19. Relaxed structure without coating surface: C1 model (a), C2 model (b). Equilibrated bond structure of C1 model(c), C2 model (d).

Table 5.5

The percentage (%) of adsorbed water onto A, B and C coating surfaces at different simulation time.

	A1	A2	B1	B2	C1	C2
0 ps	0.0	0.0	0.0	0.0	0.0	0.0
250 ps	0.0	0.0	0.0	0.0	0.2	0.0
500 ps	2.6	0.4	0.8	0.6	0.2	0.0
625 ps	3.2	1.2	1.4	0.6	0.2	0.0
750 ps	3.4	1.2	1.4	0.6	0.2	0.0
875 ps	3.2	1.2	1.4	0.6	0.2	0.0
1000 ps	3.4	1.2	1.4	0.6	0.2	0.0

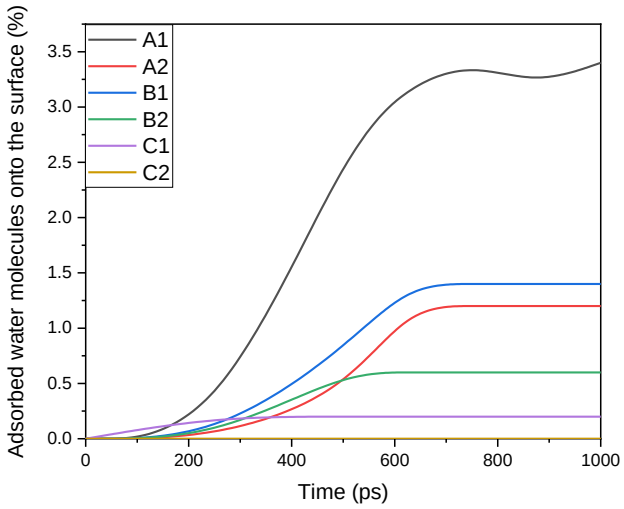

Fig. 5.20. Variation of water adsorption onto the coating surface with time.

Determining the averaged contact angles between equilibrated water-nanodroplet and coating surface is similar as used in our previous work [17]. The atomic positions of the last 50 ps data of the 6 CSH-Water nanodroplet models with an interval of 10 ps were extracted and then represented them in Cartesian coordinates. Next, the contact angles were evaluating from a simple geometry which was an appropriate tangent to close the surface of the relaxed nanodroplet profile with meeting the coating surface. All results of the contact angle are listed in Table 5.6, showing a good agreement with experimental results, expect the case of 48.06° from the left side of the left view of

B1. The water molecules have been being interacted, while through the coating to CSH surface as given in Fig. 5.17.a, mainly contributing to the low contact angle. It can be deduced that the contact angle highly increased (3.14–3.57 times) compared with the one without coating.

Table 5.6

The contact angle between water-nanodroplet and CSH surface with or without epoxy coating compared with experimental results.

Method	With/without coating	Contact angle(°)			
		Front view		Left view	
		Left side	Right side	Left side	Right side
Theoretical	A1	81.91	78.20	82.65	85.09
	A2	84.80	78.26	87.69	83.35
	B1	89.73	80.01	48.06	83.62
	B2 (this work)	79.28	75.68	79.14	88.99
	C1	84.29	87.30	86.12	89.60
	C2	89.84	86.78	88.41	91.97
Experimental	Without coating[17]	23.62-29.29			
	Epoxy resin coating [61]	77.50			

Table 5.7

The self-diffusion coefficients of coating surface and nanodroplet of the 6 models compared with our previous work [17].

Model	Diffusion coefficient (m^2/s)	
	Coating surface	Nanodroplet
A1	1.73×10^{-11}	6.27×10^{-10}
A2	1.45×10^{-11}	6.47×10^{-10}
B1	1.40×10^{-11}	8.92×10^{-10}
B2	1.45×10^{-11}	9.96×10^{-10}
C1	8.11×10^{-12}	6.18×10^{-10}
C2	9.23×10^{-12}	7.51×10^{-10}
Without coating	-	9.05×10^{-9}

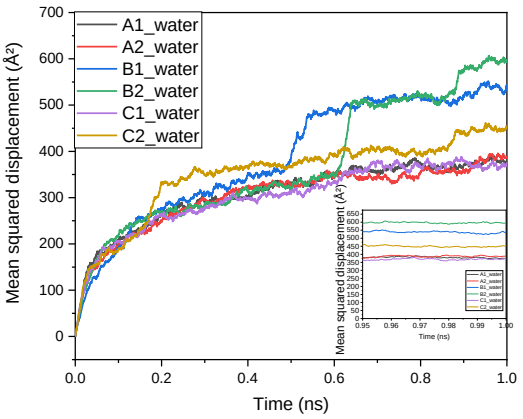
A1_water
A2_water
B1_water
B2_water
C1_water
C2_water
Mean squared displacement (Å²)
Time (ns)

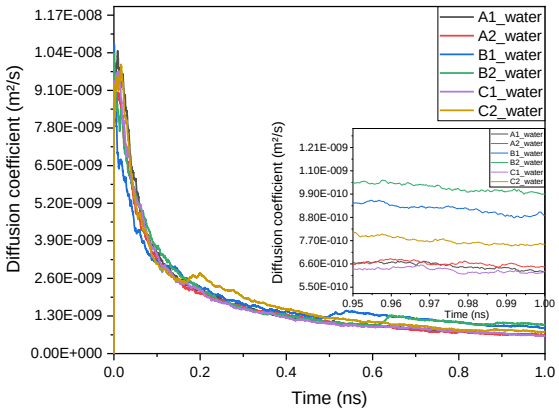
A1_water
A2_water
B1_water
B2_water
C1_water
C2_water
Diffusion coefficient (m²/s)
Time (ns)

(a)

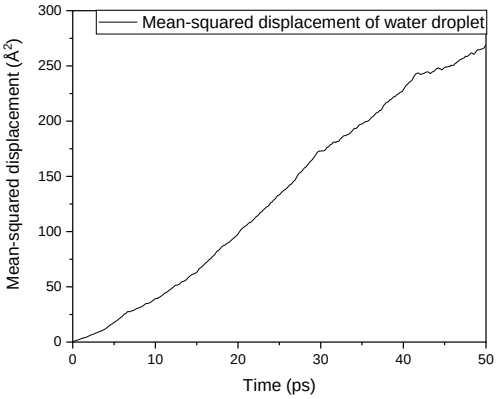
Mean-squared displacement of water droplet
Mean-squared displacement (Å²)
Time (ps)

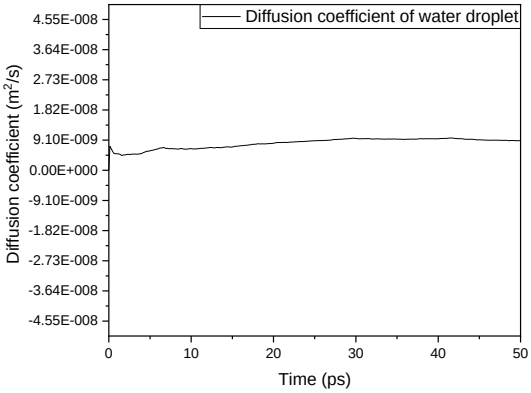
Diffusion coefficient of water droplet
Diffusion coefficient (m²/s)
Time (ps)

(b)

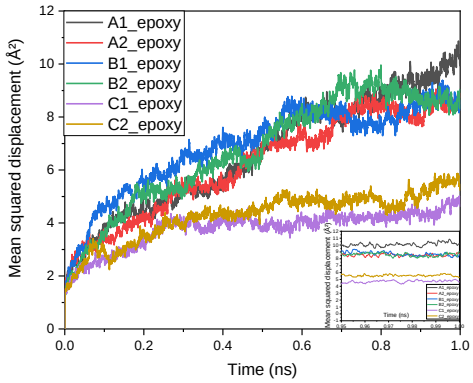
A1_epoxy
A2_epoxy
B1_epoxy
B2_epoxy
C1_epoxy
C2_epoxy
Mean squared displacement (Å²)
Time (ns)

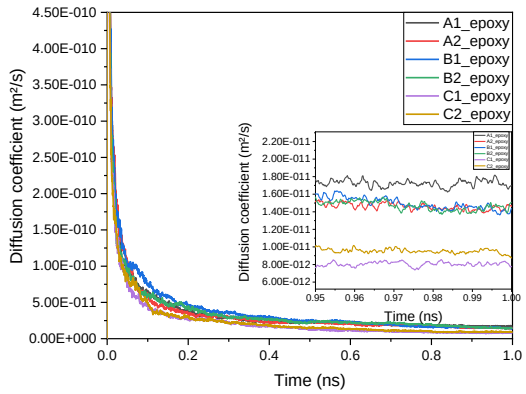
A1_epoxy
A2_epoxy
B1_epoxy
B2_epoxy
C1_epoxy
C2_epoxy
Diffusion coefficient (m²/s)
Time (ns)

(c)

Fig. 5.21. Mean squared displacement and self-diffusion coefficient of: water-nanodropelt (a), previous work [17] without coating (b) and coating materials (c).

To dig more understanding about hydrophobicity of the coating surfaces, we investigated the MSD and self-diffusion coefficient for both water-nanodroplet and coating surface of the 6 models. The inserted figures in Fig. 5.21 are the enlarged part of the last 50 ps data corresponding to each figure. Fig. 5.21 shows that the MSD of nanodroplet onto coated surface is increasing more slowly with time compared with our previous work [17] (without coating). The self-diffusion coefficient is quite smaller as well. The averaged self-diffusion coefficients from the last 5 ps of the 6 models compared with our[17] previous work are listed in Table 5.7. It is seen that the MSD of coating surface C is increasing more slowly compared with the rest of coating surfaces A and B. That means that the coating surface C is more stable; while it was being sandwiched between water-nanodroplet and CSH surface. Moreover, we investigated the partial correlation function of the 6 models, cao, c2, c1 and n2 having the same meaning as mentioned in coated surface free energy part. cp and c3 are Sp2 aromatic carbon in partial double bonds carbon ring and Sp3 carbon in methyl group, respectively. c is Sp3 aliphatic carbon atoms, ospc is oxygen atoms belong to water nanodroplet.

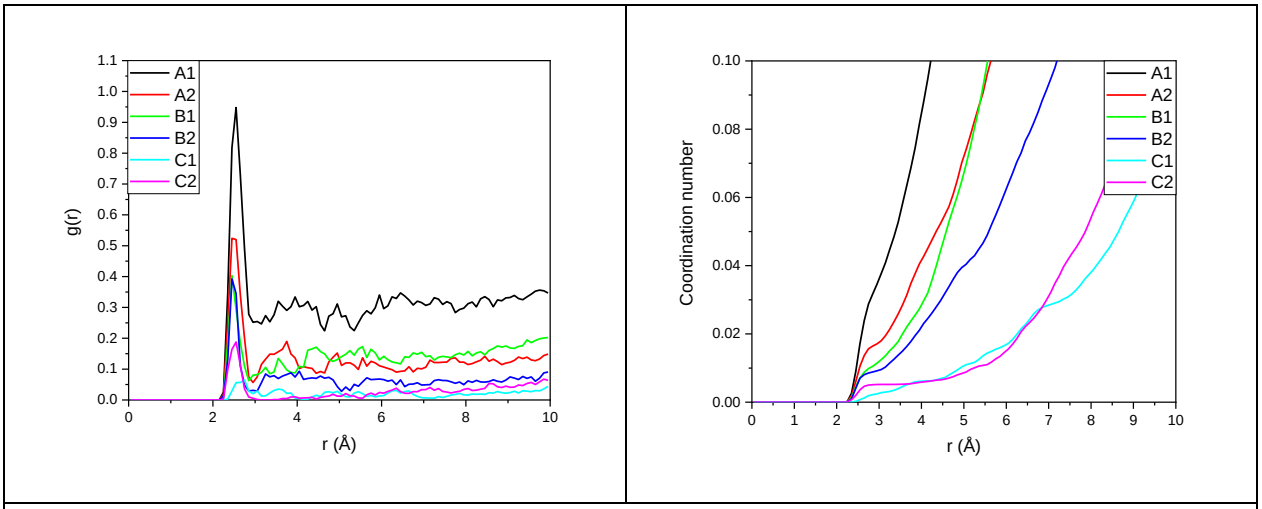

(a)

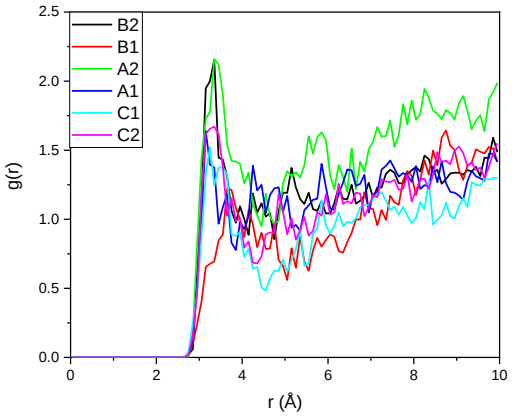
B2
B1
A2
A1
C1
C2
g(r)
r (Å)

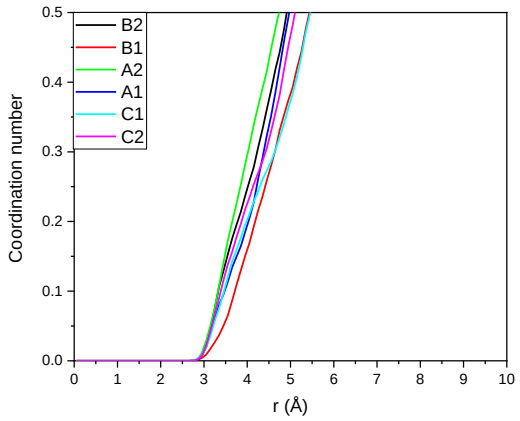
B2
B1
A2
A1
C1
C2
Coordination number
r (Å)

(b)

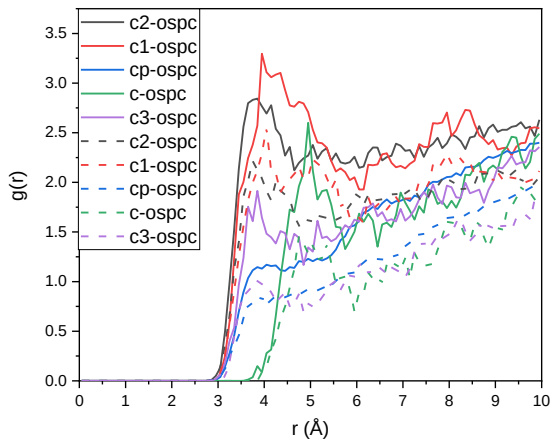
c2-ospc
c1-ospc
cp-ospc
c-ospc
c3-ospc
g(r)
r (Å)

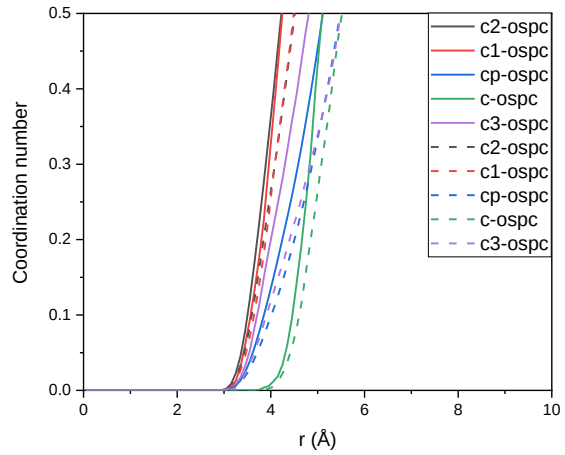
c2-ospc
c1-ospc
cp-ospc
c-ospc
c3-ospc
Coordination number
r (Å)

(c)

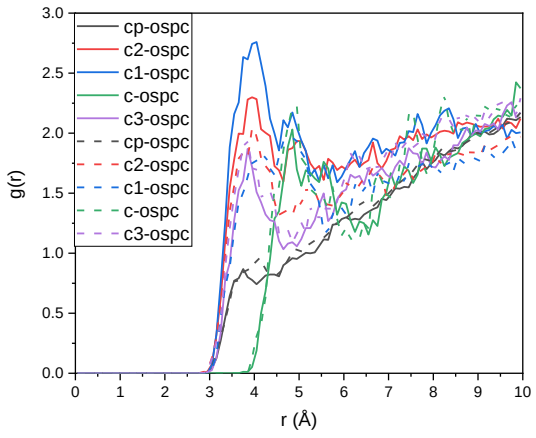
cp-ospc
c2-ospc
c1-ospc
c-ospc
c3-ospc
g(r)
r (Å)

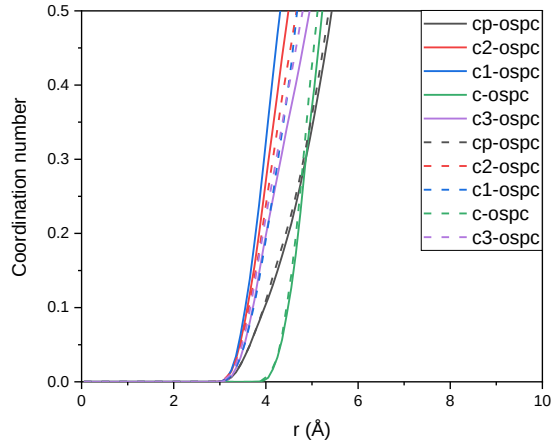
cp-ospc
c2-ospc
c1-ospc
c-ospc
c3-ospc
Coordination number
r (Å)

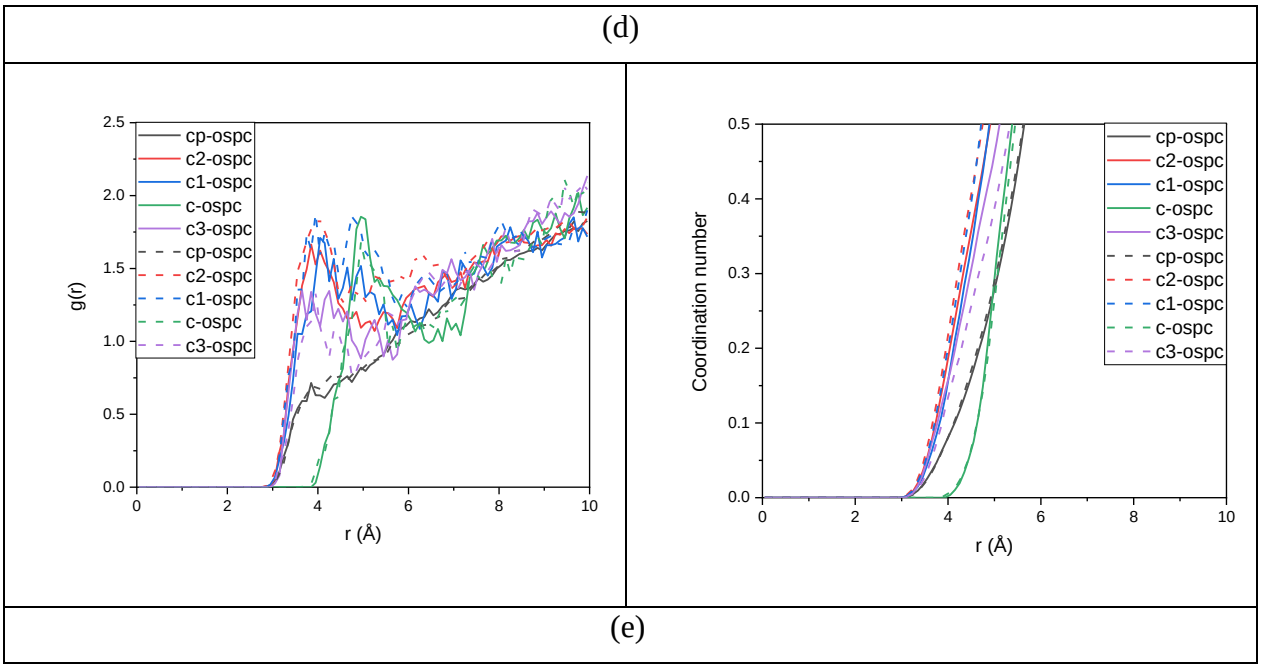

Fig. 5.22. Partial distribution function and coordination number of the 6 CSH-Nanodroplet structures: cao-ospc pairs (a), n2-ospc pairs (b), A1 (solid lines) and A2 model (dash lines) (c), B1 (solid lines) and B2 (dash lines) model (d), C1 (solid lines) and C2 (dash lines) model (e).

Fig. 5.22 shows that the radial distribution function of both cao-ospc and n2-ospc pairs has no big difference between the 6 models. Moreover, the c-ospc pair has the longest length of the first bond among the five types carbon-oxygen pairs. All results of the first bond length of each pair and the corresponding coordination number in that distance are listed in Table 5.8. At the end of this part, the mass density profiles of the equilibrated nanodroplet are investigated for the 6 models. Fig. 5.23 shows that the mass density profiles have no big difference between the 6 models. The mass density distribution of the equilibrated nanodroplet along Z direction from coated CSH surface is roughly 2 times higher than our previous work without coating [17]. The inserted figure in Fig. 5.23 is the enlarged part of the mass density profiles of the relaxed nanodroplet at the range of 0 Å to 8 Å away from CSH surface. Its results correspond to the behavior observed in each equilibrated CSH-Naonodroplet model with removed coating surface. For instance, it can be seen that there are no water molecules in the range of 1.5 Å to 6.1 Å of C1 model corresponding to the behavior observed in Fig. 5.19.a.

Table 5.8

The distance of the first bond and the coordination number in that distance for partial pair correlation of the 6 models.

	A1		A2		B1		B2		C1		C2	
	Bond (Å)	CdN	Bond (Å)	CdN	Bond (Å)	CdN	Bond (Å)	CdN	Bond (Å)	CdN	Bond (Å)	CdN
cao-ospc	2.55	0.02	2.45	0.01	2.45	0.00	2.45	0.00	2.75	0.00	2.55	0.00
n2-ospc	3.15	0.04	3.35	0.11	3.65	0.09	3.35	0.11	3.25	0.06	3.35	0.09
c2-ospc	3.85	0.28	3.75	0.16	3.95	0.25	3.95	0.22	3.85	0.14	4.05	0.24
c1-ospc	3.95	0.30	4.05	0.28	4.05	0.35	4.25	0.30	4.05	0.18	3.95	0.19
cp-ospc	3.85	0.10	3.95	0.09	3.75	0.07	4.05	0.12	3.85	0.06	3.85	0.06
c-ospc	4.95	0.40	4.75	0.16	4.85	0.29	4.95	0.38	4.95	0.27	4.95	0.25
c3-ospc	3.85	0.15	3.85	0.09	3.85	0.15	3.85	0.17	3.65	0.08	3.95	0.12

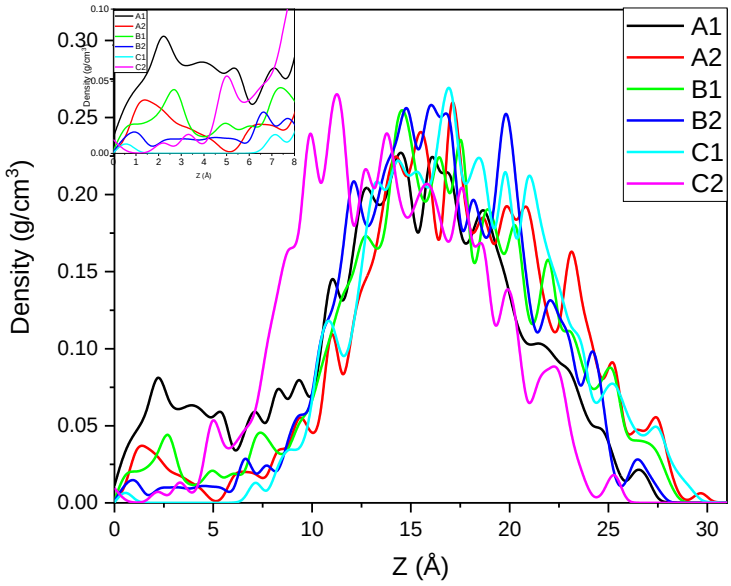

(a)

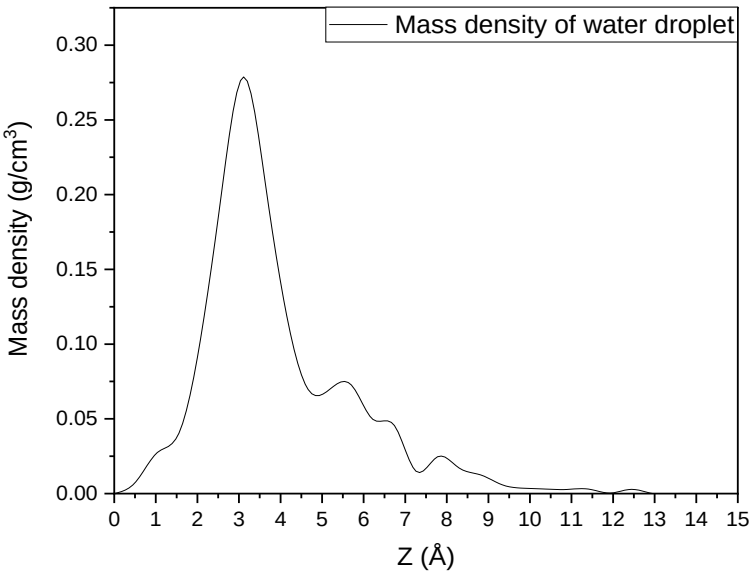

(b)

Fig. 5.23. Mass density profiles of equilibrated water-nanodroplet of the 6 models (a). Our previous work [17] (without coating) (b).

5.3.3. Work of adhesion

The work of adhesion between epoxy resins films and CSH surface is investigated from an interfacial model as mentioned in model construction part. The Eq. (5.5) has been utilized to estimate its value.

$$w_{ad} = \frac{(E_{films\_epoxy} + E_{films\_CSH}) - E_{interface}}{2A} \quad (5.5)$$

Where wad is the work of adhesion, E_{films_epoxy} and E_{films_CSH} are the total energy of epoxy films and CSH films, respectively. $E_{interface}$ is the total energy of the interfacial model, A is the one of interface between epoxy and CSH films. It can be seen from Fig. 5.1, Fig. 5.4 and Fig. 5.5 that the total energy of two films structures and interfacial model are all converged after 2 ns and 1 ns, respectively. The averaged value of the total energy is calculated from the last 100 ps data of the two films and interface structure, individually. The work of adhesion is estimated as 102.81 mJ/m^2, which is close to the experimental findings, proposed by Ilango [6], which give 102.79 and 90.17 mJ/m^2 corresponding to 2 and 28 days hydration of cement.

5.4. Conclusions

In this work, a deep atomistic level analysis is investigated on the interfacial adhesion between epoxy resin layer, (001) CSH surface and a droplet of water to understand the mechanism of the improvement of the wettability of the epoxy coated (001) CSH surface. The nanoscale structure of the full coated CSH is represented by gathering a confined layer cell of epoxy resins composed by DGEBA and MPD molecules and a realistic model of CSH. Seven proposed models have been built with different thicknesses of epoxy resin. Results show that m-phenylenediamine (MPD) would highly improve the coating efficiency. The calculated coated surface energy of CSH is in the range of 33.7 mJ/m^2 to 45.5 mJ/m^2, which in agreement with the experimental data, and its value is roughly 93% to 95% lost compared with the surface without coating. The averaged contact angle between the relaxed water-nanodroplet and the best coated CSH surface is found between 84.29° and 91.97°. This proves that epoxy coating highly decreased the hydrophilicity of (001) CSH surface. The obtained work of adhesion between epoxy resins films and (001) CSH surface is 102.81 mJ/m^2 in agreement with the experimental findings. Finally, our study show that 16.46 wt% of epoxy coating including 2.61% of MDP reduces by 3.14–3.57 times the hydrophilicity of CSH (001) surface, leading to a promising durable cement paste material.

Chapter 6:

Theoretical process of rubber nano-coating on calcium silicate hydrate film for durable cementitious materials

6.1. Introduction

Due to the experimental observation limitations to understand the mechanism behind the success hydrophobic behavior of CSH surface coated by a rubber film, there is a need to deeper analyze tthe atomic level the nano-coating procedure. Thanks to the developing of nanoscale modeling and simulation tools, it is possible to quantify the interfacial interatomic interactions between rubber and CSH constituents via the radial distribution function, and analyze how the adhesion between them is and what is the principal constituent responsible to enhance the wettability of CSH surface. The present work analyzes, for the first time, the interfacial interaction between a layer of rubber and (001) CSH surface at the nanoscale level. Using atomistic simulation tools, our aim is to describe the nanocoating efficiency of rubber to enhance the wettability of CSH surface and to explain the various atomistic interactions behind this improvement. The hydrophobic agent utilized here is rubber (Polybutadiene or Polyisoprene). To this end, a developed realistic model of Pellenq et al. [24] has been employed to represent the interatomic model between CSH and rubber. First, the (001) CSH surface analysis is performed to estimate the surface energy before and after rubber nanocoating process. Then, the contact angle between water nanodroplet and the coated CSH surface is evaluated and compared to other theoretical works and experimental measurements. Finally, the interfacial interaction between rubber and CSH film is deeply probed in order to get the best adhesion between both materials.

6.2. Modeling and simulation details

6.2.1. Construction of nano-coated CSH model

In the present work, our CSH model is based on the developed realistic model of Pellenq et al. [24] with a new Ca/Si ratio of 1.64. More information could be found in the following literatures for constructing the realistic CSH model [24, 27, 29]. To construct the rubber coated CSH surface model, we simply put a confined layer of amorphous cell of rubber onto a well relaxed (001) surface of CSH that is derived from 5 × 4 × 1 bulk CSH model of our previous work [17]. In addition, the 5 × 4 × 1 bulk CSH is transformed from a triclinic system to an orthogonal system while maintaining the relative positions of atom inside of CSH during the transformation. The (001) surface model of CSH is then constructed by adding approximately 60 Å of vacuum along Z direction onto the transformed relaxed 5 × 4 × 1 bulk CSH. The structural properties validated by experimental accessible parameters of the coated CSH model are given in the supplementary

materials. Two types of rubber have been taken into account, one is Polybutadiene elastomer also called a synthetic rubber and the other one is Polyisoprene polymer also called natural rubber. Due to the different of position of $–CH_3$ and –H along carbon bone, the Polyisoprene can be recognized into two different atomistic structures [130], one is called 1,4-trans-Polyisoprene (TPI) when $–CH_3$ and –H are put at the opposite side alone carbon bone; the other one is called 1,4-cis-Polyisoprene (CPI) while $–CH_3$ and –H are put at the same side alone carbon bone. For Polybutadiene, it has the same behavior as Polyisoprene: if –H and –H are put at the opposite side along carbon bone then it is called 1,4-trans-Polybutadiene(TPB); otherwise, it is called 1,4-cis-Polybutadiene(CPB). During simulations, each of the rubber single chain contains 10 repeating units. The schematic of the repeating units of TPI, CPI, TPB and CPB models are given in Fig. 6.1(a), as well rubber coated CSH surface structures. The appropriate distance between rubber coating and CSH is investigated by varying the interfacial distance and calculating the corresponding total energy for the coated CSH film. The most appropriate distance between rubber and CSH film is found about 1.013 Å.

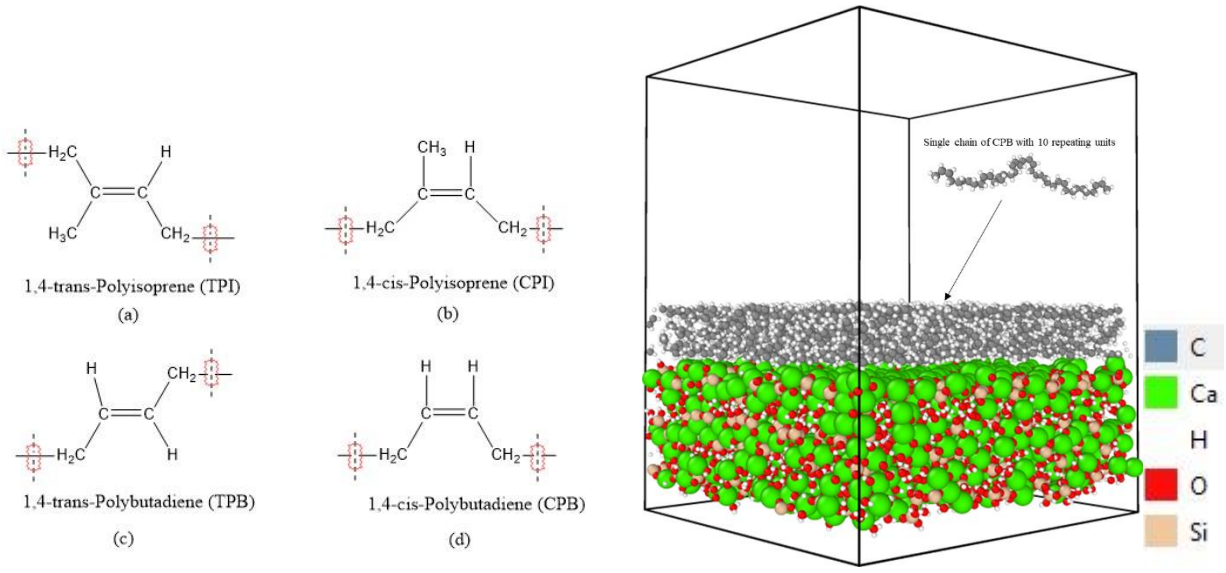

(a) (b)

Fig. 6.1. The schematic of the four types repeating units of rubber (a), the initial structure of CPB coated CSH, cell parameters: a = 68.652 Å, b = 73.353 Å, c = 89.100 Å, α = β = γ = 90.00° (b).

Regarding the dosage process of CPB and TPI, the main idea is to vary the weight content of CPB and TPI until we obtain the fully coated (001) surface. For TPI structure, it is varying from 14.54 wt% to 20.33 wt%. Results indicated that 18.96 wt% and 20.33 wt% of TPI coating could be

able to make CSH almost fully coated with a coating percentage up to 98.05%. To compare the coating ability between TPI and CPI, we fix the dosage at 18.96 wt%. Results indicated that the coating capability of TPI is better than CPI. For CPB and TPB, by fixing a dosage of 16.86 wt%, results indicate that CPB behave a superior coating ability than TPB coating. For lower content of 15.67 wt%, no good coating ability is observed. The present technique has been already used in our previous work on epoxy resin [18].

Two interfacial models, named CSH-CPB or CSH-TPI, are constructed for determining the work of adhesion between the rubber and CSH film. To this end, it is simply by gathering the two well relaxed structures of rubber film and CSH surface model. For instance, the initial structure of CSH-CPB interfacial model (a = 68.475 Å, b = 73.196 Å, c = 102.817 Å, $\alpha = \beta = \gamma = 90.00^{\circ}$) containing 21,546 atoms is given in Fig. 6.2 as well as the corresponding relaxed structure, and the variation of the total energy of each of interfacial models in time. The minimum initial distance between the CPB film and the CSH film is roughly 1.644 Å.

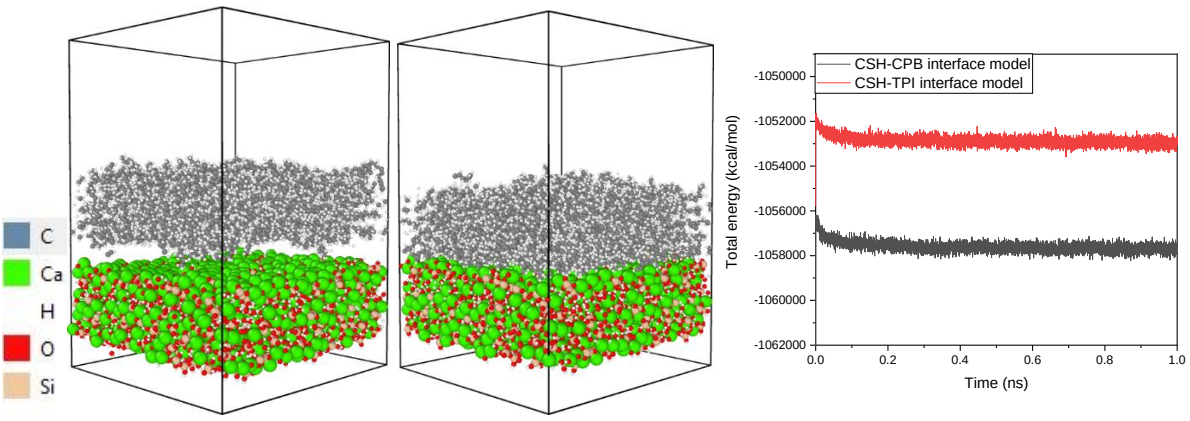

(a) (b) (c)

Fig. 6.2. The CSH-CPB interfacial model: initial structure (a), relaxed structure (b), and variation of the total energy of CSH-CPB (CSH-TPI) model with time (c).

6.2.2. Modeling water nanodroplet on (001) coated CSH surface

The water nanodroplet containing 500 molecules is generated from a water box with a free boundary condition, as presented in details in our previous work [17]. The nanodroplet is then placed onto the relaxed (001) CSH surface. To get a better adsorption process, a vacuum of 20 Å is add along the Z direction of the supercell. For instance, the initial structure of CPB coated CSH-

nanodroplet model (a = 68.529 Å, b = 73.221 Å, c = 108.904 Å, α = β = γ = 90.00°) containing 17,640 atoms is given in Fig. 6.3 as well as its equilibrated structure, and the variation of its total energy with time. In this case, the interfacial distance between the nanodroplet and the nano-coated CSH film is approximately 1.593 Å.

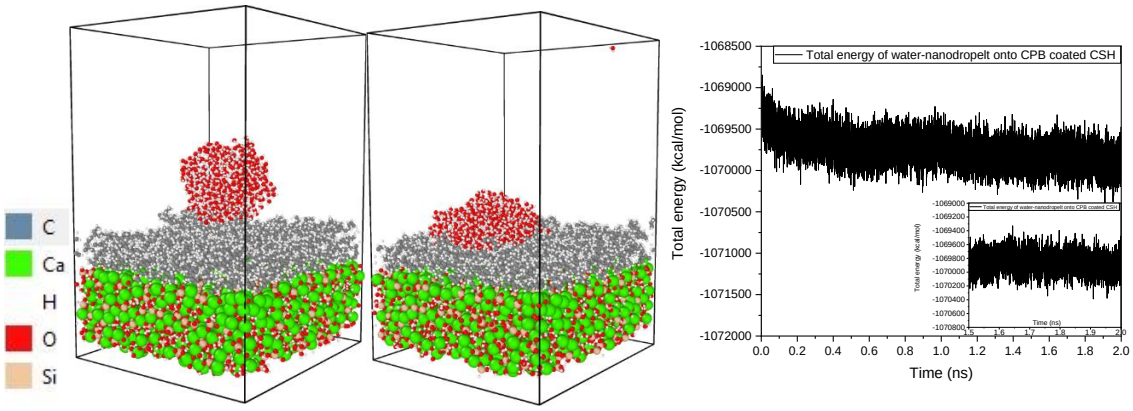

(a) (b) (c)

Fig. 6.3. CPB coated CSH-Nanodroplet model: the initial structure (a), the relaxed structure (b), and the variation of its total energy with time (c).

6.2.3. Force field description

The combination of the general force field (CLAYFF) [89] and the consistent-valence force field (CVFF) [88] has been employed to describe the interactions between atoms. Moreover, the CLAYFF potential is based on the single point charge (SPC) water potential [119], which is utilized for simulating the interactions between CSH atoms. The total energy is divided into the non-bonded interactions and the bonded interactions as presented in Eq. (5.1). In addition, the CVFF potential is used to simulate the interactions between rubber's atoms, its total energy is contributed by a series of partial energy as listed in Eq. (5.2). Nevertheless, the interactions between CSH and rubber coating is using Lorentz-Berthelot rules [102].

6.2.4. Simulation details

Large-scale Atomic/Molecular Massively Parallel Simulator (LAMMPS) [103] has been employed for molecular dynamics simulations. For conducting the simulations, three dimensional periodic boundary conditions are used in the simulation boxes. The Verlet algorithm [120] was

employed to integrate the equation of motion with a timestep of 0.25 fs. A cutoff of 10 Å is applied for determining the Van der walls interactions and the Coulombic electrostatic interactions. A cutoff of 15 Å is used for simulating the non-bonded interactions of rubber coated CSH bulk structure. In addition, a particle–particle particle-mesh (pppm) method [121] was used for evaluating the longrange Coulombic interactions or long-range $1/r^6$ interactions with an accuracy value of $1.0e^{-4}$ [122]. All models were firstly energy minimized using the gradient conjugate (cg) algorithm, then the simulations were conducted under canonical (NVT) ensemble [107] using Nose-Hoover thermostat at T = 300 K for 1 ns. To investigate the hydrophobicity, the dynamical mobility of the nanodroplet on the rubber coated CSH surface was simulated for 2 ns.

6.3. Results and discussion

6.3.1. Surface analysis

We first investigated the coating capability between TPI and CPI at the same wt.% condition as well as between TPB and CPB, to have a clear view on the coating efficiency. In Fig. 6.4, it is illustrated the top views of the relaxed coating surfaces using Van der Waals (VDW) radii's atoms of each model [118, 126]. It is noticed (Fig. 6.4) that for the same weight content of TPI, CPB, CPI and TPB we get a fully coated surface in the case of TPI and CPB in comparison to CPI and TPB. This is mainly induced by the difference of the atomistic structures of rubber. For this reason, we only focus on TPI and CPB coating in the following work. To dig more understanding of rubber coating onto CSH, the rubber concentration and thickness are varied to find the lowest amounts that give a better impermeability.

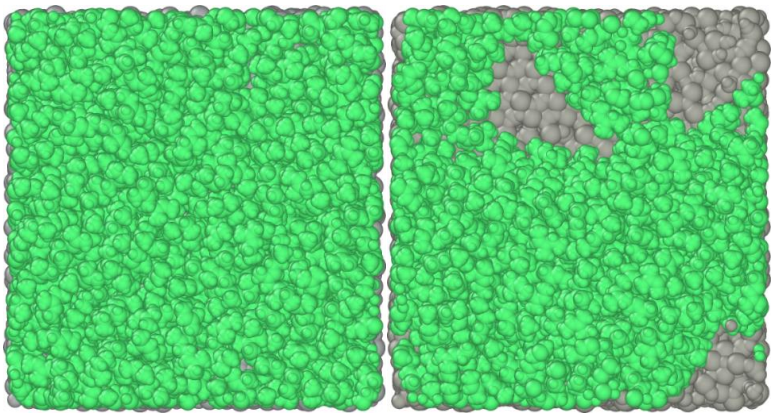

(a)

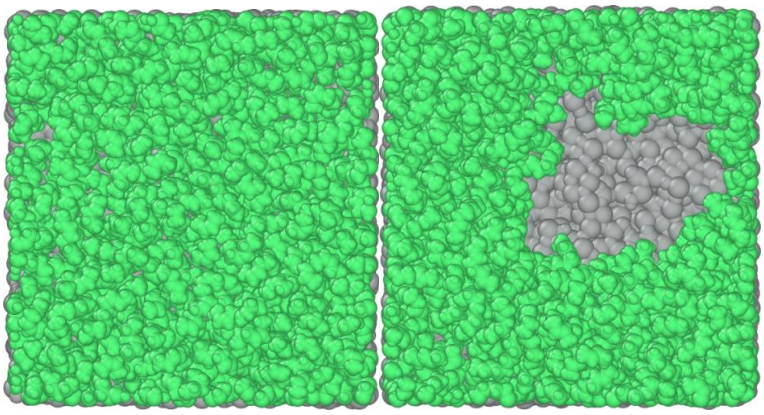

(b)

Fig. 6.4. Coating capability between TPI (left) and CPI (right) (a), and between CPB (left) and TPB (right) (b). The green color and gray color represent the coating and CSH, respectively. (For interpretation of the references to color in this figure legend, the reader is referred to the web version of this article.)

Fig. 6.5 depicts the top view of the relax configurations of the three rubbers coated CSH with different TPI and CPB concentrations, compared to our previous calculations on epoxy coated CSH. All structures are relaxed and the corresponding total energy within time are given in Fig. 6.5 as well. We note that the top of views presented in Fig. 6.5 are plotted using the VDW radii of atoms [118, 126] for determining the coating percentage, which is simply calculated from the pixels ratio between colors. The obtained results are listed in Table 6.1 as well as the initial parameters of the different coating materials. It can be seen from Table 6.1 that the coating percentage of TPI is increasing with increasing the weight percentage of coating materials. Moreover, comparing the different weight percentages (18.96% TPI coating 16.86% of CPB coating and 19.07 % of epoxy resins), it is concluded that CPB coating has a comparable coating capability with less weight percentage of the coating material.

Table 6.1

Initial density, weight percentage and coating percentage of different coating materials.

Coating materials	Initial density (g/cm3)	Experimental density (g/cm3)	Weight percentage (%)	Coating percentage (%)
TPI	0.889	0.890[131, 132]	20.33	98.05
TPI	0.892		18.96	97.53
CPB	0.900	0.900[133, 134]	16.86	97.18
Epoxy with MPD	1.132	1.111-1.142	19.07	96.95

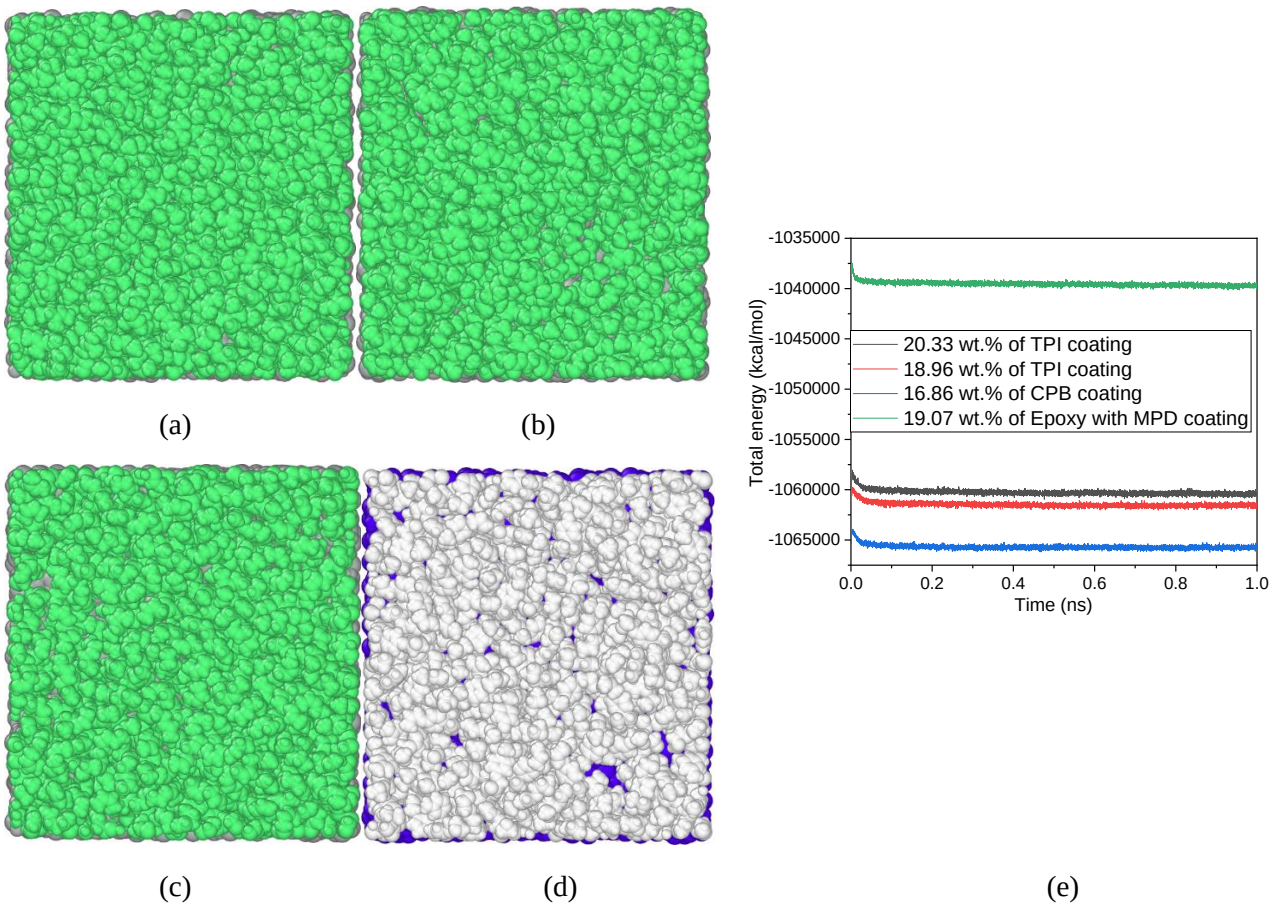

Fig. 6.5. Top view of 20.33 wt% of TPI coating surface (a), 18.96 wt% of TPI coating surface (b), 16.86 wt% of CPB coating surface (c), 19.07 wt% of Epoxy and MPD coating surface (d). The variation of the total energy of coated CSH models with time (e). The green color and gray color represent the rubber coating and the CSH in the rubber coated model, respectively, and the white color and blue color represent the epoxy coating and the CSH in the epoxy coated model, respectively. (For interpretation of the references to color in this figure legend, the reader is referred to the web version of this article.)

In Fig. 6.6, it is plotted the density profile of rubber and epoxy nanocoating model for comparison taken from our previous work [18]. It is observed from the density profile that rubber coating curves are inthe range of 4 Å to 15 Å away from CSH surface, much bigger than the one of epoxy coating estimated from 5 Å to 11 Å. In addition, TPI coating curve with a concentration of 20.33% has the best coating efficiency since it has the largest peak from 4 Å to 15 Å.

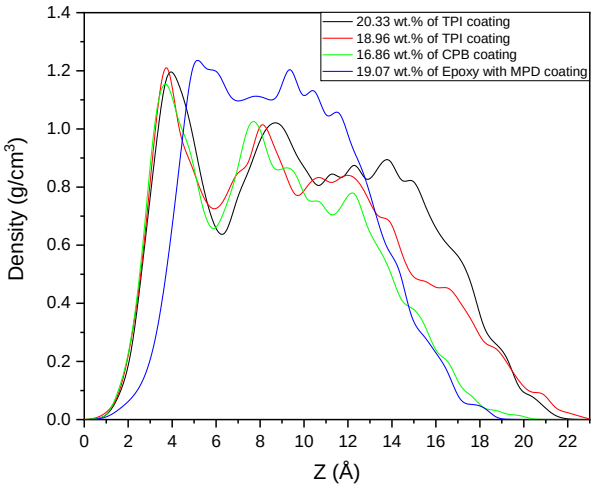

Fig. 6.6. Mass density profile of coatings of coated CSH film models.

The (001) free surface energy of rubber coated CSH models is evaluated by following Eq. (6.1). This method has been utilized by many previous researchers for estimating the free surface energy [17, 104-106].

$$\gamma_s = \frac{E_{coated\_film} - E_{coated\_bulk}}{2A} \quad (6.1)$$

Where γ_s is the free surface energy of the coated structure, E_{coated_film} and E_{coated_bulk} are the total energy of the coated film structure and the coated bulk model, respectively. A is the free surface area. Results of the free surface energy of the three models are listed in Table 6.2 and compared with other studies. It can be noticed that the surface energy of rubber coated CSH models are similar to epoxy coated CSH structure and decrease drastically from the range of 698–740 mJ/m^2 to 46.3–48.4 mJ/m^2. In addition, our findings are in a good agreement with experimental investigations [11, 12, 60].

Table 6.2

Surface energy of CSH with or without coating compared with available experimental results.

Models	Surface energy (mJ/m^2)	
	Theoretical	Experimental
TPI coated CSH	46.3-48.4	-
CPB coated CSH	40.8	-
Epoxy with MPD coated CSH	33.7-45.5[18]	28.2-53.1[60]
CSH without coating	698-740[17]	657-1750[11, 12]

To have a deep analysis about the interatomic interaction between rubber constituents and CSH surface atoms, we have calculated the radial distribution function (RDF), also called g(r), and correlation coordination values. In Fig. 6.7, the partial cao pair correlation functions and the corresponding coordination number are presented for the relaxed rubber coated CSH models. The cao is the calcium atom at the CSH surface; c3 is the Sp3 carbon atom in methyl group, c2 is the Sp3 carbon atom boned to two hydrogen atoms and c = is the non-aromatic end doubly bonded carbon atom; h is the hydrogen atom boned to carbon atom. Fig. 6.7 shows that the partial cao pair interactions among rubber coated CSH models have no big difference. For instance, in CPB coated CSH structure, it can be found that the first bond length of cao-c2 pair is 3.90 Å with a coordination number of 0.12, for cao-c = and cao-c3 pairs, its first bond length are 3.15 Å and 3.85 Å with a coordination numbers of 0.06 and 0.03, respectively. For cao-h pair interaction, it has the first bond length of 3.45 Å with a coordination number of 0.39.

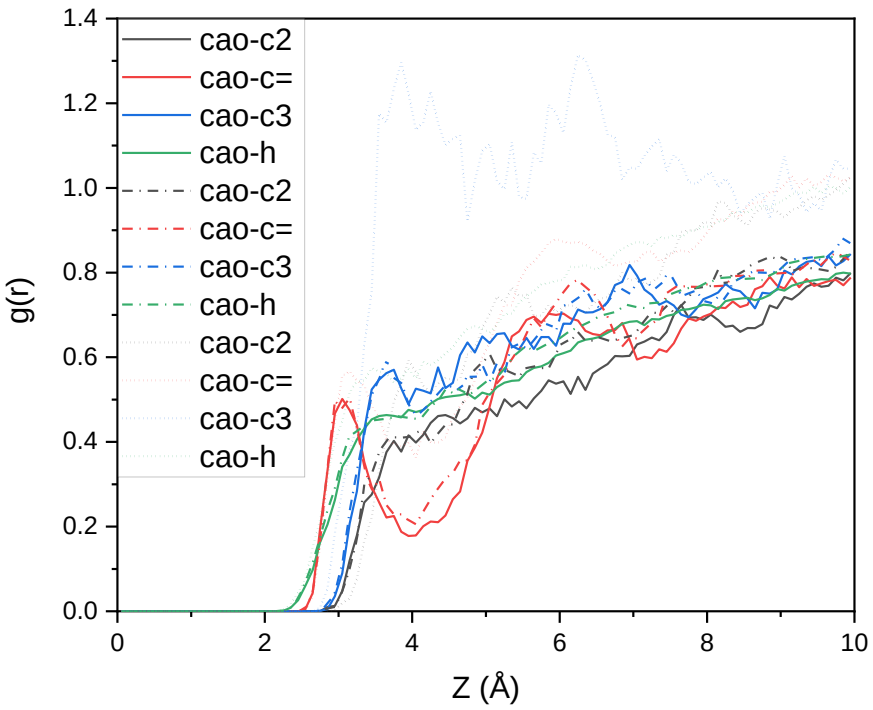

(a)

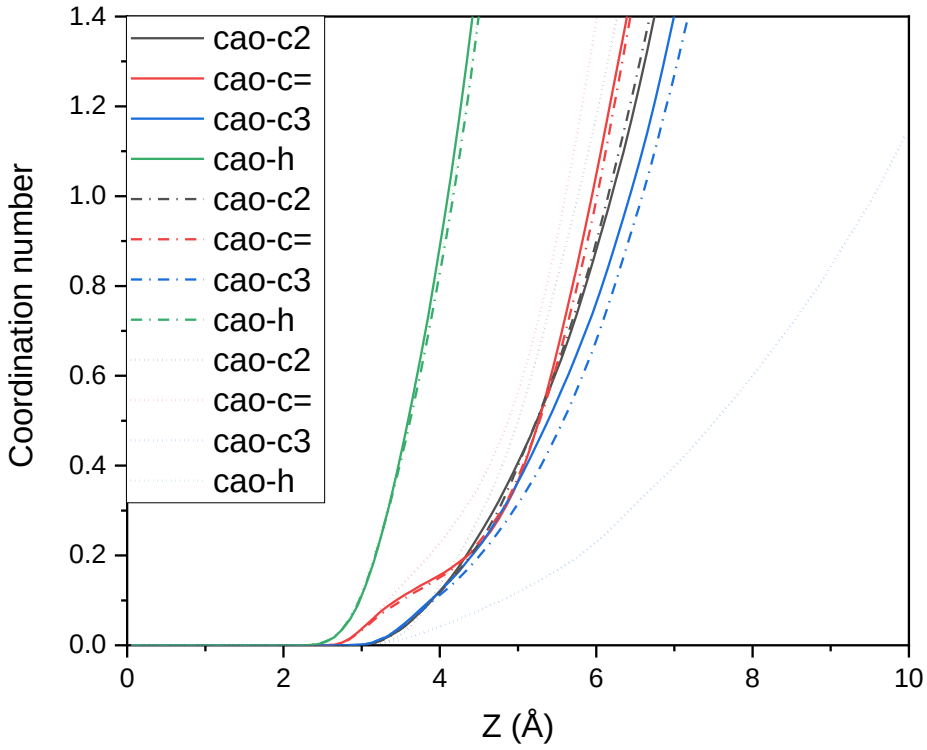

(b)

Fig. 6.7. Radial distribution function (RDF) of coated CSH film models (a), and the coordination number corresponding to each pair of RDF (b). Solid line and dash dot line are the 20.33 wt% and 18.96 wt% of TPI coated model, respectively, the dot line is 16.86 wt% of CPB coated model.

All the results of cao pair correlation functions are listed in Table 6.3. It is noticed that the first ionic bond between coating and CSH surface is cao-c = pairs. Besides, the coordination number of each pair hydrogen atom is easier accommodated onto the negatively charged oxide calcium surface due to its highest coordination number value. Therefore, our results conclude that the structure of –CH= (non-aromatic end doubly bonded carbon atom with one free hydrogen atom) is easier to adsorb onto the (001) CSH surface.

Table 6.3

The first bond length and the coordination number in that distance for partial cao pairs of coated CSH film models.

	20.33 wt.% of TPI		18.96 wt.% of TPI		16.86 wt.% of CPB	
	Bond (Å)	CdN	Bond (Å)	CdN	Bond (Å)	CdN
cao-c2	3.75	0.07	3.85	0.09	3.90	0.12
cao-c=	3.05	0.05	2.95	0.03	3.15	0.06
cao-c3	3.75	0.08	3.65	0.06	3.85	0.03
cao-h	3.63	0.53	3.85	0.70	3.45	0.39

6.3.2. Hydrophobic surface of rubber coated CSH nanostructure

The hydrophobicity of rubber coated CSH is investigated from the well relaxed rubber coated CSH-Nanodroplet models by evaluating the contact angle between water nanodroplet and rubber coated CSH surface. The schematic of estimating the contact angle as given in Fig. 6.8, which has been utilized by lots of previous investigations [17, 112, 113].

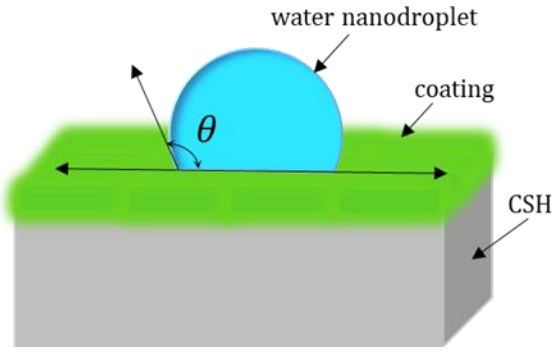

Fig. 6.8. Schematic of the contact angle (θ) between water nanodroplet and coated CSH surface from the perspective of view.

It can be seen from Fig. 6.3 that the total energy of CPB coated CSH-Nanodroplet structure is converged after 2 ns. It is the same situation for the other. To get a clear picture about the dynamical wetting of the nanodroplet on the CSH nanocoated surface, Fig. 6.9 illustrates the atomic configurations of the evolution of water nanodroplet onto the coated CSH surface (with rubber and epoxy) from the initial to the well equilibrated state (0 ns to 2 ns). It is observed that coatings have the good capability of preventing water adsorbed onto CSH surface. At 0.5 ns, the nanodroplet is

on the top of the surface and remains equilibrated until 2 ns. The averaged contact angles between relaxed nanodroplet and rubber coated CSH are determined from the last 0.5 ns configurations. To this end, we have extracted the atomistic positions of the equilibrated models then they were represented in Cartesian coordinates. The contact angle is deduced from the appropriate tangent of the nanodroplet on the coating surface.

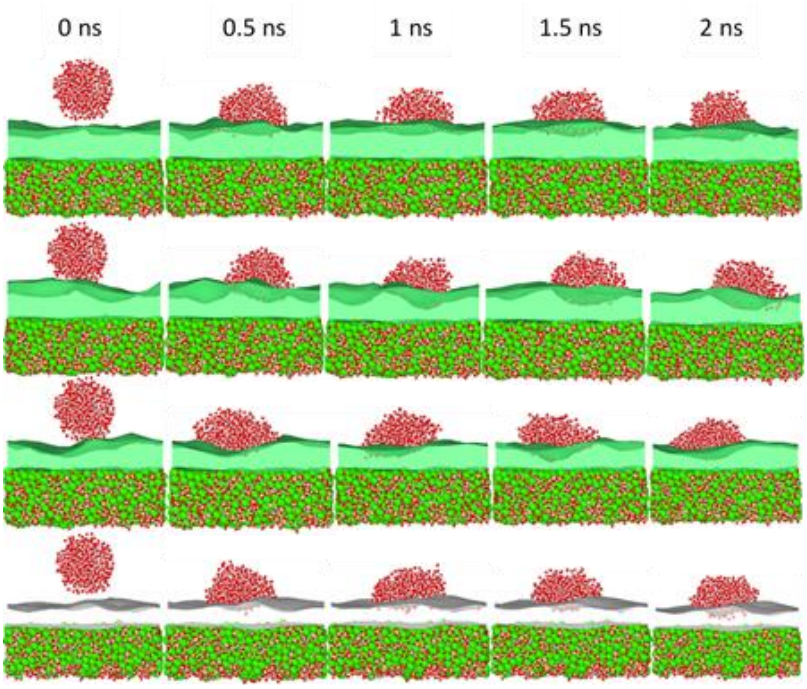

Fig. 6.9. From top to bottom are the left of view of coated CSH-Nanodroplet models corresponding the structure of (a), (b), (c) and (d) of Figs. 5 to 0 ns, 0.5 ns, 1 ns, 1.5 ns and 2 ns stage.

Table 6.4

Averaged contact angles between water nanodroplet and rubber coated CSH compared with available theoretical and experimental results [10].

Method	Coating surface (wt. %)	Contact angle (°)			
		Front of view		Left of view	
		left side	right side	left side	right side
Theoretical	20.33 of trans-Polyisoprenes	96.42	96.09	98.11	93.40
	18.96 of trans-Polyisoprenes	97.60	93.44	93.93	95.60
	16.86 of cis-Polybutadienes	93.55	94.98	97.61	92.85
	19.07 of Epoxy with MPD	84.29-91.97			
Experimental	Without coating	23.62-29.29			
	Functionalized Polybutadienes	87.3-105.8			

In this work, the contact angle was determined from left of view, as listed in Table 6.4, compared with available theoretical and experimental studies [10]. Our results show that the obtained contact angle for all models is around four times when rubber is coating CSH surface. Therefore, it reduces the water impermeability for times than pristine CSH surface, making CSH surface hydrophobic, as found experimentally. To dig more understanding of the coating capability between rubber coating and epoxy coating, we investigated the variation of density profile of water nanodroplet for a non-coated and coated CSH surface along the Z-direction, as presented in Fig. 6.10. First, it is observed that both rubber and epoxy coating are able to prevent water adsorbed onto CSH surface, since the mass density of water nanodroplet has a large peak expanded along Z-direction from 11 Å to 22 Å. It is also shown that in the case of CPB coated CSH model with 16.86 wt%, the curve is sharper than the others, which explain the lower obtained value of the contact angle, as presented in Table 6.4.

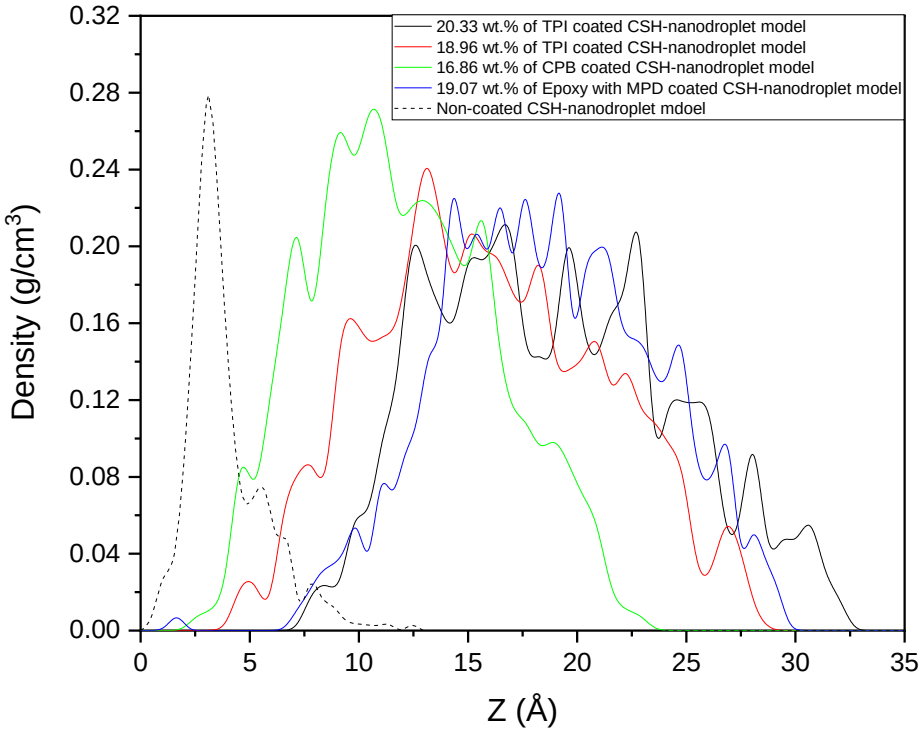

Fig. 6.10. Mass density profile of water nanodroplet onto coated and non-coated CSH structures.

Regarding the density curve of epoxy coating, a small peak is found roughly at 1.5 Å away from CSH surface, which indicates that epoxy coating is permeable than rubber. Regarding the non-coated CSH surface, a sharp peak clearly appeared around 2.5 Å, confirming the presence of water into CSH substrate. In the top of view of the coated CSH nanodroplet models, as shown in Fig. 6.11, it is noticed that the nanodroplet onto epoxy coated CSH has the most irregular shape. In the case of 20.33 wt% of TPI coated CSH, the top of view of nanodroplet is being like an imperfect circle shape.

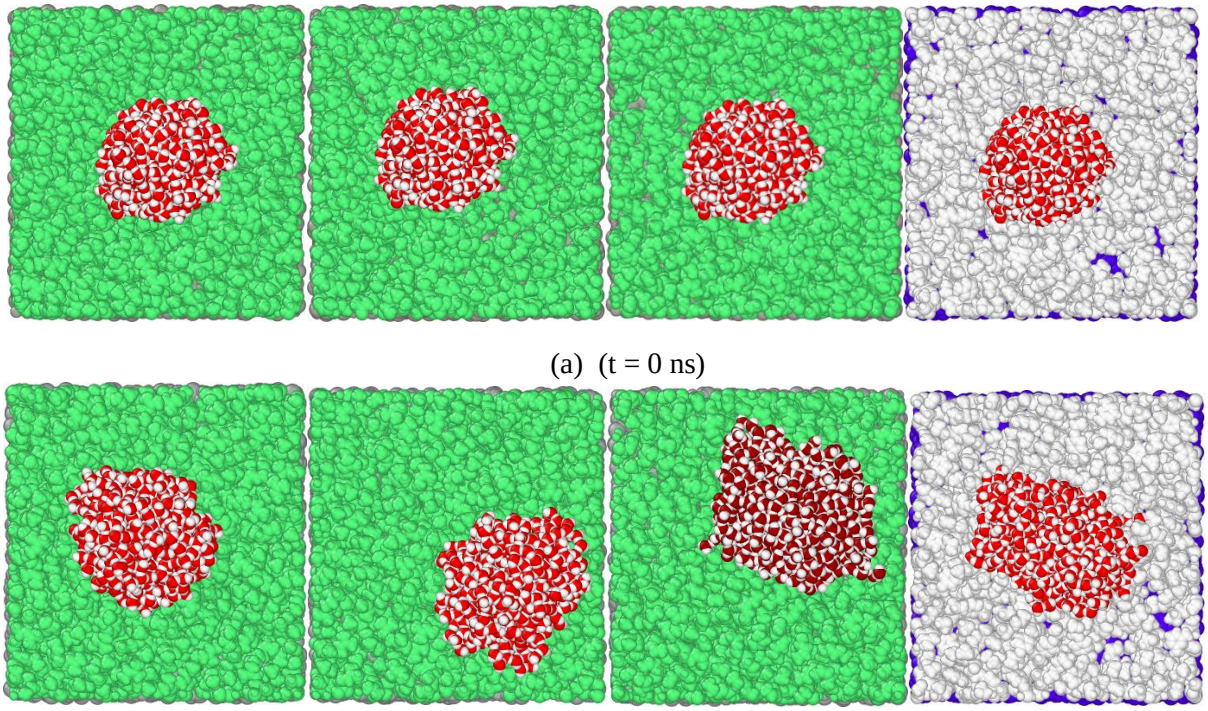

(a) (t = 0 ns)

(b) (t = 2 ns)

Fig. 6.11. (a) From left to right are the top of view of the initial nanodroplet onto coated CSH configurations, which corresponds to the structures (a), (b), (c) and (d) from Fig. 6.5. (b) The well relaxed nanodroplet onto coated CSH models corresponding to each initial structure (b).

To follow the mobility and the diffusion of water nanodroplet onto the coated CSH surface, we have investigated the variation of the Mean Squared Displacement (MSD) and the diffusion coefficient with time. Fig. 6.12.a shows that MSD is increasing sharply at the beginning then gradually slowly with time. The corresponding diffusion coefficient D is decreasing sharply at the beginning of the simulation then changing slightly with time. The inserted figures in Fig. 6.12.a

are the last 50 ps data of MSD and D, respectively. It is shown that both MSD and D of nanodroplet are changing slightly than it in the model of CSH without coating. In addition, we investigated the evolution of both MSD and D of the coating with time from the coated CSH-Nanodroplet models. The obtained diffusion coefficient of water nanodroplet and coated film are listed in Table 6.5 compared with our previous work [17].

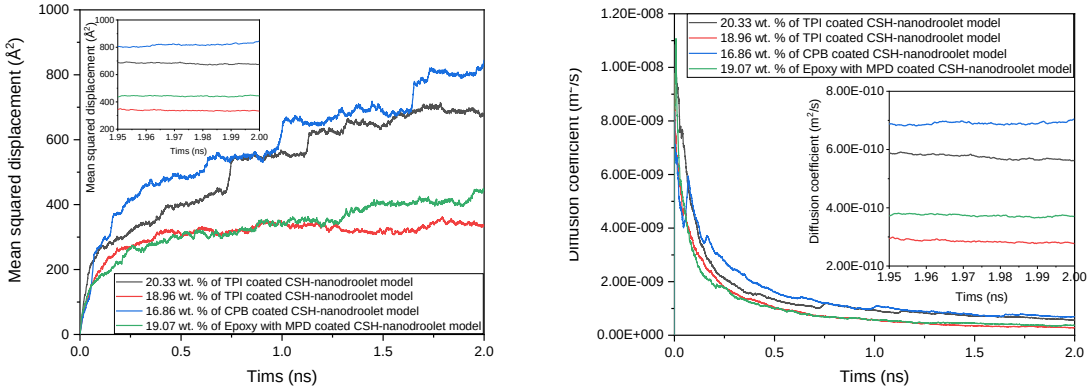

(a)

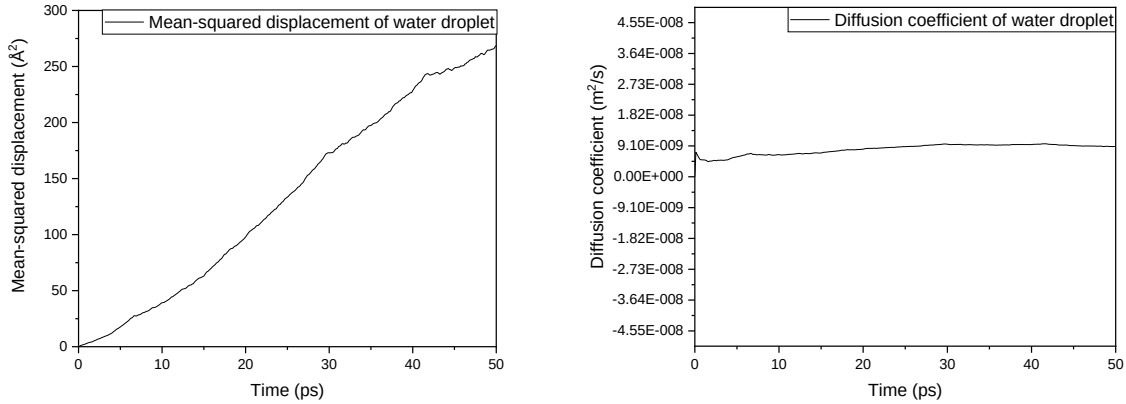

(b)

Fig. 6.12. Mean squared displacement and diffusion coefficient of nanodroplet from coated CSH-Nanodroplet models (a), from CSH-Nanodroplet model (b).

Finally, the water molecules interaction with rubber film atoms is investigated via the calculation of the partial pair correlation and the coordination number. In Fig. 6.13, the partial ospc pair

correlation functions from the equilibrated coated CSH-Nanodroplet models is presented as well as the coordination number.

Table 6.5

Averaged diffusion coefficients either of the coating or of the nanodroplet from different models.

Models	Coating materials	Diffusion coefficient (m^2/s)	
		Coating surface	Droplet
Coated CSH film models	20.33 wt.% of TPI	1.75×10^{-10}	-
	18.96 wt.% of TPI	1.87×10^{-10}	-
	16.86 wt.% of CPB	1.81×10^{-10}	-
	19.07 wt.% of Epoxy with MPD	1.22×10^{-10}	-
Coated CSH-nanodroplet models	20.33 wt.% of TPI	3.23×10^{-11}	5.75×10^{-10}
	18.96 wt.% of TPI	2.97×10^{-11}	2.85×10^{-10}
	16.86 wt.% of CPB	3.26×10^{-11}	6.90×10^{-10}
	19.07 wt.% of Epoxy with MPD	4.83×10^{-12}	3.74×10^{-10}
CSH-nanodroplet model	-	-	9.05×10^{-9}

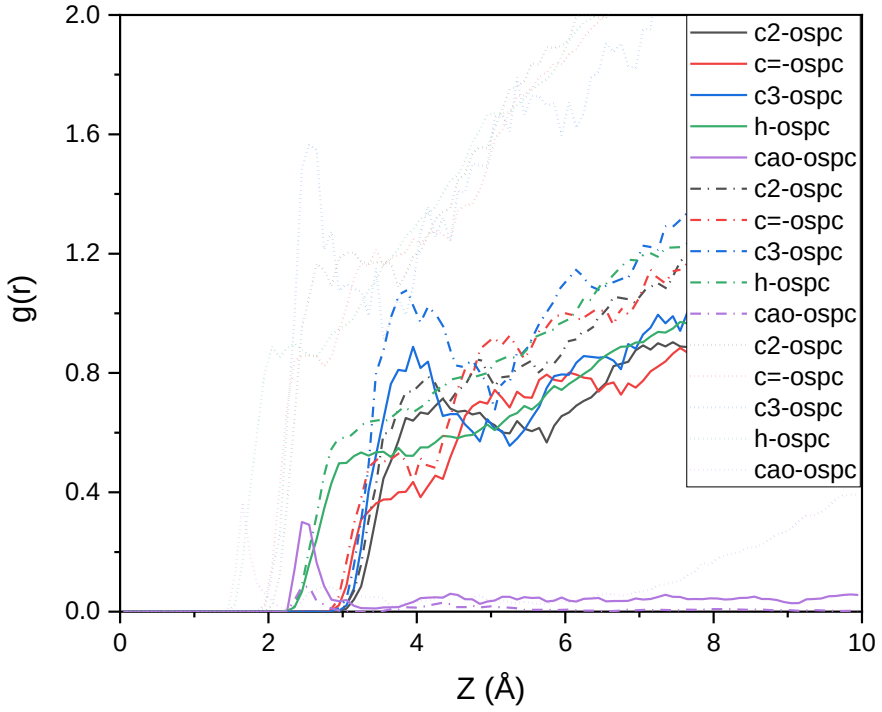

(a)

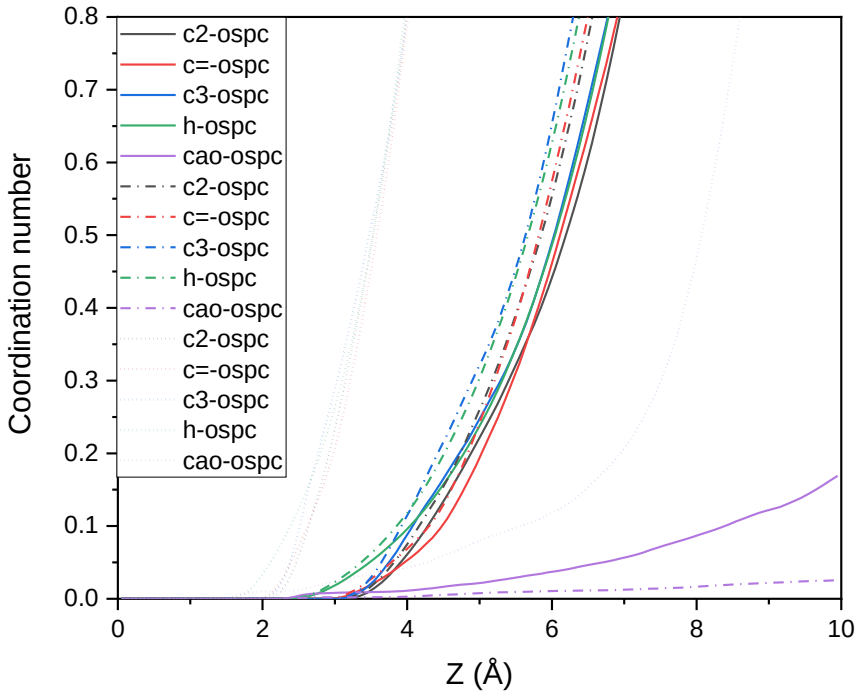

(b)

Fig. 6.13. Partial ospc pair correlation functions of coated CSH-nanodroplet models (a), and the coordination number corresponding to each pair of correlation functions (b).

The ospc is the oxygen atom in water nanodroplet. It can be seen that the RDF of ospc pair interactions have no big difference for the rubber coated CSH-Nanodroplet models. For instance, in CPB coated CSH-Nanodroplet model, the first bond length of c2-ospc pair is 2.65 Å with a coordination number of 0.10; while for c = -ospc and c3-ospc pairs, the first bond lengths are both located at 2.55 Å with coordination numbers of 0.09 and 0.12, respectively. For h-ospc and cao-ospc pairs, they have the first bond lengths of 2.05 Å and 1.65 Å with a coordination number of 0.05 and 0, respectively. All results of partial ospc pair interactions are presented in Table 6.6.

Table 6.6

First bond length and the coordination number in that distance for partial ospc pairs of coated CSH-nanodroplet models.

	20.33 wt.% of TPI		18.96 wt.% of TPI		16.86 wt.% of CPB	
	Bond (Å)	CdN	Bond (Å)	CdN	Bond (Å)	CdN
c2-ospc	4.35	0.11	4.15	0.09	2.65	0.10
c=-ospc	3.90	0.05	3.75	0.04	2.55	0.09
c3-ospc	3.90	0.08	3.85	0.10	2.55	0.12
h-ospc	3.25	0.04	3.25	0.04	2.05	0.05
cao-ospc	2.50	0.00	2.50	0.00	1.65	0.00

6.3.3. Interfacial adhesion between rubber film and CSH surface

To investigate the work of adhesion between rubber coating and CSH, we have employed two methods. In the first method, the interaction energy between coating and CSH is calculated in the conditions either with or without water nanodroplet, then the work of adhesion is determined as following Eq. (6.2):

$$w_{ad} = \frac{-E_{interaction}}{2A} = \frac{-(E_{pairwise}+E_{long\_coul})}{2A} \quad (6.2)$$

Where w_{ad} is the work of adhesion, the $E_{interaction}$ is the interaction energy between coating and CSH, the $E_{pairwise}$ is the pairwise energy, E_{long_coul} is the long-range coulombic energy, A is the interface area between coating and CSH surface. The second method was using the interfacial models to determine the work of adhesion as following the Eq. (6.3):

$$w_{ad} = \frac{(E_{film\_rubber}+E_{film\_CSH})-E_{interfacial}}{2A} \quad (6.3)$$

Where E_{film_rubber} and E_{film_CSH} are the total energy of rubber film and CSH film models, respectively. $E_{interfacial}$ is the total energy of interfacial models, A is the interface area between rubber film and CSH film. All results of the work of adhesion between coating and CSH estimated from the two methods as given in Table 6.7. The obtained values between rubber coating and CSH are in the range of 49.42 mJ /m^2 to 92.76 mJ/m^2. They are found in a good agreement with the

experimental investigation [6]. Nevertheless, the evaluated values of work of adhesion from method one is smaller than the values estimated from method two. The work of adhesion between rubber coating and CSH in the condition of the rubber coating being sandwiched between nanodroplet and CSH is bigger than under the condition without nanodroplet. However, for the epoxy coated CSH models, we noted opposite results what means the work of adhesion between epoxy coating and CSH is reduced while epoxy coating being sandwiched between nanodroplet and CSH.

Table 6.7

Work of adhesion between coating and CSH with or without nanodroplet compared with available experimental results [6].

Models	Coating materials	work of adhesion (mJ/m^2)		
		Theoretical		Experiment
		Method 1	Method 2	
Coated CSH films models	20.33 wt.% of TPI	53.09	76.60	-
	18.96 wt.% of TPI	49.42		
	16.86 wt.% of CPB	56.71	92.76	
	19.07 wt.% of Epoxy with MPD	89.56	102.81	90.17-102.79
Coated CSH-nanodroplet models	20.33 wt.% of TPI	54.82	-	-
	18.96 wt.% of TPI	56.16		
	16.86 wt.% of CPB	64.45		
	19.07 wt.% of Epoxy with MPD	86.19		

6.4. Conclusions

In this work, the hydrophobicity of the rubber coated CSH surface and the work of adhesion between coating and CSH has been evaluated by the means of Molecular Dynamics simulations. A realistic CSH model and a confined layer of rubber model are utilized to represent the atomistic model of the rubber coated CSH. The interatomic interactions have been described using the combination of CLAYFF and CVFF force fileds. Results show that the coating capability of TPI is better than CPI as well as CPB is better than TPB. The rubber coated CSH surface energy jumps up from the range of 698–740 mJ/m^2 to 40.8 mJ/m^2 to 48.4 mJ/m^2. The obtained contact angle is four times higher than the CSH surface, estimated between 92.85° and 98.11°, in agreement with experimental data. This important result proves the hydrophobicity behavior of rubber coated CSH nanostructure. Finally, the calculated work of adhesion between rubber coating and CSH surface is found in the range of 49.42 mJ/m^2 to 92.76 mJ/m^2.

Chapter 7:

Theoretical investigation of prohibiting water and chloridion infiltration into cement paste through a rubber nano-coating

7.1. Introduction

Under aggressive condition, either the interfacial deterioration behind mechanism in organic-coating/CSH or how a success impermeable coated cement paste performed is not understood at atomistic level. Since the experimental observation technical limits, there is a critical need to do the unsolved investigations, at nano-scale level, by means of molecular dynamics simulations. It enhances us the possibility to understand, what significant interfacial interatomic bond interactions in organic-coating/cement-paste are responsible to against the aggressive environment. Furthermore, the behind mechanisms, at nano-scale level, of how is a success impermeable organic coating performed under severe condition and what are remarkable properties responsible for making the impermeable performance could be revealed. Therefore, in the present work, our aim is, at atomistic level, under either salty water solution condition (4 wt. % of NaCl) or pure water solution condition, first investigate the interfacial bond degradation in the interface of organic-coating/CSH, further, study what properties of an effective coating result in helping cement paste survived. To this end, two types of coated CSH model [18, 19] based on a developed Pellenq et al. [24] realistic model are employed. One is fully or non-fully epoxy resins (diglycidyl ether of bisphenol A with *m*-phenylenediamine) coated CSH model and the other one is fully rubber (1,4-cis-Polybutadiene) coated CSH model. Under the severe conditions, we firstly investigate the whole detachment process between non-fully epoxy coating and CSH, then we investigated the effect of small pore structure in the coating surface and coating thickness distribution along CSH surface to the fully coating impermeable performance.

7.2. Modeling and simulation details

7.2.1 Models construction

To represent coating CSH model exposed in severe environment at nano-scale level, a developed realistic CSH model of Pellenq et al. [24] with a new Ca/Si ratio of 1.64 is used in this work. More details of constructing a realistic model could be found in the following investigations [24, 27, 29]. Moreover, the nano-coating process is detailed in our previous studies [18, 19], which is simply done by putting a confined layer of amorphous cell of coating materials onto a well relaxed CSH (001) surface varying the weight content of coating materials until CSH being ideal coated. Subsequently, we simply put well relaxed coating CSH under either pure water solution condition or salty water solution condition. Furthermore, since the deterioration process in the interface of

organic-coating/CSH under aggressive condition is slow, thus partial epoxy coated CSH model is constructed in order to study the whole detachment process between coating and CSH. Nevertheless, both fully epoxy coated CSH model and fully rubber coated CSH model are constructed to seek the possibility that coating could make CSH impermeable under severe environment. Hence, 6 models have been constructed in this work, for instance, the structure of fully rubber coated CSH under salty water solution condition (a = 68.652 Å, b = 73.353 Å, c = 129.100 Å, $\alpha = \beta = \gamma = 90.00°$) containing 39,380 atoms is given in Fig. 7.1, and the variation of the total energy in time is presented as well. In this case, the vacuum added along Z direction is about 30 Å, the minimum distance between salty water solution and coated CSH is 0.890 Å.

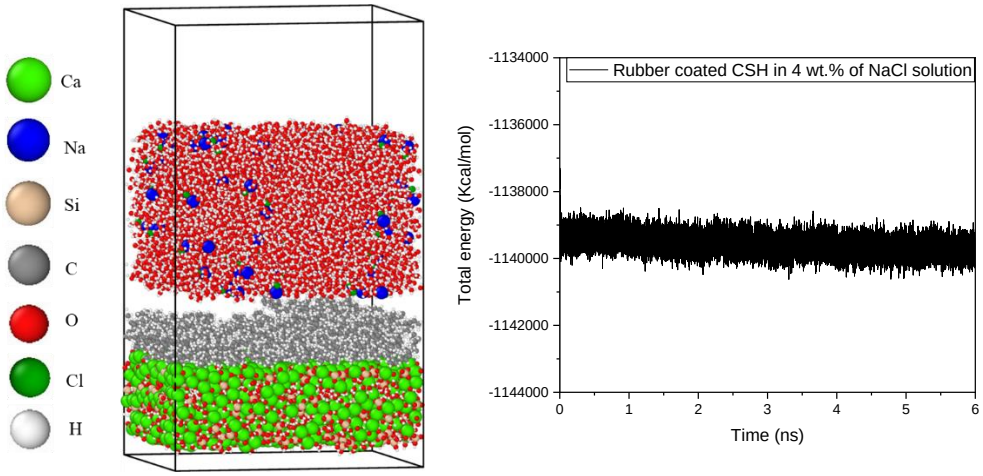

(a) (b)

Fig. 7.1. The perspective view of rubber coated CSH under 4 wt. % of NaCl solution condition at t = 0 ns (a), the variation of the total energy in time (b).

7.2.2 Force field and simulation details

In this work, a combination method of the general force field [89] (CLAYFF) and the consistent-valence force field [88] (CVFF) are utilized for simulating the interactions among atoms. Additionally, the CLAYFF force field is used to describe the interactions among CSH atoms, and solution (pure water solution and salty water solution) atoms are simulated using CLAYFF potential as well. It is based on the single point charge [119] (SPC) water potential, divide the system energy into a series of partial energy: van der Waals energy, Coulombic energy, harmonic

bond energy and harmonic angle energy. Furthermore, the CVFF force field is utilized to simulate the interactions among epoxy's (or rubber's) atoms. Besides the 4 types energy introduced in CLAYFF potential, there are another 2 types energy contributed to its total energy, which are the harmonic dihedral energy and the improper energy as given in CVFF potential. Nevertheless, The interactions in the interfaces of CSH/epoxy(rubber), CSH/Solution and Solution/epoxy(rubber) are simulated following Lorentz-Berthelot rules [102].

Molecular dynamics simulations are performed via Large-scale Atomic/Molecular Massively Parallel Simulator [103] (LAMMPS). Periodic boundary conditions are applied to X, Y and Z directions during the simulation process. The equation of motion is integrated using Verlet algorithm [120] with a timestep of 0.25 fs. The Van der waals interactions and the Coulombic electrostatic interactions are truncated using a cutoff of 10 Å. Moreover, a particle-particle particle-mesh (pppm) method [121] is used to estimate the long-range Coulombic interactions or long-range $1/r^6$ interactions with an accuracy value of 1.0e-4 [122]. All models are firstly energy minimized using the conjugate gradient (cg) algorithm to optimize the structure, then the simulations are performed to equilibrate the models under canonical (NVT) ensemble [107] using Nose-Hoover thermostat at T = 300 K. To probe the degradation process between coating and CSH, thus the partial epoxy coated CSH model under aggressive environment (either pure water solution condition or salty water solution condition) are simulated for 8 ns to study the bonding fracture in the interface. Further, fully coated (rubber and epoxy) CSH models are equilibrating for 6 ns to seek the potential of making CSH impermeable under the aggressive condition.

7.3. Results and discussion

7.3.1 Detachment process

We first investigated the behind mechanism of bonding deterioration in the interface between coating and CSH under aggressive environment. The variation of the total energy of the partial coated CSH model under severe condition in time is given in Fig. 7.2, the insert figures are the last 1 ns for two cases, which indicates the total energy is converged.

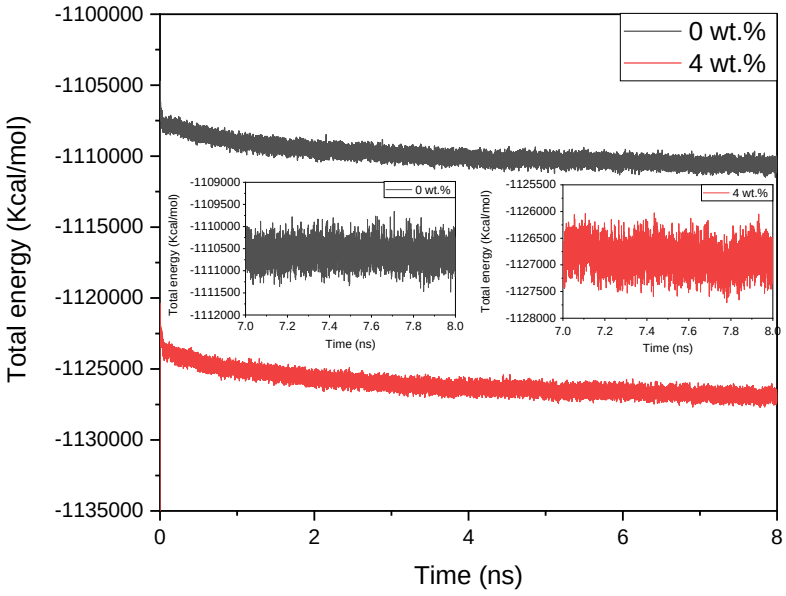

Fig. 7.2. The variation of the total energy of partial epoxy coated CSH under different wt. % of NaCl condition in time.

To have a clear view of the detachment process between coating and CSH within time, the front of view, the left of view and the top of view of the corresponding equilibrated configuration at different stages are presented in Fig. 7.3. to Fig. 7.5. Fig. 7.3 and Fig. 7.4 both show that non-fully epoxy coating will be fully detached after 8 ns in two cases. Moreover, the front of view indicates that the epoxy coating would be more distorted under salty condition than in pure water condition, the top of view shows that the size of pore structure would increase within time for the two cases.

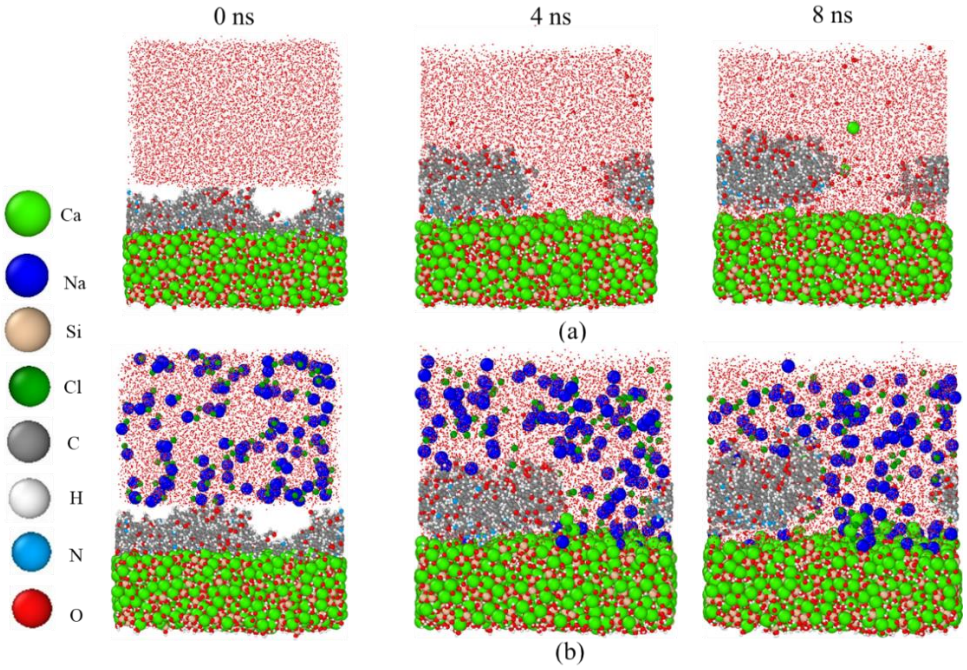

Fig. 7.3. The front view of partial epoxy coated CSH under pure water solution within time (a), and under salty water solution (b).

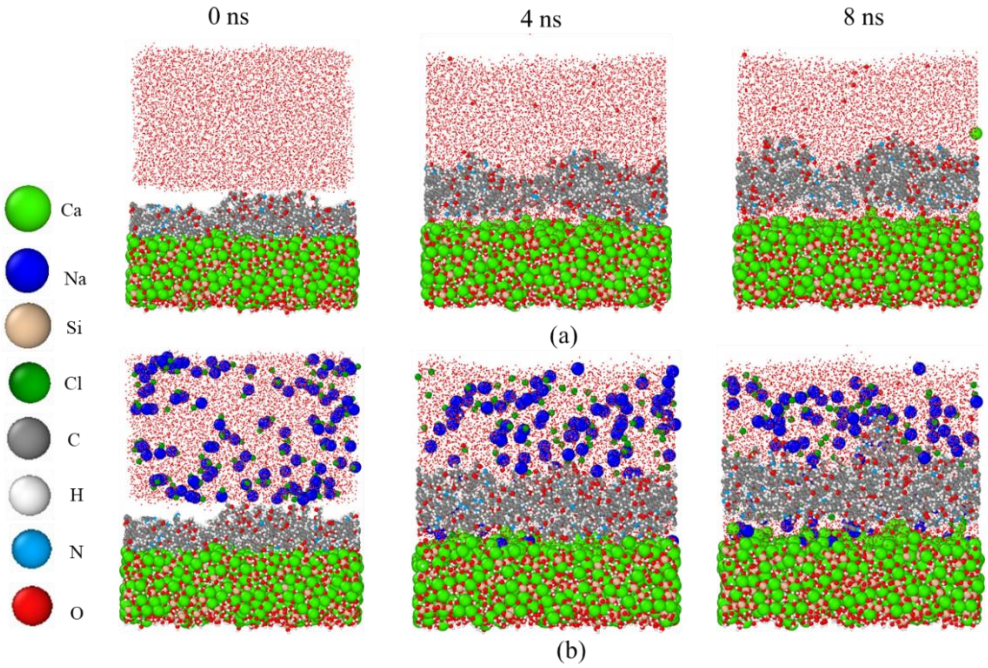

Fig. 7.4. The left view of partial epoxy coated CSH under pure water solution within time (a), and under salty water solution (b).

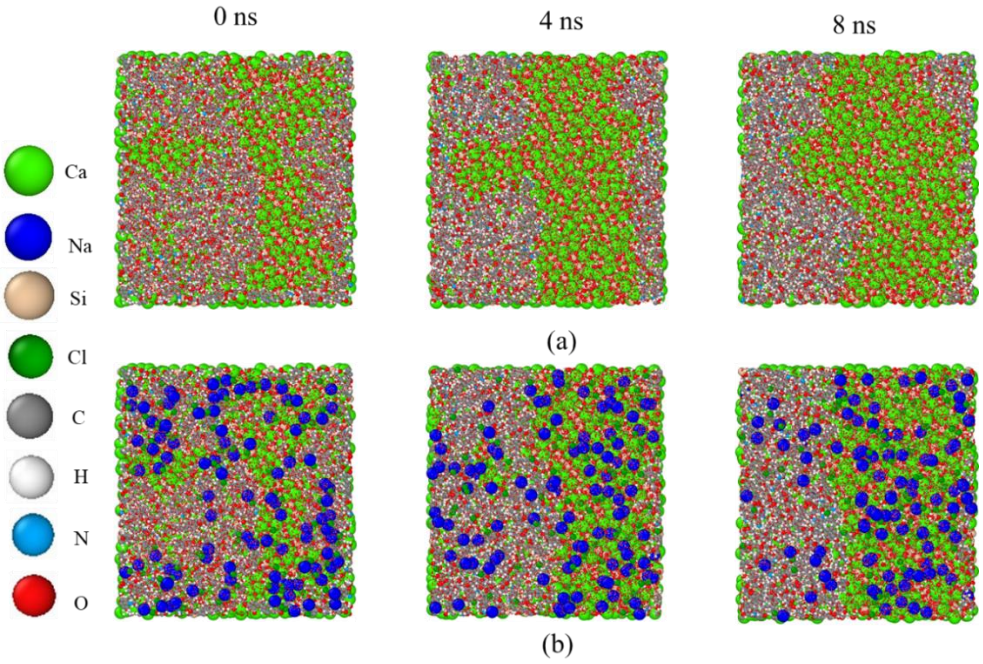

Fig. 7.5. The top view of partial epoxy coated CSH under pure water solution within time (a), and under salty water solution (b).

To explore the behind inducement of why epoxy coating more distorted in salty water condition than in pure water condition during the detachment process, the radial distribution function (RDF), also called g(r), has been investigated. The partial correlation function of both Na~ pairs and Cl~ pairs are presented in Fig. 7.6. Na and Cl are sodium atom and chlorine atom, respectively, c2 and c3 are the Sp3 carbon atom boned two hydrogen atoms and the Sp3 carbon atom in methyl group, respectively. The hn is hydrogen atom bonded to nitrogen atom in MPD (*m*-phenylenediamine) molecules, cp is Sp2 aromatic carbon in partial double bonds carbon ring and o is oxygen atom. The first remarkable peak in all figures observed in Fig. 7.6 indicates that chloridion are responsible to attack coating thus making coating distorted. Moreover, cl-hn pairs has the smallest first bond distance around 2.8 Å, the rest are bigger than 4 Å. Further, the mass density profiles along Z direction of the two systems are studied as listed in Fig. 7.7. It shows three remarkable peaks in black line which indicates the layer structure of CSH corresponding to calcium-silicate sheets. In the range of 20 Å to 27.5 Å, it indicates the water infiltrated inside of CSH. The remarkable peaks in the ranges of 27.5 to 30 Å for blue line indicates a dense water layer formed between coating

and CSH which marking the fully detachment behavior. Furthermore, compared the blue and red line, it can be seen the detached epoxy coating reducing the density of water.

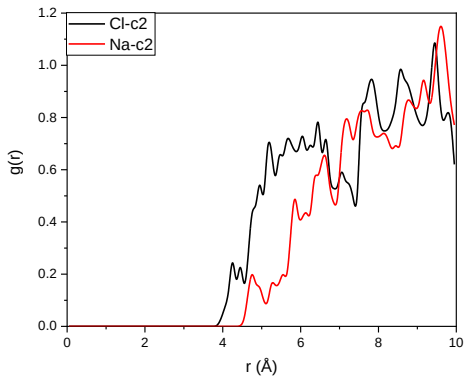

(a)

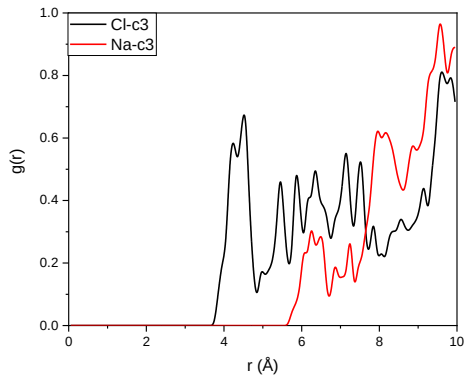

(b)

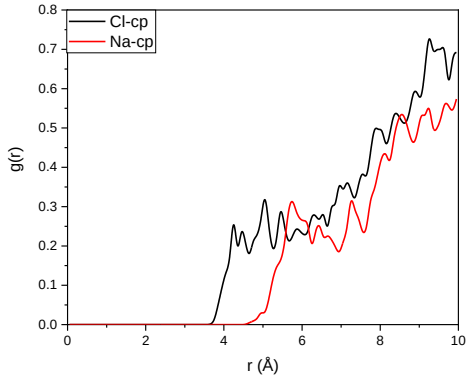

(c)

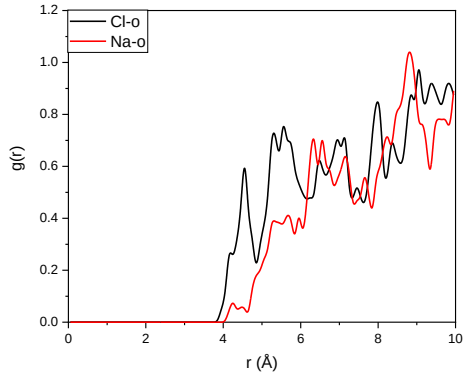

(d)

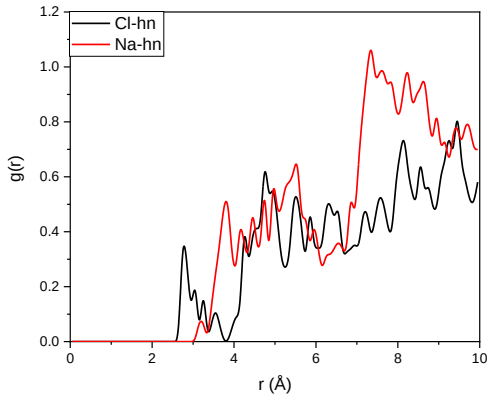

(e)

Fig. 7.6. The partial correlation function of partial epoxy coated CSH under salty water condition.

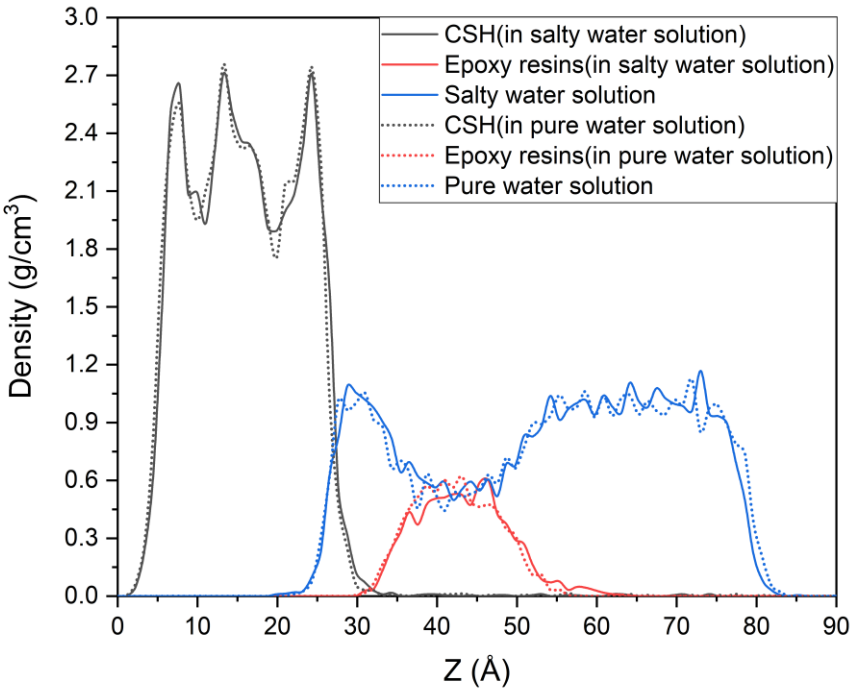

Fig. 7.7. Mass density profiles of the system of partial epoxy coated CSH under different solutions condition.

To probe deeper behind information of the detachment behavior under aggressive condition, the fracture energy between coating and CSH is investigated, the fracture energy is defined as following Eq. (7.1).

$$E_{fracture} = -E_{interaction} = -(E_{pairwise} + E_{long\_coul}) \quad (7.1)$$

Where $E_{fracture}$ and $E_{interaction}$ are the fracture energy and the interaction energy between coating and CSH, respectively. The $E_{pairwise}$ and E_{long_coul} are the pairwise energy and the long-range coulombic energy, respectively. Consequently, the variation of the fracture energy within time is given in Fig. 7.8. It shows that the fracture energy is decreasing with time corresponding to the detachment behavior, and the insert figure is the last 2 ns of the fracture energy, which indicates

it is converged. Additionally, it can be seen in the ranges of 1ns to 2ns that salty water has bigger power to reduce the fracture energy than water. To do a depth investigation of this behavior, the RDF and correlation coordination numbers of the structure under either pure water condition or salty water condition have been calculated in the interfacial region at different times. The results is given in Fig. 7.9 and Fig. 7.10. $Ca_{surface}$ is the calcium atom at CSH (001) surface, O_{epoxy} and N_{MPD} are oxygen atom in epoxy and nitrogen atom in MPD, respectively. The inserted g(r) figures in Fig. 7.9 and Fig. 7.10 are represented the structure at 4 ns, 6 ns and 8 ns stages. The results show quite different trend compared with the structure at 0ns and 2 ns in two conditions. Furthermore, the correlation coordination numbers of both $Ca_{surface}$-O_{epoxy} and $Ca_{surface}$-N_{MPD} indicate that its values are smaller in salty water solution condition than in pure water solution condition at 2 ns, which contributing to the less fracture energy observed in Fig. 7.8 in the range of 1 ns to 2 ns.

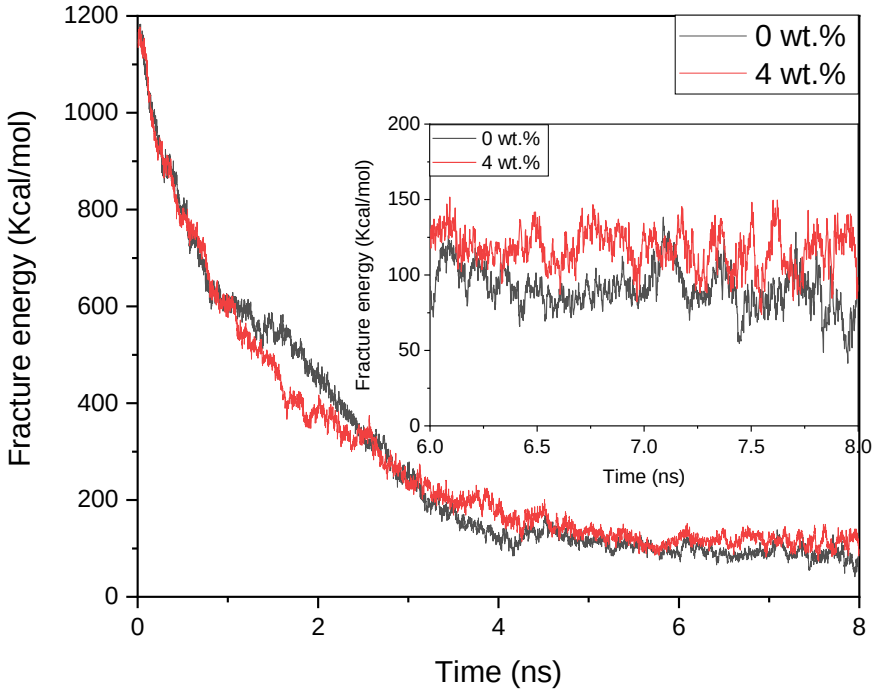

Fig. 7.8. The variation of the fracture energy of partial epoxy coated CSH under different wt. % of NaCl solution condition in time.

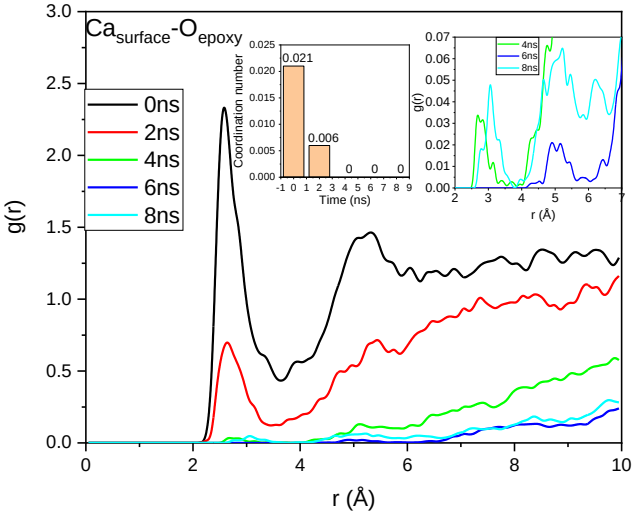

(a)

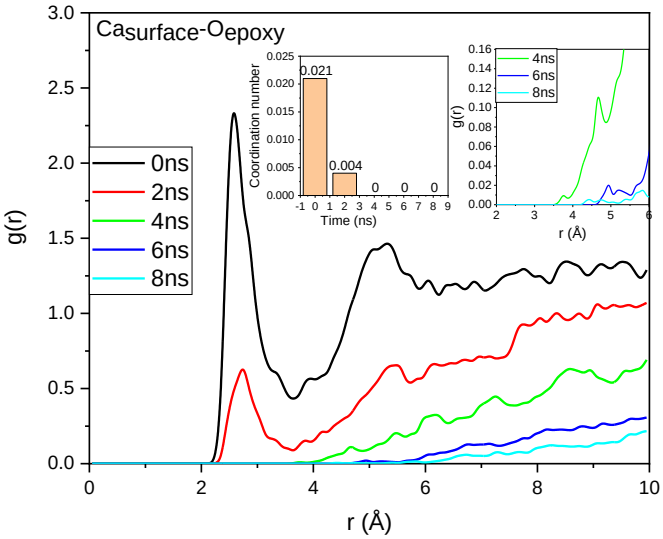

(b)

Fig. 7.9. The RDF and coordination number of $Ca_{surface}$-O_{epoxy} pair under pure water solution condition (a), and under salty water solution condition (b).

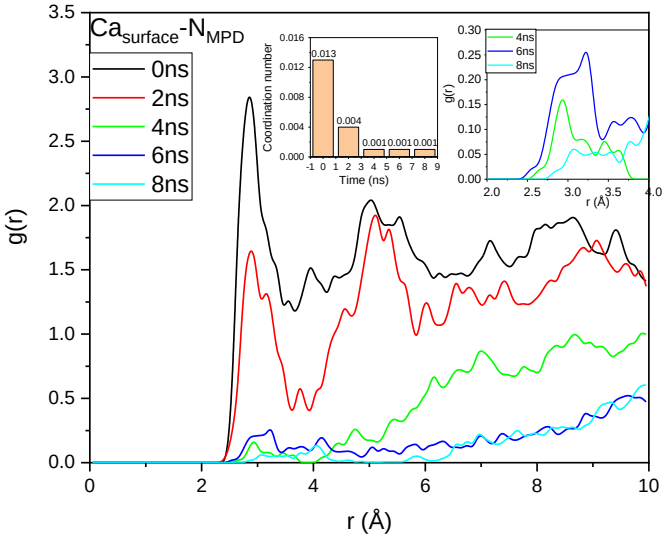

(a)

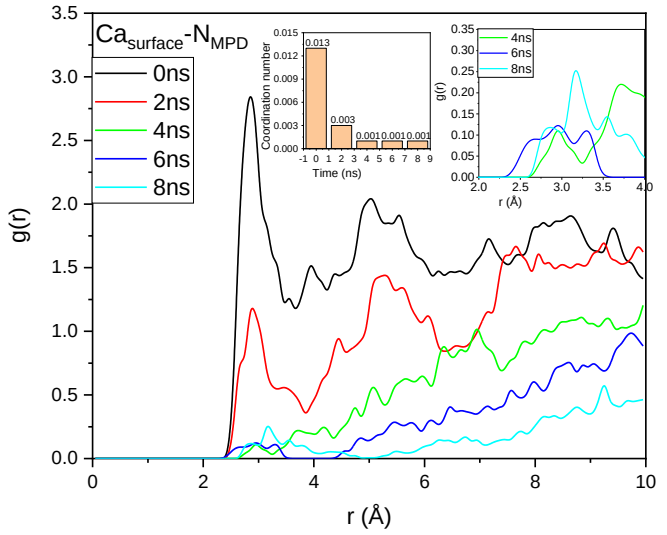

(b)

Fig. 7.10. The RDF and coordination number of $Ca_{surface}$-N_{MPD} pair under pure water solution condition (a), and under salty water solution condition (b).

To have more behind information contributing to the detachment behavior, the self-diffusion coefficient (D) of water and ions (Cl^- and Na^+) have been investigated either only in the solution or the solution being interacted with non-fully coated CSH. Its value is estimated from the standard relationship between D and the slop of its mean-squared displacement (MSD) as following Eq. (7.2).

$$D = \frac{1}{6}\frac{d}{dt}MSD(t) = \frac{1}{6}\frac{d}{dt}\langle|R_i(t) - R_i(0)|^2\rangle \quad (7.2)$$

Where $R_i(t)$ and $R_i(0)$ are the positions of R atom at time t and time 0, respectively. Consequently, the results of MSD are given in Fig. 7.11 and the corresponding D are summarized in Table. 7.1 compared with other investigations. Our results have no big difference compared with other's investigations, and it indicates that the D of both water and ions are smaller while them being interacted with non-fully coated CSH than them in condition of diffusing freely in solution only. Furthermore, the D of water is decreased 12.26 % in 4 wt.% of NaCl solution than in pure water solution. Additionally, Fig. 7.11 shows that the MSD of water increasing more linear in time than ions (Cl^- and Na^+), further, the MSD of the ions is increasing gently slowly in time especially while solution being interacted with non-fully coated CSH.

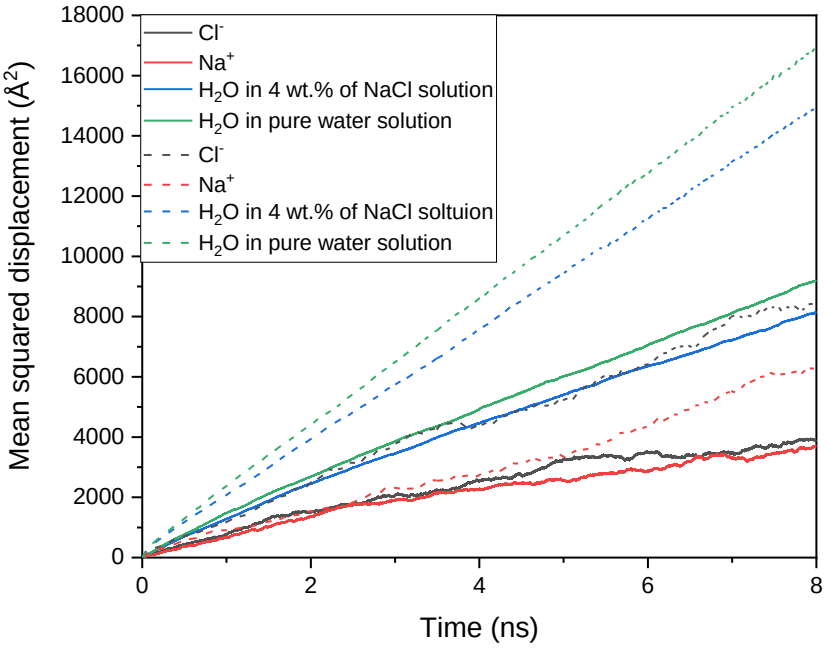

Fig. 7.11. The MSD of Cl^-, Na^+ and water molecules either in condition of diffusing freely in solution only (dash line) or being interacted with coated CSH (solid line).

Table 7.1

Self-diffusion coefficient of Cl^-, Na^+ and H_2O compared with others.

H_2O/ions	Diffusion coefficient 10^{-9} m^2/s		
	This work	Ab-initio [135]	Classical [135]
Cl^-	1.05 (1.95)	1.215	0.769
Na^+	0.98 (1.18)	0.799	0.723
H_2O in salty solution	1.88 (3.15)	1.412	2.139
H_2O in pure water solution	2.06 (3.59)	2.135	3.208

To have more understanding of this diffusion behavior of the ions, the RDF between the ions and CSH surface calcium atoms are investigated from well equilibrated structure of non-fully coated CSH model in salty water condition, and the correlation coordination values are evaluated as well. The cao is calcium atom on CSH surface, the results are presented in Fig. 7.12, which indicates a first bond length of 2.7 Å and 3.6 Å for cao-Cl and cao-Na, respectively. Those ionic bonds contribute to the diffusion behavior of the ions observed in Fig. 7.11, which means that the ions would diffuse slowly in time since they are bounded in the CSH surface. Further, the variation of the corresponding coordination number in radial distance indicates that chloridion could form a stable structure around calcium atom thus attack the CSH surface.

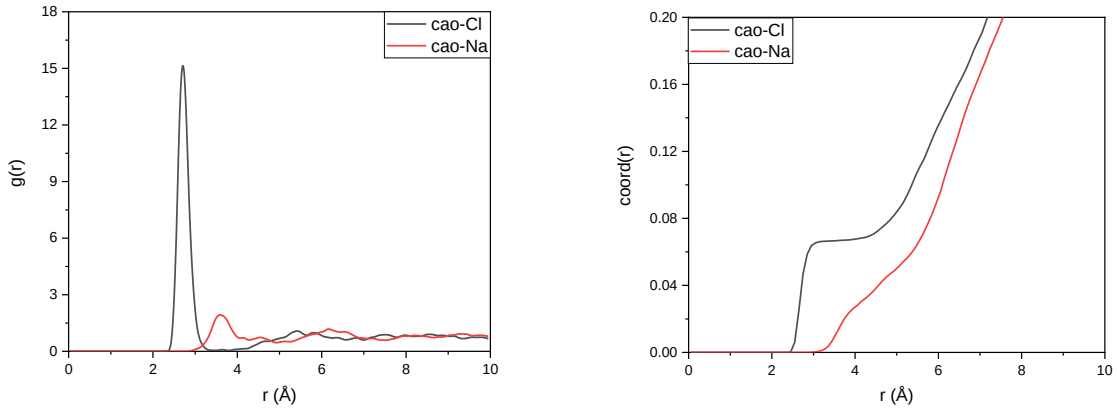

(a) (b)

Fig. 7.12. The partial radial distribution function of the ions (a), and its corresponding coordination number (b).

7.3.2 Impermeable behavior of fully coated CSH

It can be seen from Fig. 7.1 that the total energy of fully rubber coated CSH under salty water condition is well converged after 6 ns. The variation of the total energy of the rest 3 models of fully coated CSH under severe condition have the same behavior as the one presented in Fig. 7.1. The left view of the corresponding fully coated CSH model under aggressive condition at different times are given in Fig. 7.13, which indicates that fully rubber coating could make CSH impermeable under harsh environment. We noted that, the fully rubber coated CSH model under pure water solution condition are derived after itself being survived under salty water solution environment, since rubber coating surface roughness are decreased after it being interacted with salty water solution. Nevertheless, fully epoxy coated CSH shows an opposite behavior.

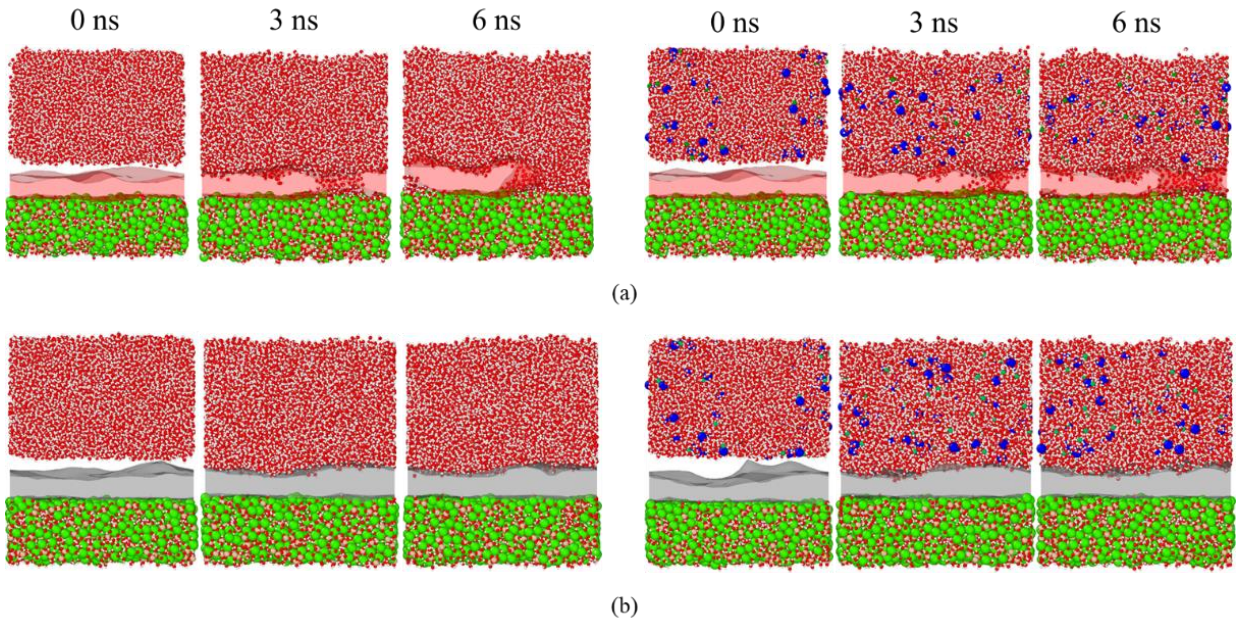

Fig. 7.13. The left view of fully epoxy coated CSH under pure water solution (left) and under salty water solution (right) at different times (a), the corresponding structure of fully rubber coated CSH (b). the epoxy coating and rubber coating are transparent to red and gray color, respectively.

To dig the behind inducement of the permeable behavior of epoxy coating under severe condition, the variation of epoxy coating surface under aggressive condition in time is studied. In Fig. 7.14, it is represented the top view of epoxy coated CSH model under aggressive condition in time using Van der Waals (VDW) radii of constituent atoms of each model [118, 126], we note that the aggressive solutions are hidden for a clear view of epoxy coating surface. Fig. 7.14 shows that the presence of pore structure in epoxy coating make it is permeable, and the pore size would be enlarged within time under aggressive condition. Moreover, the water sorption with time in case of fully epoxy coated CSH under pure water solution condition has been estimated, the results compared with experimental investigations are given in Fig. 7.15. It shows that the water sorption is increasing with time, and it has the same behavior compared with experimental studies [58].

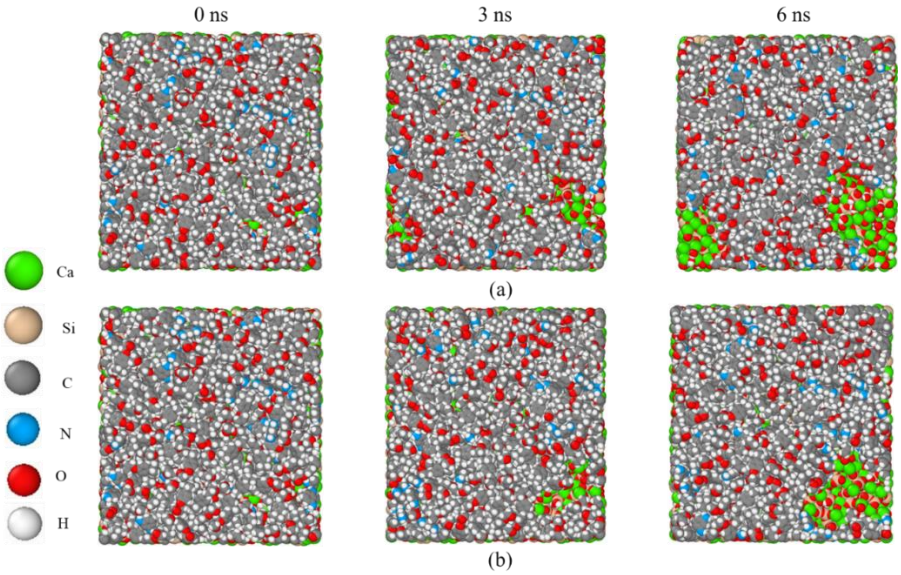

Fig. 7.14. The top view of epoxy coated CSH under pure water solution at different times (a), and under salty solution condition (b). The solutions are hidden.

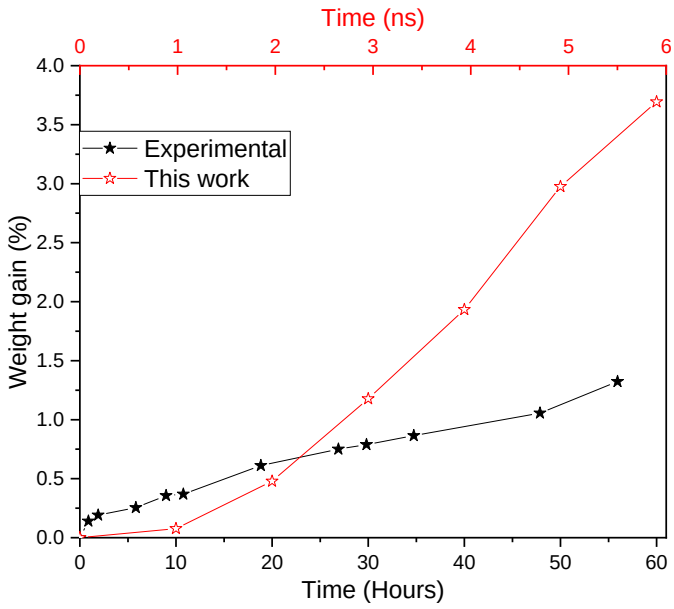

Fig. 7.15. Water sorption within time of fully epoxy coated CSH under pure water solution condition compared with experimental results [58].

Further, to probe the hidden parameters that make fully rubber coated CSH impermeable under salty water environment, its coating surface roughness has been evaluated by using triangulated surface mashes based on alpha-shape algorithm [136]. The initial state and well equilibrated state

of the rubber coating surface thickness of the corresponding structure (Fig. 7.13.b right) are presented in Fig. 7.16. The black lines are mash edges, and the results clearly indicates that the rubber coating surface roughness is decreased after being sandwiched between salty water solution and CSH.

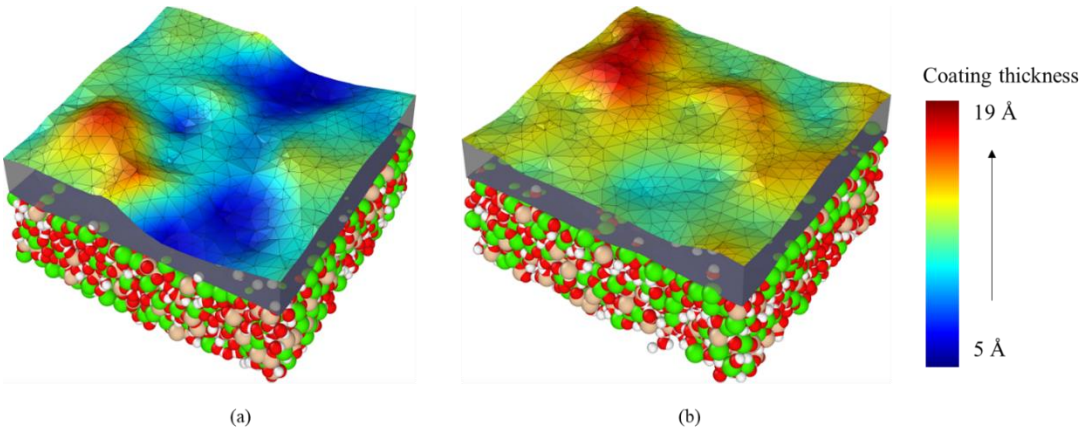

Fig. 7.16. The perspective view of rubber coated CSH under the salty solution condition: the initial state (a), the well relaxed state (b). The salty water solution is hidden.

Nevertheless, we have investigated how coating surface roughness affect the coating performance under pure water solution condition, which is simply done by put the structure presented in Fig. 7.16 under pure water solution environment. The outcomes of the one structure corresponding to Fig. 7.16.b is presented in Fig. 7.13.b (left), and the results of the other one structure is given in Fig. 7.17. Which indicates that the bigger surface roughness of rubber coating could make the fully rubber coated CSH model permeable under pure water solution. To have more understanding of this behavior, the variation of the surface roughness for the corresponding structures discussed above in the first 3 ns are investigated. In Fig. 7.18, it can be seen that the surface roughness is varies within time, and the initial big surface roughness contribute to the pore generation in coating surface as marked in Fig. 7.18.a.

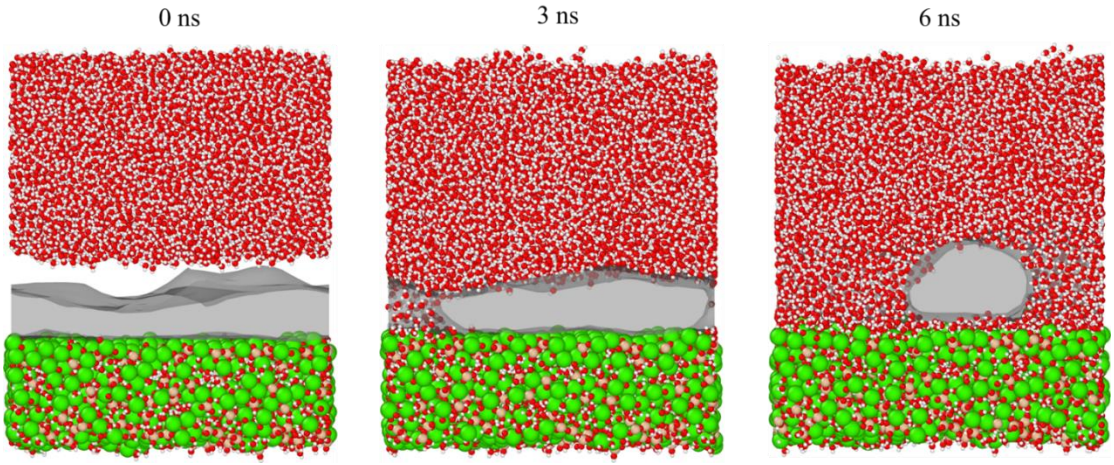

Fig. 7.17. The left view of the structure corresponding to Fig. 7.16.a under pure water solution condition at different times.

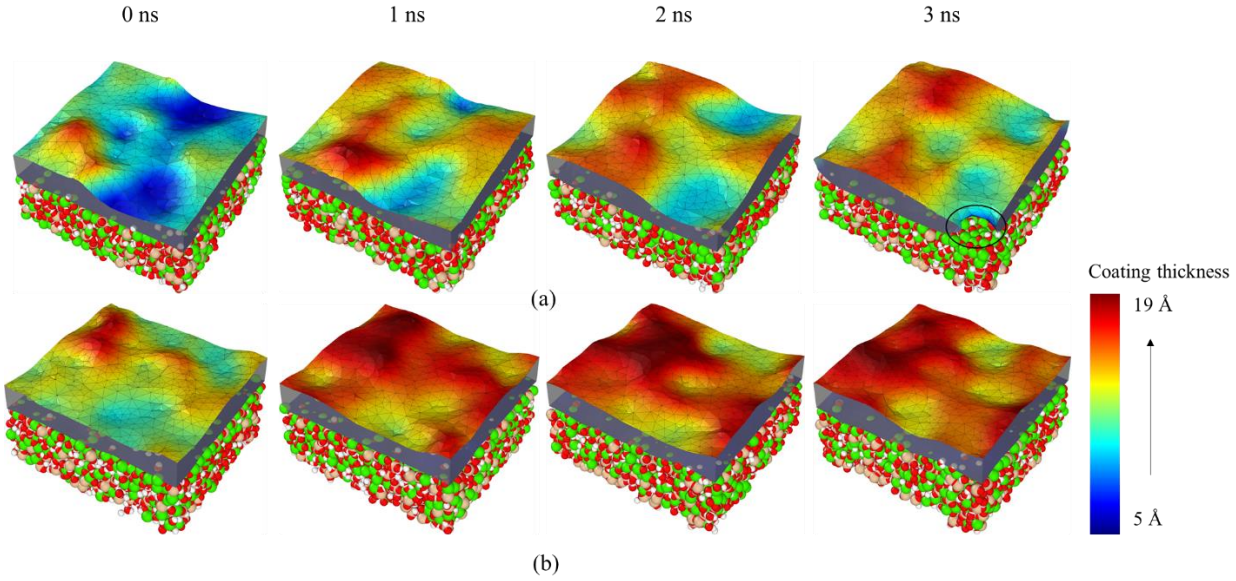

Fig. 7.18. The perspective view of the structure presented in Fig. 7.16 under the pure water solution at different times: corresponding to Fig. 7.16.a (a), corresponding to Fig. 7.16.b (b). The pure water solution is hidden.

Moreover, to have more understanding of the deterioration between fully coating and CSH under harsh environment, we investigated the fracture energy in two cases, one case is between permeable epoxy coating and CSH, and the other one is between impermeable rubber coating and CSH. The outcomes are presented in Fig. 7.19, it indicates that the interface fracture toughness between impermeable rubber coating and CSH would not decrease under harsh environment for 6 ns.

Nevertheless, for permeable epoxy coating, the interface fracture toughness could remain the same almost in 1 ns and 2 ns in condition of pure water solution and salty water solution, respectively. Then it begins a gently decreasing in another roughly 1 ns, the following decreasing is drastically. This behavior corresponding to the results we found in 7.3.1 section, which H_2O has a bigger D than the ions (Cl^- and Na^+), and its value is smaller in salty solution than in pure water solution.

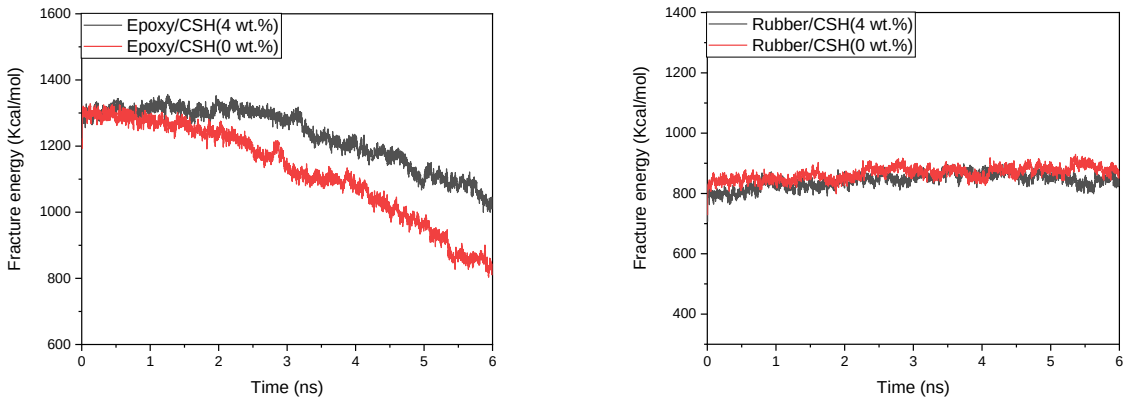

(a) (b)

Fig. 7.19. The variation of fracture energy between fully coating and CSH under different wt. % of NaCl solution condition within time: in case of epoxy/CSH (a), and in case of rubber/CSH (b)

Furthermore, the interaction energy between solution and CSH have been studied for two cases as well. In Fig. 7.20, it shows that the interaction energy between solution and CSH are decreasing quite slowly for impermeable rubber coating compared with the one permeable model.

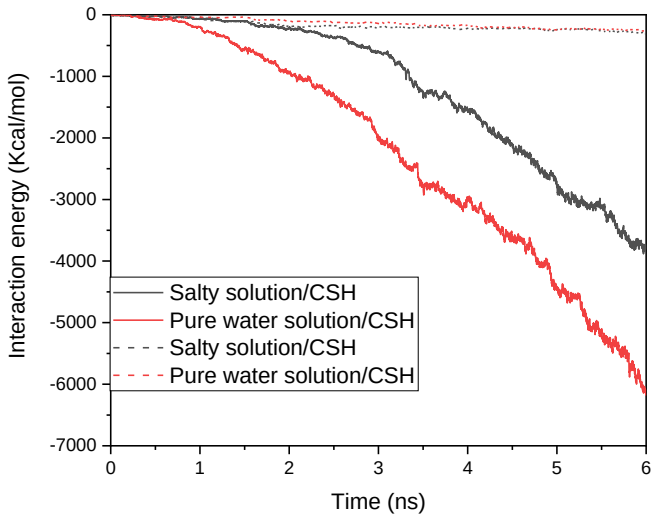

Fig. 7.20. The variation of the interaction energy between solution and CSH in time, in case of rubber coated CSH (dash line), epoxy coated CSH (solid line).

Further, the interfacial bond between rubber coating and CSH is investigated under harsh environment compared with under dry condition [19] as given in Fig. 7.21. The c3 and The c= are the Sp3 carbon atom in methyl group and the non-aromatic end doubly bonded carbon atom, respectively. Fig. 7.21 indicates that the trend of the RDF has no big difference among three conditions, nevertheless, the RDF of cao-c= ionic bond in pure water condition and dry condition are almost the same compared with in salty water condition.

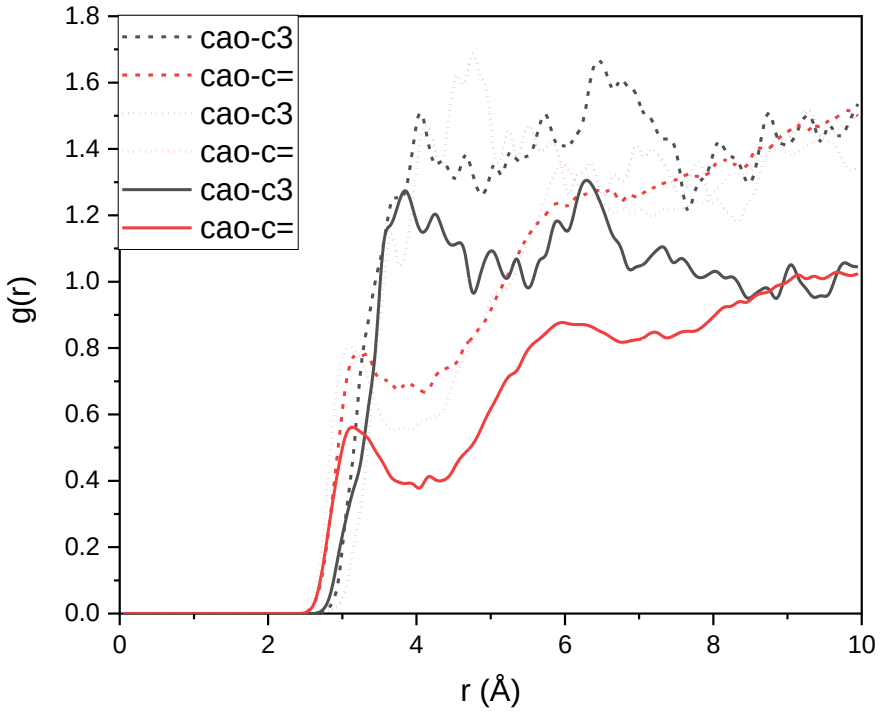

Fig. 7.21. The partial correlation function of fully rubber coated CSH under salty water solution condition (dash line), under pure water solution condition (dot line) compared with under dry condition [19] (solid line).

Further, we studied the chloridion diffusion coefficient in fully coated CSH models, the results as listed in Table 7.2. It shows that since the chloridion would be bounded in the CSH surface, thus caused a bigger diffusion coefficient in fully epoxy coated system than in the non-fully coated

system. Nevertheless, the order of magnitudes of diffusion coefficient is quite different compared with experimental results [58].

Table 7.2

The diffusion coefficient of chloridion for different systems compared with experimental results.

ions	Diffusion coefficient	
	Theoretical (this work)10^{-9} m^2/s	Experimental [58]10^{-12} m^2/s
Cl^-(in fully epoxy coated system)	1.33	2.59-7.67
Cl^-(in non-fully epoxy coated system)	1.05	
Cl^-(in fully rubber coated system)	1.26	8.4-9.56

7.4. Conclusions

In this work, the detachment process between epoxy coating and CSH under severe environment have been investigated, and what properties contribute to a fully impermeable organic-coating (epoxy and rubber) is studied as well. By means of Molecular dynamics simulations, a realistic CSH model, a confined layer of the organic-coating and a confined layer of solution (pure water solution and 4 wt.% of NaCl water solution) are utilized to represent the nano-scale level of the organic coated CSH model under aggressive environment. The combination of CLAYFF and CVFF force fields are utilized to describe the interatomic interactions. Results show that under harsh environment non-fully epoxy coating is detached more distorted in salty solution than in pure water solution. The chloridion is responsible to attack the epoxy resins coating and CSH surface. $Ca_{surface}$-O_{epoxy} and $Ca_{surface}$-N_{MPD} are the first two ionic bonds responsible to the adhesion between epoxy resins coating and CSH surface. The self-diffusion of H_2O is 12.26 % smaller in 4 wt. % of NaCl solution than in pure water solution. The pore structure in fully epoxy coating could weaken the interfacial adhesion between epoxy coating and CSH under severe condition. A big surface roughness of rubber coating contributes the pore generation under pure water solution condition. The water sorption for a permeable epoxy coating is increasing with time, in agreement with experimental findings. Further, a continuous well-distributed rubber coating is able to prohibit water and chloridion infiltration into cement paste.

Chapter 8:

General Conclusion and perspectives

8.1 General conclusions

This dissertation presents a theoretical investigation to engineer an impermeable hydrophobic Calcium-Silicate-Hydrate paste by a nano-coating treatment to enhance the durability of cementitious materials exposed to severe environment. By means of molecular dynamics simulations employing a realistic CSH model and ReaxFF potential, the work of adhesion and the wettability between a water-nanodroplet and CSH (001) surface were investigated. The obtained surface energy of (001) CSH surface is found in range of 698 erg/cm^2 to 740 erg/cm^2, in agreement with experimental findings, which contributes to the hydrophilic behavior of CSH (001) surface. Consequently, the averaged contact angle between equilibrated water-nanodroplet and CSH surface is found in range of 23.62° to 29.29°, which confirms the hydrophilic CSH surface. The calculated work of adhesion between water-nanodroplet and CSH surface is 136.47×10^{-3} J/m^2 in agreement with experimental data. For Connolly surface, solvent accessible area and VDW contact area, our calculations give the values of 8.991 J/m^2, 7.704 J/m^2 and 10.769 J/m^2, respectively. A deep atomistic level analysis was then investigated on the interfacial adhesion between epoxy resins layer and (001) CSH surface in order to understand the behind mechanism for the reduction of the hydrophilicity of the epoxy coated (001) CSH surface. The nanostructure of the full coated CSH is represented by gathering a confined layer cell of epoxy resins composed by DGEBA and MPD molecules and a realistic model of CSH. Results indicate that MPD would highly improve the coating efficiency. The obtained epoxy resins coated surface energy of CSH is in range of 33.7 mJ/m^2 to 45.5 mJ/m^2, which in agreement with the experimental data. The obtained value is roughly 93% to 95% lost compared with the surface without coating. Resulting in the averaged contact angle between the relaxed water-nanodroplet and the best coated CSH surface is found between 84.29° and 91.97°. This proves that epoxy coating extremely reduced the hydrophilicity of (001) CSH surface. The calculated work of adhesion between epoxy resins films and (001) CSH surface is 102.81 mJ/m^2 in agreement with the experimental findings. Moreover, 16.46 wt% of epoxy coating including 2.61% of MDP reduces by 3.14–3.57 times the hydrophilicity of CSH (001) surface.

Intrerestingly, results for rubber coating CSH surface show that the coating capability of TPI is better than CPI as well as CPB is better than TPB. The rubber coated CSH surface energy jumps up from the range of 698–740 mJ/m^2 to 40.8 mJ/m^2 to 48.4 mJ/m^2. The obtained contact angle is four times higher than the CSH surface, estimated between 92.85° and 98.11°, in agreement with

experimental data. This important result proves the hydrophobic behavior of rubber coated CSH nanostructure. Finally, the calculated work of adhesion between rubber coating and CSH surface is found in the range of 49.42 mJ/m^2 to 92.76 mJ/m^2.

Making CSH surface under an aggressive enviroment show that the interfacial degradation between coating and CSH highly reduces the durability of coated CSH. Results indicate that under harsh environment, non-fully epoxy coating is detached more distorted in salty solution than in pure water solution. The chlorine ions are contributed to attack the epoxy resins coating and CSH surface. $Ca_{surface}$-O_{epoxy} and $Ca_{surface}$-N_{MPD} are the first two ionic bonds responsible to the adhesion between epoxy resins coating and CSH surface. The self-diffusion of H_2O is 12.26 % smaller in 4 wt. % of NaCl solution than in pure water solution. The pore structure in fully epoxy coating would weaken the interfacial adhesion between epoxy coating and CSH under severe condition. A big surface roughness of rubber coating contributes to the pore generation under pure water solution condition. The water sorption for a permeable epoxy coating is increasing with time, in agreement with experimental findings. Further, a continuous well-distributed rubber nano-coating is able to prohibit water and chlorine infiltration into cement paste, leading to a promising future of durable cement paste material.

8.2 Perspectives

Based on the investigation findings in the thesis, form the point view of my experience, the further perspectives to continue the research could be point out as followings:

1. Reduce the pore size inside of epoxy coating surface that would enhance its impermeability. If the pore structures could be eliminated that would be even better.

2. Enhance the interface bonding interactions between surface coating (epoxy and rubber) and cement paste, which would be able to raise the interfacial adhesion to extend its durability.

3. Reduce the thickness of the surface rubber coating with remaining its impermeable properties.

4. Investigate the temperature influence onto the impermeable rubber coating.

5. Investigate the pressure effect onto the impermeable rubber coating.

6. Delve how surface coating (epoxy and rubber) behaves under the attack of sulfates, magnesium ions, and microorganism bacteria.

7. Study other appropriate coating agents instead of epoxy and rubber that could make cement paste superhydrophobic and further see their impermeability under various harsh environments.

List of the publications of this thesis

1. Wettability and work of adhesion of water nanodroplet on (001) surface of cement paste ---XD Zhu, A Zaoui, W Sekkal - Cement and Concrete Research 159, 106896 (2022).
2. Molecular-scale insight into improved waterproofing of cement paste by protective epoxy resins nano-coating ---XD Zhu, A Zaoui, W Sekkal - Powder Technology 426, 118679 (2023).
3. Theoretical process of rubber nano-coating on calcium silicate hydrate film for durable cementitious materials ---XD Zhu, A Zaoui, W Sekkal - Construction and Building Materials 397, 132441 (2023).

References

[1] K. Li, L. Xu, P. Stroeven, C. Shi, Water permeability of unsaturated cementitious materials: A review, Construction and Building Materials, 302 (2021).

[2] K.L. Scrivener, P. Juilland, P.J.M. Monteiro, Advances in understanding hydration of Portland cement, Cement and Concrete Research, 78 (2015) 38-56.

[3] X. Pan, Z. Shi, C. Shi, T.-C. Ling, N. Li, A review on concrete surface treatment Part I: Types and mechanisms, Construction and Building Materials, 132 (2017) 578-590.

[4] M. Schneider, M. Romer, M. Tschudin, H. Bolio, Sustainable cement production—present and future, Cement and Concrete Research, 41 (2011) 642-650.

[5] A. Arabzadeh, H. Ceylan, S. Kim, K. Gopalakrishnan, A. Sassani, S. Sundararajan, P.C. Taylor, Superhydrophobic coatings on Portland cement concrete surfaces, Construction and Building Materials, 141 (2017) 393-401.

[6] N.K. Ilango, P. Gujar, A.K. Nagesh, A. Alex, P. Ghosh, Interfacial adhesion mechanism between organic polymer coating and hydrating cement paste, Cement and Concrete Composites, 115 (2021).

[7] S.A.M. G, S. G, P.C. L, Performance characteristics of surface coatings applied to concrete for control of reinforcement corrosion, Construction and Building Materials, 14 (2000) 55-59.

[8] M.M.H. F, C.-B. P, A.D. M, Reducing water and chloride penetration through silicate treatments for concrete as a mean to control corrosion kinetics, Int. J. Electrochem. Sci, 7 (2012) 9682-9696.

[9] J.-G. Dai, Y. Akira, F.H. Wittmann, H. Yokota, P. Zhang, Water repellent surface impregnation for extension of service life of reinforced concrete structures in marine environments: The role of cracks, Cement and Concrete Composites, 32 (2010) 101-109.

[10] A. Szymańska, M. Dutkiewicz, H. Maciejewski, M. Palacz, Simple and effective hydrophobic impregnation of concrete with functionalized polybutadienes, Construction and Building Materials, 315 (2022).

[11] F. Wittmann, Surface tension skrinkage and strength of hardened cement paste, Matériaux et Constructions, 1 (1968) 547-552.

[12] E. Polzer, Diplomarbeit, angefertigt am Lehrstuhl für Baustoffkunde und Werkstoffprüfung der T. H. München, (1967).

[13] R. Di Mundo, C. Labianca, G. Carbone, M. Notarnicola, Recent Advances in Hydrophobic and Icephobic Surface Treatments of Concrete, Coatings, 10 (2020).
[14] C. L, C.J. H, Permeability and pore structure of OPC paste, Cement and Concrete Research, 31 (2001) 277-282.
[15] R. Feynman, There is plenty of room at the bottom, Engineering and Science, (1960).
[16] K.E. Drexler, C. Peterson, G. Pergamit, Unbounding the Future: The Nanotechnology Revolution, William Morrow and Company (1991).
[17] X. Zhu, A. Zaoui, W. Sekkal, Wettability and work of adhesion of water nanodroplet on (001) surface of cement paste, Cement and Concrete Research, 159 (2022).
[18] X.-D. Zhu, A. Zaoui, W. Sekkal, Molecular-scale insight into improved waterproofing of cement paste by protective epoxy resins nano-coating, Powder Technology, 426 (2023).
[19] X.-D. Zhu, A. Zaoui, W. Sekkal, Theoretical process of rubber nano-coating on calcium silicate hydrate film for durable cementitious materials, Construction and Building Materials, 397 (2023).
[20] H.M. Jennings, J.J. Thomas, J.S. Gevrenov, G. Constantinides, F.-J. Ulm, A multi-technique investigation of the nanoporosity of cement paste, Cement and Concrete Research, 37 (2007) 329-336.
[21] T.H.F. W., Proposed Structure for Calcium Silicate Hydrate Gel, Journal of the American Ceramic Society, 69 (1986) 464-467.
[22] E. Bonaccorsi, S. Merlino, H.F.W. Taylor, The crystal structure of jennite, Ca9Si6O18(OH)6·8H2O, Cement and Concrete Research, 34 (2004) 1481-1488.
[23] E. Bonaccorsi, S. Merlino, A.R. Kampf, The Crystal Structure of Tobermorite 14 A (Plombierite), a C-S-H Phase, Journal of the American Ceramic Society, 88 (2005) 505-512.
[24] R.J. Pellenq, A. Kushima, R. Shahsavari, K.J. Van Vliet, M.J. Buehler, S. Yip, F.J. Ulm, A realistic molecular model of cement hydrates, Proc Natl Acad Sci U S A, 106 (2009) 16102-16107.
[25] S.A. Hamid, The crystal structure of the 11Å natural tobermorite Ca2.25[Si3O7.5(OH)1.5] · 1H2O, Zeitschrift für Kristallographie-Crystalline Materials, 154 (1981) 189-198.
[26] A.J. Allen, J.J. Thomas, H.M. Jennings, Composition and density of nanoscale calcium-silicate-hydrate in cement, Nat Mater, 6 (2007) 311-316.

[27] M.J. Qomi, M. Bauchy, F.J. Ulm, R.J. Pellenq, Anomalous composition-dependent dynamics of nanoconfined water in the interlayer of disordered calcium-silicates, J Chem Phys, 140 (2014) 054515.
[28] H. Manzano, S. Moeini, F. Marinelli, A.C. van Duin, F.J. Ulm, R.J. Pellenq, Confined water dissociation in microporous defective silicates: mechanism, dipole distribution, and impact on substrate properties, J Am Chem Soc, 134 (2012) 2208-2215.
[29] M. Bauchy, M.J. Qomi, F.J. Ulm, R.J. Pellenq, Order and disorder in calcium-silicate-hydrate, J Chem Phys, 140 (2014) 214503.
[30] M. Laanaiya, A. Zaoui, Preventing cement-based materials failure by embedding Fe2O3 nanoparticles, Construction and Building Materials, 260 (2020).
[31] H. Manzano, R.J. Pellenq, F.J. Ulm, M.J. Buehler, A.C. van Duin, Hydration of calcium oxide surface predicted by reactive force field molecular dynamics, Langmuir, 28 (2012) 4187-4197.
[32] W. Sekkal, A. Zaoui, Novel properties of nano-engineered cementitious materials with fullerene buckyballs, Cement and Concrete Composites, 118 (2021).
[33] W. Sekkal, A. Zaoui, Enhancing the interfacial bond strength of cement nanocomposite with carbonate nanostructure, Composites Part B: Engineering, 124 (2017) 111-119.
[34] W. Sekkal, A. Zaoui, M. Benzerzour, N. Abriak, Role of porosity on the stiffness and stability of (001) surface of the nanogranular C–S–H gel, Cement and Concrete Research, 87 (2016) 45-52.
[35] Shafrin E G, Z.W. A., Constitutive relations in the wetting of low energy surfaces and the theory of the retraction method of preparing monolayers1, The Journal of Physical Chemistry, 64 (1960) 519-524.
[36] Brunauer S, Kantro D L, W.C. H., The surface energy of tobermorite, Canadian Journal of Chemistry, 37 (1959) 714-724.
[37] Brunauer S, Surface energy of a calcium silicate hydrate, Journal of Colloid and interface Science, 59 (1977) 433-437.
[38] R. Li, P. Hou, N. Xie, Z. Ye, X. Cheng, S.P. Shah, Design of SiO 2 /PMHS hybrid nanocomposite for surface treatment of cement-based materials, Cement and Concrete Composites, 87 (2018) 89-97.
[39] N.S. Klein, J. Bachmann, A. Aguado, B. Toralles-Carbonari, Evaluation of the wettability of mortar component granular materials through contact angle measurements, Cement and Concrete Research, 42 (2012) 1611-1620.

[40] E. Franzoni, B. Pigino, C. Pistolesi, Ethyl silicate for surface protection of concrete: Performance in comparison with other inorganic surface treatments, Cement and Concrete Composites, 44 (2013) 69-76.
[41] M. S, Y. J.F, D. D., ' Concrete', 2nd Edition Prentice Hall, Upper Saddle River, (2002) NJ, USA

[42] R.I. G., The nature of CSH in hardened cements, cement and concrete research, 29 (1999) 1131-1147.
[43] P.T. C, Structure and physical properties of hardened Portland cement paste, Journal of the american ceramic society, 41 (1958) 1-6.
[44] I.G. Richardson, The calcium silicate hydrates, Cement and Concrete Research, 38 (2008) 137-158.
[45] man RF, S.P. J., A new model for hydrated Portland cement and its practical implications, Engineering Journal, 53 (1970) 53-59.
[46] J. Li, Municipal Solid Waste Incineration Ash-Incorporated Concrete: One Step towards Environmental Justice, Buildings, 11 (2021).
[47] J.H. Taplin, A method for following the hydration reaction in portland cement paste, Australian Journal of Applied Science, 10 (1959) 329-345.
[48] Richardson I G, G.G. W., Microstructure and microanalysis of hardened cement pastes involving ground granulated blast-furnace slag, Journal of materials science, 27 (1992) 6204-6212.
[49] Rodger S A, G.G. W., Electron microscopy study of ordinary Portland cement and ordinary Portland cement–pulverized fuel ash blended pastes, Journal of the American Ceramic Society, 72 (1989) 1037-1039.
[50] Richardson I G, Groves G W, R.S. A., The Porosity and Pore Structure of Hydrated Cement Pastes as Revealed by Electron Micrsocopy Techniques, MRS Online Proceedings Library (OPL), 137 (1988) 313.
[51] Viehland D, Li J F, Yuan L J, Mesostructure of calcium silicate hydrate (C‐S‐H) gels in portland cement paste: short‐range ordering, nanocrystallinity, and local compositional order, Journal of the American Ceramic Society, 79 (1996) 1731-1744.
[52] Richardson I G, G.G. W., Microstructure and microanalysis of hardened ordinary Portland cement pastes, Journal of Materials science, 28 (1993) 265-277.

[53] Taylor H F W, N.D. E., An electron microprobe study of a mature cement paste, Cement and Concrete Research, 14 (1984) 565-573.
[54] Richardson I G, Brough A R, G.G. W, The characterization of hardened alkali-activated blast-furnace slag pastes and the nature of the calcium silicate hydrate (CSH) phase, Cement and Concrete Research, 24 (1994) 813-829.
[55] M. L. Berndt, Evaluation of coatings, mortars and mix design for protection of concrete against sulphur oxidising bacteria, Construction and Building Materials, 25 (2011) 3893-3902.
[56] M. Khanzadeh Moradllo, M. Shekarchi, M. Hoseini, Time-dependent performance of concrete surface coatings in tidal zone of marine environment, Construction and Building Materials, 30 (2012) 198-205.
[57] A.R. Suleiman, A.M. Soliman, M.L. Nehdi, Effect of surface treatment on durability of concrete exposed to physical sulfate attack, Construction and Building Materials, 73 (2014) 674-681.
[58] A. A. Almusallam, F. M. Khan, S. U. Dulaijan, O. S. B.Al-Amoudi, Effectiveness of surface coatings in improving concrete durability, Cement and Concrete Composites, 25 (2003) 473-481.
[59] C. Vipulanandan, J. Liu, Performance of polyurethane-coated concrete in sewer environment, Cement and Concrete Research, 35 (2005) 1754-1763.
[60] K. Benzarti, C. Perruchot, M.M. Chehimi, Surface energetics of cementitious materials and their wettability by an epoxy adhesive, Colloids and Surfaces A: Physicochemical and Engineering Aspects, 286 (2006) 78-91.
[61] W. Zheng, W.G. Chen, T. Feng, W.Q. Li, X.T. Liu, L.L. Dong, Y.Q. Fu, Enhancing chloride ion penetration resistance into concrete by using graphene oxide reinforced waterborne epoxy coating, Progress in Organic Coatings, 138 (2020).
[62] M. Horgnies, J.J. Chen, Superhydrophobic concrete surfaces with integrated microtexture, Cement and Concrete Composites, 52 (2014) 81-90.
[63] M.V. Diamanti, A. Brenna, F. Bolzoni, M. Berra, T. Pastore, M. Ormellese, Effect of polymer modified cementitious coatings on water and chloride permeability in concrete, Construction and Building Materials, 49 (2013) 720-728.
[64] G. Li, A. Akbar, L.-W. Zhang, F. Rosei, K.M. Liew, Surface modification strategy for controlling wettability and ionic diffusion behaviors of calcium silicate hydrate, Applied Surface Science, 622 (2023).

[65] M. Li, H. Zheng, Y. Duan, D. Hou, P. Wang, B. Pang, S. Li, Z. Jin, The Wetting Behavior of Water Droplets on Silane and Silane/GO-Modified Ettringite Surfaces: Insights into Molecular Dynamics Simulations, Coatings, 13 (2023).
[66] S. Cheng, Z. Shui, X. Gao, R. Yu, T. Sun, C. Guo, Y. Huang, Degradation mechanisms of Portland cement mortar under seawater attack and drying-wetting cycles, Construction and Building Materials, 230 (2020).
[67] C. Tuakta, O. Büyüköztürk, Deterioration of FRP/concrete bond system under variable moisture conditions quantified by fracture mechanics, Composites Part B: Engineering, 42 (2011) 145-154.
[68] A. Zhou, O. Büyüköztürk, D. Lau, Debonding of concrete-epoxy interface under the coupled effect of moisture and sustained load, Cement and Concrete Composites, 80 (2017) 287-297.
[69] N. Kumano, K. Mori, M. Kato, M. Ishii, Degradation of scratch resistance of clear coatings by outdoor weathering, Progress in Organic Coatings, 135 (2019) 574-581.
[70] H.A. Al-Turaif, Surface morphology and chemistry of epoxy-based coatings after exposure to ultraviolet radiation, Progress in Organic Coatings, 76 (2013) 677-681.
[71] H. Wang, P. Feng, Y. Lv, Z. Geng, Q. Liu, X. Liu, A comparative study on UV degradation of organic coatings for concrete: Structure, adhesion, and protection performance, Progress in Organic Coatings, 149 (2020).
[72] Allen M P, T.D. J, Computer simulation of liquids, Oxford university press, (1989).
[73] Tuckerman M E, M.G. J., Understanding modern molecular dynamics: Techniques and applications, The Journal of Physical Chemistry B, 104 (2000) 159-178.
[74] O. Büyüköztürk, M.J. Buehler, D. Lau, C. Tuakta, Structural solution using molecular dynamics: Fundamentals and a case study of epoxy-silica interface, International Journal of Solids and Structures, 48 (2011) 2131-2140.
[75] Hansson T, Oostenbrink C, v.G.W. F., Molecular dynamics simulations, Current opinion in structural biology, 12 (2002) 190-196.
[76] T.A. Hunt, B.D. Todd, On the Arnold cat map and periodic boundary conditions for planar elongational flow, Molecular Physics, 101 (2003) 3445-3454.
[77] W.F. van Gunsteren, H.J.C. Berendsen, Algorithms for macromolecular dynamics and constraint dynamics, Molecular Physics, 34 (1977) 1311-1327.

[78] H. Grubmüller, H. Heller, A. Windemuth, K. Schulten, Generalized Verlet algorithm for efficient molecular dynamics simulations with long-range interactions, Molecular Simulation, 6 (1991) 121-142.
[79] O.S. Olafusi, E.R. Sadiku, J. Snyman, J.M. Ndambuki, W.K. Kupolati, Application of nanotechnology in concrete and supplementary cementitious materials: a review for sustainable construction, SN Applied Sciences, 1 (2019).
[80] M.A. González, Force fields and molecular dynamics simulations, École thématique de la Société Française de la Neutronique, 12 (2011) 169-200.
[81] A.D. Mackerell, Jr., Empirical force fields for biological macromolecules: overview and issues, J Comput Chem, 25 (2004) 1584-1604.
[82] G. A., Molecular aggregation: structure analysis and molecular simulation of crystals and liquids, Oxford University Press, (2007).
[83] Mayo S L, Olafson B D, Goddard W A, DREIDING: a generic force field for molecular simulations, Journal of Physical chemistry, 94 (1990) 8897-8909.
[84] Rappé A K, Casewit C J, Colwell K S, UFF, a full periodic table force field for molecular mechanics and molecular dynamics simulations, Journal of the American chemical society, 114 (1992) 10024-10035.
[85] A.D. MacKerell, D. Bashford, M. Bellott, R.L. Dunbrack, J.D. Evanseck, M.J. Field, S. Fischer, J. Gao, H. Guo, S. Ha, D. Joseph-McCarthy, L. Kuchnir, K. Kuczera, F.T. Lau, C. Mattos, S. Michnick, T. Ngo, D.T. Nguyen, B. Prodhom, W.E. Reiher, B. Roux, M. Schlenkrich, J.C. Smith, R. Stote, J. Straub, M. Watanabe, J. Wiorkiewicz-Kuczera, D. Yin, M. Karplus, All-atom empirical potential for molecular modeling and dynamics studies of proteins, J Phys Chem B, 102 (1998) 3586-3616.
[86] Cornell W D, Cieplak P, Bayly C I, A second generation force field for the simulation of proteins, nucleic acids, and organic molecules, Journal of the American Chemical Society, 117 (1995) 5179-5197.
[87] C. Oostenbrink, A. Villa, A.E. Mark, W.F. van Gunsteren, A biomolecular force field based on the free enthalpy of hydration and solvation: the GROMOS force-field parameter sets 53A5 and 53A6, J Comput Chem, 25 (2004) 1656-1676.

[88] D.O. P, R.V. A, O.D. J, Structure and energetics of ligand binding to proteins: Escherichia coli dihydrofolate reductase-trimethoprim, a drug-receptor system, Proteins: Structure, Function, and Bioinformatics, 4 (1988) 31-47.
[89] C.R. T, L.J. J, K.A. G, Molecular models of hydroxide, oxyhydroxide, and clay phases and the development of a general force field, The Journal of Physical Chemistry B, 108 (2004) 1255-1266.
[90] Brenner D W, Shenderova O A, Harrison J A, A second-generation reactive empirical bond order (REBO) potential energy expression for hydrocarbons, Journal of Physics: Condensed Matter, 14 (2002) 783.
[91] Stuart S J, Tutein A B, H.J. A., A reactive potential for hydrocarbons with intermolecular interactions, The Journal of chemical physics, 112 (2000) 6472-6486.
[92] L. Liu, Y. Liu, S.V. Zybin, H. Sun, W.A. Goddard, 3rd, ReaxFF-lg: correction of the ReaxFF reactive force field for London dispersion, with applications to the equations of state for energetic materials, J Phys Chem A, 115 (2011) 11016-11022.
[93] Martínez L, Andrade R, Birgin E G, Packmol: A package for building initial configuration for molecular dynamics simulations, Journal of computational chemistry, 30 (2009) 2157-2164.
[94] P. Hirel, Atomsk: A tool for manipulating and converting atomic data files, Computer Physics Communications, 197 (2015) 212-219.
[95] W.L. Jorgensen, J. Chandrasekhar, J.D. Madura, R.W. Impey, M.L. Klein, Comparison of simple potential functions for simulating liquid water, The Journal of Chemical Physics, 79 (1983) 926-935.
[96] X.B. Zhang, Q.L. Liu, A.M. Zhu, An improved fully flexible fixed-point charges model for water from ambient to supercritical condition, Fluid Phase Equilibria, 262 (2007) 210-216.
[97] Van Duin A C T, Dasgupta S, Lorant F, ReaxFF: A Reactive Force Field for Hydrocarbons, The Journal of Physical Chemistry A, 105 (2001) 9396-9409.
[98] Chenoweth K, Van Duin A C T, G.W. A., ReaxFF Reactive Force Field for Molecular Dynamics Simulations of Hydrocarbon Oxidation, The Journal of Physical Chemistry A, 112 (2008) 1040-1053.
[99] A.K. Rappe, W.A. Goddard, Charge equilibration for molecular dynamics simulations, The Journal of Physical Chemistry, 95 (2002) 3358-3363.

[100] N. A., Parallel multilevel preconditioned conjugate-gradient approach to variable-charge molecular dynamics, Computer Physics Communications, 104 (1997) 59-69.
[101] Aktulga H M, Fogarty J C, Pandit S A, Parallel reactive molecular dynamics: Numerical methods and algorithmic techniques, Parallel Computing, 38 (2012) 245-259.
[102] B. Guillot, Y. Guissani, How to build a better pair potential for water, The Journal of Chemical Physics, 114 (2001) 6720-6733.
[103] P. S., Fast Parallel Algorithms for Short-Range Molecular Dynamics, Journal of computational physics, 117 (1995) 1-19.
[104] S. Misra, P.D. Fleming, W.L. Mattice, Structure and energy of thin films of poly-(1, 4-cis-butadiene): A new atomistic approach, Journal of Computer-Aided Materials Design, 2 (1995) 101-112.
[105] T.C. Clancy, W.L. Mattice, Computer simulation of polyolefin interfaces, Computational and Theoretical Polymer Science, 9 (1999) 261-270.
[106] D. He, D.H. Reneker, W.L. Mattice, Fully atomistic models of the surface of amorphous polyethylene, Computational and Theoretical Polymer Science, 7 (1997) 19-24.
[107] G.J. Martyna, M.L. Klein, M. Tuckerman, Nosé–Hoover chains: The canonical ensemble via continuous dynamics, The Journal of Chemical Physics, 97 (1992) 2635-2643.
[108] M. Laanaiya, A. Zaoui, Piezoelectric response and failure behavior of cement paste under external loading, Cement and Concrete Research, 139 (2021).
[109] S. Soyer-Uzun, S.R. Chae, C.J. Benmore, H.-R. Wenk, P.J.M. Monteiro, P. Brown, Compositional Evolution of Calcium Silicate Hydrate (C-S-H) Structures by Total X-Ray Scattering, Journal of the American Ceramic Society, 95 (2012) 793-798.
[110] A. Zaoui, Insight into elastic behavior of calcium silicate hydrated oxide (C–S–H) under pressure and composition effect, Cement and Concrete Research, 42 (2012) 306-312.
[111] G. Constantinides, F.-J. Ulm, The nanogranular nature of C–S–H, Journal of the Mechanics and Physics of Solids, 55 (2007) 64-90.
[112] Y. Zheng, A. Zaoui, Wetting and nanodroplet contact angle of the clay 2:1 surface: The case of Na-montmorillonite (001), Applied Surface Science, 396 (2017) 717-722.
[113] A. Zaoui, W. Sekkal, Atomic-scale study of the nonmelting, wetting, and freezing behavior of KCl(100), Physical Review B, 70 (2004).

[114] W. Sekkal, M. Izadifar, A. Zaoui, N. Ukrainczyk, E. Koenders, Theoretical investigation of protective graphene-coated metakaolin geopolymer interface under moisture and chemical composition effects, Powder Technology 430 (2023) 119007.
[115] M.E. Schrader, Young-Dupre revisited, Langmuir, 11 (1995) 3585-3589.
[116] Vargaftik N B, Volkov B N, V.L. D, International tables of the surface tension of water, Journal of Physical and Chemical Reference Data, 12 (1983) 817-820.
[117] L. Courard, Evaluation of thermodynamic properties of concrete substrates and cement slurries modified with admixtures, Materials and structures, 35 (2002) 149-155.
[118] S.S. Batsanov, Van der Waals radii of elements, Inorganic materials, 37 (2001) 871-885.
[119] H.J.C. Berendsen, J.P.M. Postma, W.F.v. Gunsteren, Interaction models for water in relation to protein hydration, Intermolecular forces, (1981) 331-342.
[120] L. Verlet, Computer" experiments" on classical fluids. I. Thermodynamical properties of Lennard-Jones molecules, Physical review, 159 (1967) 98.
[121] R.W. Hockney, J.W. Eastwood, Computer Simulation Using Particles, Taylor & Francis Group, New York, 1988, pp. 267-301.
[122] E.L. Pollock, J. Glosli, Comments on P3M, FMM, and the Ewald method for large periodic Coulombic systems, Computer Physics Communications, 95 (1996) 93-110.
[123] W. Sekkal, A. Zaoui, High strength metakaolin-based geopolymer reinforced by pristine and covalent functionalized carbon nanotubes, Construction and Building Materials, 327 (2022).
[124] L.L. Zhang, A. Zaoui, W. Sekkal, Y.Y. Zheng, Interlayer adsorption of cationic dye on cationic surfactant-modified and unmodified montmorillonite, J Hazard Mater, 442 (2023) 130107.
[125] Y. Zheng, A. Zaoui, Temperature effects on the diffusion of water and monovalent counterions in the hydrated montmorillonite, Physica A: Statistical Mechanics and its Applications, 392 (2013) 5994-6001.
[126] R.S. Rowland, R. Taylor, Intermolecular nonbonded contact distances in organic crystal structures: Comparison with distances expected from van der Waals radii, The Journal of Physical Chemistry, 100 (1996) 7384-7391.
[127] A. Einstein, On the motion of small particles suspended in liquids at rest required by the molecular-kinetic theory of heat, Ann. Phys., 17 (1905) 549-560.

[128] D. Hou, Q. Yang, P. Wang, Z. Jin, M. Wang, Y. Zhang, X. Wang, Unraveling disadhesion mechanism of epoxy/CSH interface under aggressive conditions, Cement and Concrete Research, 146 (2021).
[129] E. Hosseini, M. Zakertabrizi, A. Habibnejad Korayem, Z. Zaker, R. Shahsavari, Orbital Overlapping through Induction Bonding Overcomes the Intrinsic Delamination of 3D-Printed Cementitious Binders, ACS Nano, 14 (2020) 9466-9477.
[130] C.H. Y, Determination of cis-1, 4 and trans-1, 4 Contents of Polyisoprenes by High Resolution Nuclear Magnetic Resonance, Analytical Chemistry, 34 (1962) 1793-1795.
[131] P. Sharma, S. Roy, H.A. Karimi-Varzaneh, Validation of Force Fields of Rubber through Glass-Transition Temperature Calculation by Microsecond Atomic-Scale Molecular Dynamics Simulation, J Phys Chem B, 120 (2016) 1367-1379.
[132] Faller R, Müller-Plathe F, Doxastakis M, Local structure and dynamics of trans-polyisoprene oligomers, Macromolecules, 34 (2001) 1436-1448.
[133] Fetters L J, Lohse D J, R. D, Connection between polymer molecular weight, density, chain dimensions, and melt viscoelastic properties, Macromolecules, 27 (1994) 4639-4647.
[134] Fetters L J, Lohse D J, G.W. W, Chain dimensions and entanglement spacings in dense macromolecular systems, Journal of Polymer Science Part B: Polymer Physics, 37 (1999) 1023-1033.
[135] Y. Ding, A.A. Hassanali, M. Parrinello, Anomalous water diffusion in salt solutions, Proc Natl Acad Sci U S A, 111 (2014) 3310-3315.
[136] A. Stukowski, Computational Analysis Methods in Atomistic Modeling of Crystals, Jom, 66 (2013) 399-407.